SPATIOTEMPORAL PATTERNS IN WATER YIELD FROM THE HUMID PUNA: A CASE STUDY IN THE AGRARIAN DISTRICT OF ZURITE, PERÚ

By

Wyeth Wunderlich

A Thesis Presented to

The Faculty of Humboldt State University

In Partial Fulfillment of the Requirements for the Degree

Master of Science in Environmental Systems: Geology

Committee Membership

Dr. Jasper Oshun, Committee Chair

Dr. Margaret Lang, Committee Member, Graduate Coordinator

Dr. Kristina Keating, Committee Member

Dr. Laura Levy, Committee Member

May 2021

ABSTRACT

SPATIOTEMPORAL PATTERNS IN WATER YIELD FROM THE HUMID PUNA: A CASE STUDY IN THE AGRARIAN DISTRICT OF ZURITE, PERÚ

Wyeth Wunderlich

The humid puna is a seasonally dry alpine grass- and shrub-land biome that exists at the altitudinal limits of plant survival, hosts peat-forming wetlands known as *bofedales*, and yields water to streams used by small and large communities throughout the central and southern Peruvian Andes. Despite the importance of the humid puna in supplying water resources, particularly to perennial streams, few studies have quantified water yield and no studies have explored relationships between the structure of puna landscapes and spatial patterns in water yield. Zurite (population: 3,640, elevation: 3,011 m.a.s.l., annual precipitation: 855 mm) is an agrarian district in the department of Cusco, Perú that derives water resources from the Upper Ramuschaka Watershed (URW, area: 2.12 km^2, mean elevation: 4,332 m.a.s.l.), a humid puna headwater catchment with 11.5% coverage of seasonally saturated *bofedales*. The URW provides an opportunity to explore the hydrology of the Andean puna, and to present baseline water resources data to the community of Zurite to guide sustainable water management and resiliency to a changing climate. Our study sought to: a) Determine the total, wet, and dry season water yield and derive annual water balances from *in-situ* measurements in the URW; b) Explore the temporal phases of the URW annual water balance; c) Identify relationships between

spatiotemporal patterns in water yield and the presence of *bofedales*; and d) Estimate seasonal dynamic water storage contributions to dry season runoff from *bofedales* in the URW. We monitored precipitation inputs, seasonal dynamics in subsurface moisture, groundwater, and streamflow for two years, and took distributed discharge measurements at 18 subbasins nested throughout the Central and Eastern tributaries of the URW from June 2019 - January 2021. Over the course of four field campaigns spanning wet and dry seasons, we flew an unmanned aerial vehicle (UAV) to generate a 1-m resolution digital elevation model (DEM) for topographic analyses, and measured material and hydrologic properties in *bofedales* via direct measurements and downhole nuclear magnetic resonance (NMR).

The URW received 749 mm annual precipitation in WY2019 and 825 mm in WY2020. Annual runoff ranged from 62% to 80% of the annual water balance, with dry season runoff accounting for between 11% and 19% of annual runoff. Spatiotemporal analysis of water yield throughout the URW revealed that subbasins with a greater proportion of *bofedal* land cover yielded greater unit runoff and that this relationship strengthened through the dry season. We estimated seasonal dynamic water storage across all *bofedales* of the URW to account for 50 - 60 mm of streamflow contributions, or approximately one half of dry season runoff. Collectively, these results suggest: a) water yield from headwater humid puna catchments can represent 60-80% of annual precipitation, and b) *bofedales* integrate groundwater resources from upslope contributing areas 4 – 12 times their area, store water primarily in high porosity peat, and release water through low conductivity clay rich deposits, sustaining baseflow. Regional research

and management efforts should design monitoring programs to improve baseline *bofedal* hydrology data sets and specifically incorporate *bofedales* in conservation initiatives due to their role in sustaining dry season streamflow in the puna.

ACKNOWLEDGEMENTS

This thesis is a product of the participation, hard work, and dedicated contributions from many collaborators. Thank you to my advisor, Dr. Jasper Oshun, for the opportunity and orchestration of the *Bonanza en los Andes* project. Thank you to my committee members and collaborators, Dr. Margaret Lang and Dr. Kristina Keating, for your expertise, leadership, and resilience in conducting remote research in the Peruvian Andes and thank you to Dr. Laura Levy for the valuable thesis input and feedback.

I would like to acknowledge the generous financial support from the funding partners of the *Bonanza en los Andes* research project, Geoscientists Without Borders (GWB). Thank you to the Lost Coast Rotaract for the generous funding in support of my participation in *Bonanza en los Andes*. I extend my heartfelt appreciation to the Bud Burke Geology Scholarship for providing fiscal support at a particularly challenging moment in life, and to the HSU Geology department and the personnel behind the scenes that have supported me personally and in this research effort throughout my time at HSU.

I extend my deepest gratitude to the community of Zurite for hosting and collaborating with the *Bonanza en los Andes* project and team, with a special thanks to our host family and key community collaborators – Tomás Ruiz López and Gladis Quispe. A special thanks for the contributions made by collaborators in Cusco, Perú, particularly the intensive and challenging field work, leadership, and friendship of Mr. Wilner Bandera Perez - the dedication and efforts of whom were crucial to the completion and success of this thesis. Thank you to Ingeniero Rene Pumayalli and Unu

Kumachiq Cusco Groundwater Consultants for offering support, consultation, and collaboration regarding regional groundwater hydrology and technical logistics. Thank you to the guardians in Zurite who noted field conditions, assisted in field work, and protected field instruments throughout the monitoring process, and to the community members in Zurite who joined in field efforts to support and learn about our hydrogeologic investigations in their home district. I would like to acknowledge the essential community support and collaboration from the local governing entities in Zurite: *el Comisión de Regantes de Agua*, *Municipalidad Distrital de Zurite*, and *la Comunidad*.

I am thankful to Nolan Marshall for, among much other field work, conducting *bofedal* borehole surveys over two Zurite field seasons. Thank you to Laurel Smith for also conducting two Zurite field seasons and designing and executing technically and logistically challenging photogrammetric drone surveys in the complex topography of the Upper Ramuschaka Watershed. I am very appreciative for the significant contributions and field efforts made by HSU students Samuel Bold, Alyssa Virgil, Olivia Helprin, Edward Davis, Jared Walbert, Jillian Freiheit, Malia Gonzalez, Peter Duin, Nick Hawthorne, Emily Santos, Hannah Gidanian, Yojana Miraya, Jazmin Sandoval, and Nathalie Ruiz. And lastly, thank you very much to student collaborators from other institutions: Logan Schmidt, Hunter Murray, Vidal Barrientos, Oscar Huaman and the many unnamed collaborators in the community of Zurite and beyond that made this project possible.

TABLE OF CONTENTS

LIST OF TABLES

LIST OF FIGURES

LIST OF APPENDICES

INTRODUCTION

Regional Precipitation and Runoff Patterns in the Tropical Andes

The Andes Mountains extend from Colombia (~10^{o}N) to the southern tip of South America (~52^{o} S), representing the only major continuous boundary to upper-level atmospheric circulation in the Southern Hemisphere (Lenters and Cook, 1995; Garreaud, 2009). The Andes are a product of tectonic subduction of the Nazca beneath the South America plate that drives uplift, accretion, crustal shortening, magmatic addition, and complex local-scale geologic processes (Gregory-Wodzicki, 2000). Mean peak mountain heights of the tropical and subtropical Andes exceed 4000 m.a.s.l. (Garreaud, 2009; Garreaud et al., 2009), creating a barrier to large transpiration fluxes from the Amazon Basin and Atlantic Ocean that dictates precipitation patterns across the continent of South America (Lenters and Cook, 1995; Gregory-Wodzicki, 2000, Garreaud, 2009; Garreaud et al., 2009). Elevational and climatic gradients throughout the Andes drive the distribution of distinct alpine, subalpine, shrubland, and montane forest ecosystem belts that correspond strongly with regional precipitation patterns (Squeo et al., 2006; Josse et al., 2009).

Regional climate in the southern hemisphere Tropical Andes (extending from 5^{o}S to 23^{o}S) is driven by upper-level large-scale seasonal circulation patterns (Garreaud et al., 2009; Garreaud, 2009). The austral summer (December, January, and February) climate is characterized by light easterly winds from the Atlantic Ocean and Amazon Basin down

to 21°S, resulting in advective transport of humid air mass from the Amazon Basin to the low- and mid-latitude regions of the Andes that brings orographic precipitation and a warm, wet austral summer (Lenters and Cook, 1997; Garreaud, 2009). In contrast, the austral winter (June, July, and August) brings weakening easterlies that are held north of 10°S latitude; meanwhile, the subtropical westerly jet stream strengthens, centered at 30°S, and carries cool, dry air mass from the Pacific coast that results in a regionally cool and dry austral winter (e.g., Garreaud, 2009). The seasonality of precipitation in the Andes has led to communities depending on water from upland catchments derived from either glaciers or, more commonly, from perennial streams - especially during the dry austral winter south of 10°S latitude (Bradley et al., 2006; Buytaert et al., 2006; Celleri et al., 2010; Drenkhan et al., 2015).

More than 99% of tropical glaciers globally are found in the Andes, totaling approximately 1800 km^2 glacierized land area across Bolivia, Perú, Ecuador, Colombia, and Venezuela (Kaser, 1999; Rabatel et al., 2013; Drenkhan et al., 2018). Even in the most glacierized tropical catchment in the world: the Santa River (11,600 km^2), which drains westward into the Pacific Ocean in Central Perú, glaciers comprise only 3.60% of the total catchment area (Drenkhan et al, 2015). Despite glacier meltwater contributions from the Cordillera Blanca, the most extensively glacierized region of the Santa River Watershed (Barnett et al., 2005; Bradley et al, 2006; Baraer et al., 2009; Kaser et al, 2010; Drenkhan et al., 2015; Buytaert et al., 2017; Vuille et al., 2018; Drenkhan et al. 2018), recent studies showed that the majority of dry season discharge was sourced from precipitation-recharged groundwater in catchments with drainage areas ranging from 8.25

km^2 – 170 km^2 (Baraer et al., 2009; Gordon et al., 2015; Somers et al., 2019). Such substantial dry season contributions are often linked to proglacial geomorphic features that provide groundwater storage - such as large cross valley moraines, talus slopes, and glaciofluvial deposits in valley bottoms (Baraer et al., 2009; Gordon et al., 2015; Somers et al., 2016; Glas et al., 2019). Integrated groundwater-surface water modeling of the proglacial Shullcas catchment (drainage area: 170 km^2) in the Cordillera Blanca estimated that approximately 90% of discharge was derived from precipitation-recharged sources, with 72% of dry season discharge from groundwater aquifers that received nominal recharge (~2%) from glacier meltwater (Somers et al., 2019). The results from groundwater studies in glacierized catchments of the Cordillera Blanca indicate that groundwater is primarily recharged by precipitation and operates mostly independently from glacier meltwater runoff processes, despite links to proglacial geomorphic features (Baraer et al., 2009; Gordon et al., 2015; Glas et al., 2019; Somers et al., 2019).

Water Resources in the Vilcanota Watershed

The Vilcanota Watershed (drainage area: 11,048 km^2, also known as the Vilcanota-Urubamba Basin) (Figure 1) is a drainage with over 4,800 m of vertical relief that flows northward from peaks that exceed 6,000 m.a.s.l. into the Amazon River. Here, we adopt the watershed boundary described by Drenkhan et al., (2018) and define the downstream extent of the Vilcanota Watershed at Santa María (1,200 m.a.s.l.) within the department of Cusco. The Vilcanota Watershed is the second most glacierized tropical watershed on Earth, with approximately 1.3% of the watershed covered in glaciers

(Kronenburg et al., 2016; Drenkhan et al., 2018). Studies have established that in low latitudes, high elevation regions are warming disproportionately faster than lower elevation regions, and that the mean warming rate in the Tropical Andes from 1950 - 2010 was approximately 1.3^{o} C per decade (Bradley et al., 2006; Vuille et al., 2008; Drenkhan et al., 2015). Similar to other glacierized regions in the Tropical Andes, the extent of glacierized area in the Vilcanota Watershed decreased by 37.3% between 1988 and 2016 (Drenkhan et al., 2018). From 1965 to 2009, Vilcanota Watershed average annual temperature and precipitation showed greater variability in decadal trends than the Santa River Watershed, located further north at a latitude of ~9^{o} S; however, decadal climate trends were weak and within the bounds of uncertainty (Drenkhan et al., 2015). Substantial uncertainty in how regional water resources will be impacted by climate change is amplified by a lack of baseline *in-situ* hydrologic studies in the seasonally dry Vilcanota Watershed (Bradley et al., 2006; Vuille et al., 2008; Buytaert et al., 2009, Celleri et al., 2010; Drenkhan et al., 2015). There is a fundamental need to establish regional hydrologic baselines with *in-situ* data that can be used to guide water management and development initiatives (Bradley et al., 2006; Drenkhan et al., 2015).

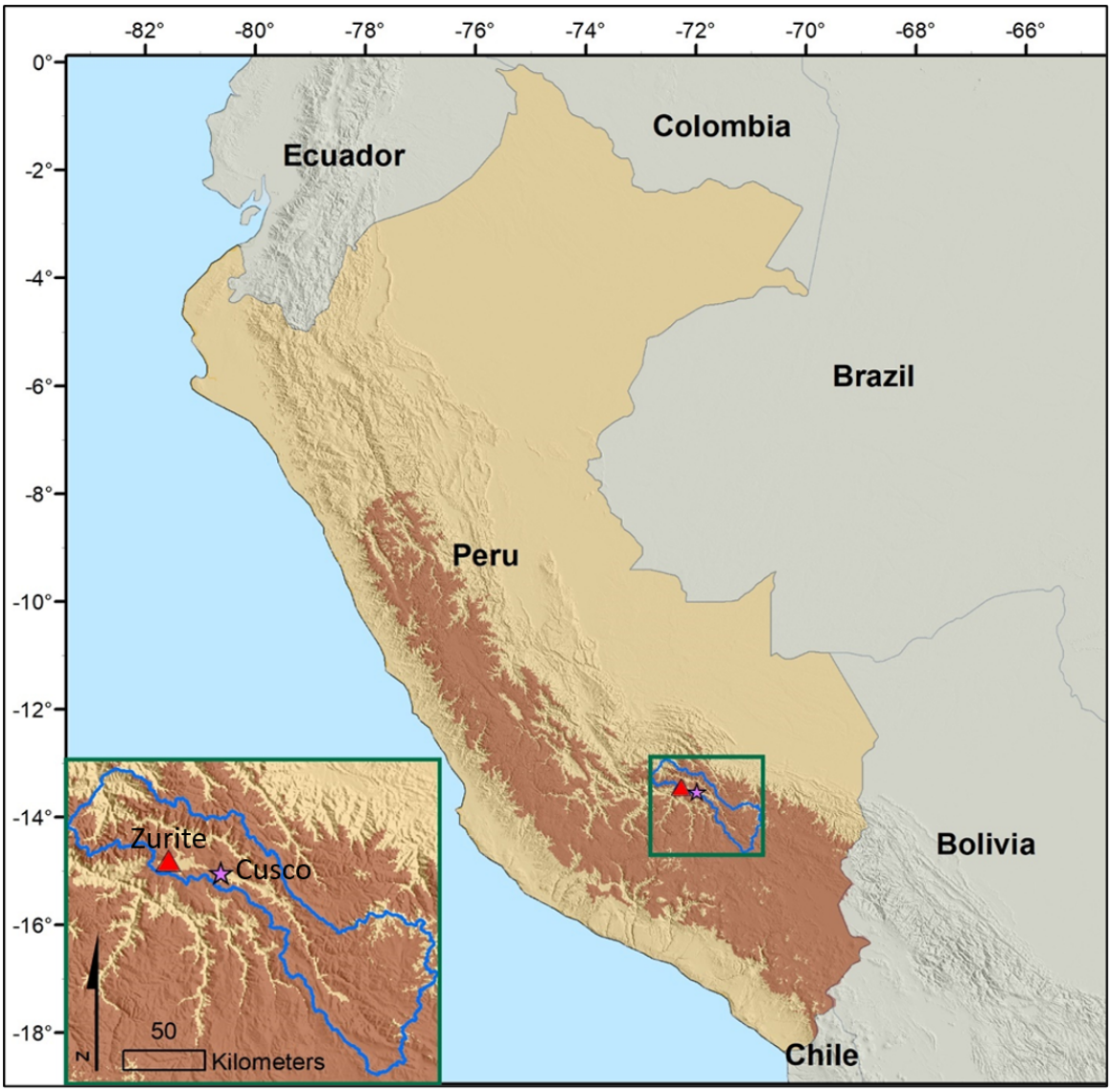

Figure 1. Map of western South America showing location of Perú and the field area. The brown-shaded region shows the extent of the *puna* in Perú – a seasonally dry tropical alpine grasslands ecosystem - from Ochoa-Tocachi et al. (2016). The regional capital of Cusco is represented by the purple star and Zurite and the Upper Ramuschaka Watershed (URW, drainage area: 2.12 km^2, latitude: -13.42416, longitude: -72.26889, mean elevation: 4332 m.a.s.l) are represented by the red triangle. The blue outline marks the boundary of the Vilcanota Watershed drainage (drainage area: 11,048 km^2) that the subbasins in the district of Zurite are nested within.

Daily median runoff from 1958 to 2013 at the 'km 105' gaging station (Upper Vilcanota River, drainage area: 9,160 km^2) operated by the hydroelectric company Empresa de Generación Eléctrica Machupicchu S.A. (EGEMSA) show runoff to be driven by seasonal precipitation patterns, peaking between January and March, and declining from April to October (Drenkhan et al., 2015). The percentage of glacier meltwater in streams decreases rapidly with distance from the glacier terminus, and accounts for less than 2% of annual discharge in the Vilcanota River as it flows through the Sacred Valley (drainage area: ~ 8,500 km^2), north of Cusco (Buytaert et al., 2017). Although the runoff pathways have yet to be studied, the primary source of runoff in the Vilcanota Watershed likely comes from the humid puna, which covers 78.2% of the Vilcanota Watershed (Figure 1) (Josse et al., 2009; Ochoa-Tocachi et al., 2016). The humid puna is a high elevation grass- and xerophytic shrub-land ecosystems that exists at the altitudinal extremes of plant life just below the permanent snow line (Figure 1) (Squeo et al., 2006; Josse et al., 2009; Fonken, 2014; Ochoa-Tocachi et al., 2016).

There are approximately 1,000,000 people living in the Vilcanota Watershed (Drenkhan, 2015) and up to 20% are without a stable water supply (INEI, 2017). Most communities rely on surface water draining from the humid puna landscape. Cusco, the largest city and department capital (population 400,000), sources up 90% of its potable water from two sources that are supplied predominantly from humid puna drainages: Laguna Piuray and the Vilcanota River in the Sacred Valley (Josse et al., 2009; Ochoa-Tocachi et al., 2016; Buytaert et al., 2017; SEDACUSCO EPS, 2019). Glacier recession in the Vilcanota Watershed has been the focus of significant research efforts (Kaser et al.,

1999; Vuille et al., 2008; Rabatel et al., 2013; Drenkhan et al., 2015; Kronenberg et al., 2016; Drenkhan et al., 2018; Vuille et al., 2018), however, there are no studies that have quantified water resources in the humid puna of the Vilcanota Watershed, despite the current importance in supplying freshwater to population centers and projections of humid puna expansion into glacierized area (Josse et al., 2009; Tovar et al., 2013; Drenkhan et al., 2015; Buytaert et al., 2017; Drenkhan et al., 2018).

Puna Extent and Water Yield

The puna biome covers an estimated 33.7% of the tropical Andes and can be found at elevation ranges from 2,000 – 6,000 m.a.s.l. (Josse et al., 2009). The puna biome is divided into at least two subsystems based on annual precipitation (Squeo et al., 2006; Tovar et al., 2013; Ochoa-Tocachi et al., 2016): the humid puna, which extends from eastern and central Perú (~ 8^{o} S) into the northeastern Bolivia Cordillera (~15^{o} S) and receives an average annual precipitation exceeding 500 mm (Squeo et al., 2006; Ochoa-Tocachi et al., 2016); and the xeric puna, which ranges from the extent of the humid puna in western and southern Perú and western Bolivia into northeastern Chile and northwestern Argentina (~20^{o} S) and receives less than 500 mm annual precipitation (Squeo et al., 2006; Josse et al., 2009; Ochoa-Tocachi et al., 2016). The humid puna covers an area of approximately 236,220 km^2 and the xeric puna 191,770 km^2, comprising 18.6% and 15.1% of all land cover of the tropical Andes, respectively (Josse et al., 2009; Tovar et al., 2013). An estimated 21.6% of glacierized and cryoturbated land area in the Tropical Andes will be replaced by humid puna and 35.4% by xeric puna

ecosystems from 2010 to 2039 under Intergovernmental Panel on Climate Change (IPCC) carbon emissions scenario A1B (between 1^{o} C and 1.5^{o} C projected regional temperature increase by 2039) (Tovar et al., 2013). Severe emissions scenarios and projections further into the future both indicated significantly greater replacement of glacierized and cryoturbated land area in the Tropical Andes by humid and xeric puna (Tovar et al., 2013). These projections underwrite a crucial water security need to quantify water resources from glaciated puna catchments in a framework that can capture changes to upland annual water balances over time (Bradley et al., 2006; Drenkhan et al., 2015; Buytaert et al., 2017). The sole study of catchment water yield in the puna assessed the impacts of land use on paired tropical headwater catchments, including four from the puna of central Perú to central Bolivia, (Ochoa-Tocachi et al. 2016). These data provide important catchment scale baseline data but do not reveal spatial patterns in water yield associated with the structure of the puna.

Structure of the puna

The humid puna biome encompasses five distinct ecosystems and covers an expansive area (Figure 1) (Josse et al., 2009). There are archetypical commonalities in the structure of the humid puna landscape present throughout the range, including complex topography with steep hillslopes, prominent local ridges, and significant outcropping of local geologic units (Josse et al., 2009; Oliveras et al., 2014; Ochoa-Tocachi et al., 2016). While plant cover of the humid puna can vary considerably between ecosystems, commonalities include a high alpine belt that is dominated by perennial tussock grasses, a low alpine belt that is largely dominated by perennial tussock grasses with sparsely

distributed woody shrubs, and a subalpine belt where native woody shrubs may be found at higher densities amongst tussock grasses on hillslopes, along watercourses, and in protected gullies (Squeo et al., 2006; Josse et al., 2009).

Recent studies in upland puna grasslands have measured extraordinarily high net primary productivity rates of tussock grasses (i.e., plant growth rates above and below ground) and high organic carbon stocks in hillslope soils (Oliveras et al., 2014; Yang et al., 2019; Yang et al., 2020). The high primary productivity rates and soil organic carbon stocks in hillslope soils generally results in high infiltration and water retention capacities of puna uplands (e.g., Harden and Scruggs, 2003; Abdelnour et al., 2011), and highlights the role of puna grasslands as an important regional carbon sink (Yang et al., 2018; Oliveras et al., 2014; Yang et al., 2020).

Valley bottoms and topographic low points of humid puna catchments are often filled with quaternary deposits of fluvial, glaciofluvial, and/or colluvial origin (Josse et al., 2009; Somers and McKenzie, 2020), which integrate upslope contributions of groundwater and host peat-forming alpine wetlands known as *bofedales* (singular: '*bofedal*') (Squeo et al., 2006; Josse et al., 2009; Fonken, 2014; Salvador et al., 2014).

Bofedales – landscape reservoirs of the puna

Bofedales are seasonally or perennially saturated alpine wetlands within the puna found in topographic depressions, valley bottoms, along watercourses, and in relatively low-gradient topography (Squeo et al., 2006; Salvador et al., 2014; Fonken, 2014). *Bofedales* have high edaphic humidity throughout the year and a hydrophytic plant assemblage that is distinct from other ecological communities of the puna (Squeo et al.,

2006; Josse et al., 2009; Salvador et al., 2014; Fonken, 2014). Tropical alpine conditions create vigorous hydrophytic plant communities that are often peat-forming when hydrologic conditions permit (Earle et al., 2001; Chimner et al., 2003; Cooper et al., 2010; Segnini et al., 2010; Fonken, 2014; Salvador et al. 2014; Cooper et al., 2015).

Although peat-forming, *bofedales* differ from temperate peatlands that have been the extensive focus of research due to their intricate links to alpine groundwater, unique hydrophytic vascular plant communities (i.e., they are generally not comprised of bryophytes such as sphagnum moss), and locations at the altitudinal extremes of vascular plant survival (Earle et al., 2003; Fonken, 2014; Salvador et al., 2014; Cooper et al., 2019; Valois et al., 2020). *Bofedales* share similarities to alpine wet meadows and fens that are often in areas of quaternary deposition and serve as an interface between the hillslope groundwater system and watercourses (Squeo et al., 2006; Fonken et al., 2014; Salvador et al., 2014; Cooper et al., 2019; Glas et al., 2019; Somers and McKenzie, 2020; Valois et al., 2020). However, they differ in that they have amongst the highest measured rates of both carbon/peat accumulation and lateral terrestrialization of low energy water bodies on Earth (Earle et al., 2003; Chimner et al., 2003; Cooper et al., 2010; Segnini et al., 2010).

Numerous studies have characterized *bofedal* ecology and qualitatively assessed the hydrologic function of *bofedales* (Cooper et al. 2014; Fonken 2014, Salvador et al. 2014; Polk et al. 2019). Loss of glacier area in the Cordillera Blanca was associated with increases in wetland area – suggesting a landscape evolution link between glacier recession and the formation of *bofedales* (Polk et al., 2017). In a similar, albeit wetter

tropical alpine grassland system with less precipitation seasonality in the Ecuadorian Andes called the 'páramo', the aerial extent of wetlands was positively correlated to annual runoff (Mosquera et al., 2015). No such spatial analysis of nested subbasins has been conducted for *bofedales* in the puna to our knowledge. However, it has often been suggested that *bofedales* capture, store, and release water and thus play in important role in sustaining streamflow in upland catchments (Earle et al., 2003; Fonken et al., 2014; Salvador et al., 2014; Drenkhan et al., 2015). We are aware of only two published studies that identify the water source of *bofedales* and quantify *bofedal* storage capacity (Cooper et al., 2019; Valois et al., 2020). A groundwater monitoring study of 10 streamside *bofedales* distributed throughout southern Perú and Bolivia determined that groundwater flow from adjacent hillslope or quaternary deposition-linked aquifers was the primary water source of *bofedales*, and that there was no measurable input from streamflow or glacier meltwater (Cooper et al., 2019). In the xeric puna of northern Chile, a three-dimensional model of a *bofedal* constructed from geophysical and core extraction surveys was the first study to estimate *bofedal* storage capacity (Valois et al., 2020); however, they did not make a distinction between total theoretical storage capacity and *bofedal* seasonal dynamic storage that might contribute to streamflow. The studies of Cooper et al. (2019) and Valois et al. (2020) support an interpretation that *bofedales* serve as an interface between the hillslope groundwater and streamflow systems and have a substantial storage capacity; however, the seasonal dynamic storage of *bofedales* has yet to be assessed and streamflow contribution dynamics from *bofedales* remain poorly understood (Drenkhan et al., 2015).

Zurite Water Supply and Security

Zurite, Perú is a rural district of 3,640 inhabitants (*Municipalidad Distrital de Zurite*, 2017) located at an elevation of 3,405 m.a.s.l in the province of Anta within the Vilcanota Watershed (Figure 1). The community of Zurite relies entirely on puna derived water resources for agricultural and municipal use. Mean annual precipitation from 1981 to 2019 was 855 mm (Aybar et al., 2020), 95% of which typically falls between October and April, with the remaining 5% between May and September (Figure 2) (Aybar et al., 2020). Zurite, like much of the high elevation tropics, receives relatively consistent solar radiation levels year-round, with differences in temperature between day and night generally exceeding mean seasonal temperature differences (Ochoa-Tocachi et al., 2016; SENAHMI, 2020). The primary limiting regional constrain on agricultural crop production is water, which is severely limited from May to September (Figure 2).

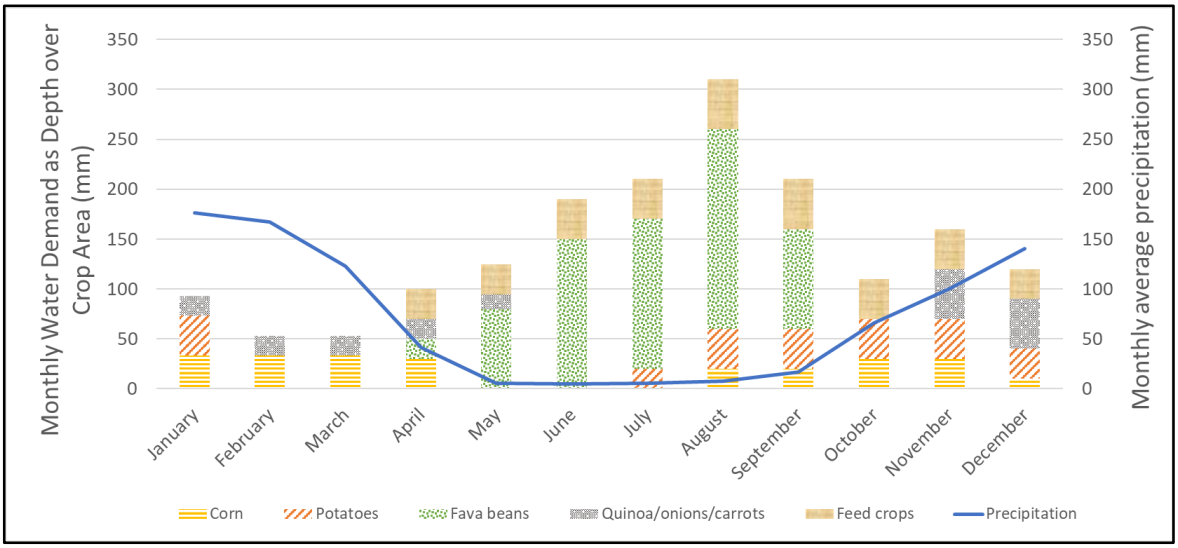

Figure 2. Annual crop seasons with estimates of monthly irrigation depth required per-unit-area of staple crops (*Zurite Comisión de Regantes de Agua*, 2020). Crop selection is often rotated between chacras (the local name for small, cultivated plots), such that not all agricultural land is cultivated at any given time. The blue line represents historical mean monthly precipitation from 1980 – 2020 (SENAHMI, 2020). The austral summer (December, January, and February) receives adequate precipitation to meet crop irrigation demand, whereas water demand in the austral winter (June, July, and August) substantially exceeds water supplied from precipitation to produce thirsty crops. Crops grown during the transition months between the summer and winter require limited irrigation, however precipitation is most variable in the transition seasons, which also correspond to critical crop cycle windows of planting and harvesting.

Life and livelihood in Zurite are intricately tied to agricultural production. Most families own and/or operate at least one plot of land where they practice some degree of subsistence farming primarily focused on corn, wheat, potatoes, quinoa, fava beans, and forage for animals. The *Municipalidad Distrital de Zurite* (2017) reports total cultivated land area in the district to be 1,206.5 hectares (ha), of which 851.6 ha are irrigated and 354.9 ha are dry farmed. Water supply during the dry season, from approximately May

through September, has historically constrained Zurite crop cultivation by up to 50% of the potential cultivated area if water availability constraints were alleviated with additional supply (Regional Government of Cusco, 2013). While perennial streams and groundwater springs from the immediate uplands supply a portion of Zurite's dry season water needs, corn, potatoes, quinoa, carrots, and onions grown primarily in the wet season comprise up to 93% of annual crop production, most of which is corn and potatoes (Table 1). There is a deficit between mean monthly precipitation and monthly water demand of staple crops grown in Zurite – establishing a clear need to irrigate during the dry season (Figure 2). Photographs taken from the peak of San Cristóbal looking out over Zurite and the Anta Plain in both the wet and dry seasons highlight the dramatic seasonal difference throughout the year, where the few green plots during the dry season are those with access to irrigation water (Figure 3).

Table 1. Estimates of major crop percentages grown annually in Zurite (*Comisión de Regantes de Agua*, 2021).

Crop	**Amount grown in a typical year (%)**	**Primary season of crop cultivation**
Corn	80	Wet
Potatoes	10	Wet
Fava beans	3	Dry
Quinoa/onion/carrot	4	Wet
Other cereal grains	3	Dry

Figure 3. Photographs of Zurite and the Anta Plain taken from the peak of San Cristobal mountain show the extreme contrast between the wetter austral summer (top) and the drier austral winter (bottom). The town of Zurite, located in the lower right corner of the two photos, is situated on the alluvial fan of the Ramuschaka watershed. The need for dry season irrigation is highlighted by sparsely cultivated green plots during the dry season. Photo credits: Jasper Oshun.

Surface water storage for irrigation amounts to 10,500 m^3 across five open reservoirs. Water reservoirs are drained daily during the dry season in a rotational system to serve the needs of water users in the community (*Zurite Comisión de Regantes de Agua*, 2020). The community has no long-term water storage and is thus vulnerable to prolonged drought. Irrigation systems in Zurite consist of an extensive network of canals that rely primarily on gravity to deliver water. Most crop irrigation is administered by flooding cultivated plots; however, a recent exception is a pilot project involving five families to improve water use efficiency via sprinkler irrigation systems (*Zurite Comisión de Regantes de Agua*, 2020).

Rural water security has been recognized as a priority by the regional government of Cusco with initiatives such as Plan MERISS (*Plan de Mejoramiento de Riego en Sierra y Selva*, 'Plan to Improve Irrigation in the Mountains and Rainforest' in English). Plan MERISS includes the Sambor-Huaypo project, completed in 2010, which resulted in four reservoirs and canal infrastructure to deliver water to approximately 5,800 agrarian families amongst 15 communities (Regional Government of Cusco, 2020). The agricultural community of San Nicolas de Bari, located in the eastern sector of Zurite, receives approximately 6,000 to 8,000 m^3/day at the terminus of one branch of the Sambor-Huaypo network (*Zurite Comisión de Regantes de Agua*, 2020). By increasing dry season irrigation water supply, the project has alleviated water constraints that had limited crop cultivation in San Nicolas de Bari by up to 50% (Regional Government of Cusco, 2013; *Zurite Comisión de Regantes de Agua*, 2020). Sambor-Huaypo has been instrumental to expanding dry season agriculture and improving water security in Zurite;

however, rugged topography and a long transport distance have led to interruptions in water supply due to landslides and infrastructure repair - the cost of which is borne by the beneficiary communities (*Zurite Comisión de Regantes de Agua*, 2020). Since the completion of Sambor-Huaypo, landslides have resulted in months without adequate irrigation water during critical windows in annual crop cycles (*Zurite Comisión de Regantes de Agua*, 2020).

Zurite and the Upper Ramuschaka Watershed

The setting in Zurite parallels many agrarian communities throughout the Andes that rely on water supply from the humid puna. Citizen participation in agricultural and water management decisions, widescale subsistence farming practices, and its location on the alluvial fan of a humid puna catchment make Zurite an ideal locale to directly link hydrologic productivity from a humid puna catchment within the Vilcanota Watershed to agrarian water demand. The structured landscape above Zurite is both typical of puna uplands and offers an opportunity to connect water resources to landscape features.

Zurite and the surrounding agricultural fields are spread across the alluvial fan of the Ramuschaka Watershed, a 5.0 km^2 high-relief catchment (mean slope: 38.6%) that drains into a 10 km by 30 km dry Pleistocene lakebed filled with lacustrine sediments known as the Anta Plain (Figure 3, Figure 4) (Carlotto, 2010). The Ramuschaka Watershed is the primary local water source for Zurite. Whereas the upper parts of the watershed are within the humid puna, eucalyptus forests are present below 3800 m.a.s.l., in the immediate uplands adjacent to Zurite (Figure 4). The Upper Ramuschaka Watershed (URW) is a minimally disturbed 2.12 km^2 headwater catchment that is

characteristic of the humid puna. The URW is bounded by steep headwalls of exposed bedrock or covered in the perennial tussock grass *Jarava ichu.* Low gradient subbasins within amphitheater uplands of the URW host seasonally saturated *bofedales*. The outlet of the URW is a perennial stream that is sometimes diverted via a concrete weir (at 4,011 m.a.s.l.) and interbasin canal for irrigation in the eastern agricultural sector of Zurite (Figure 4).

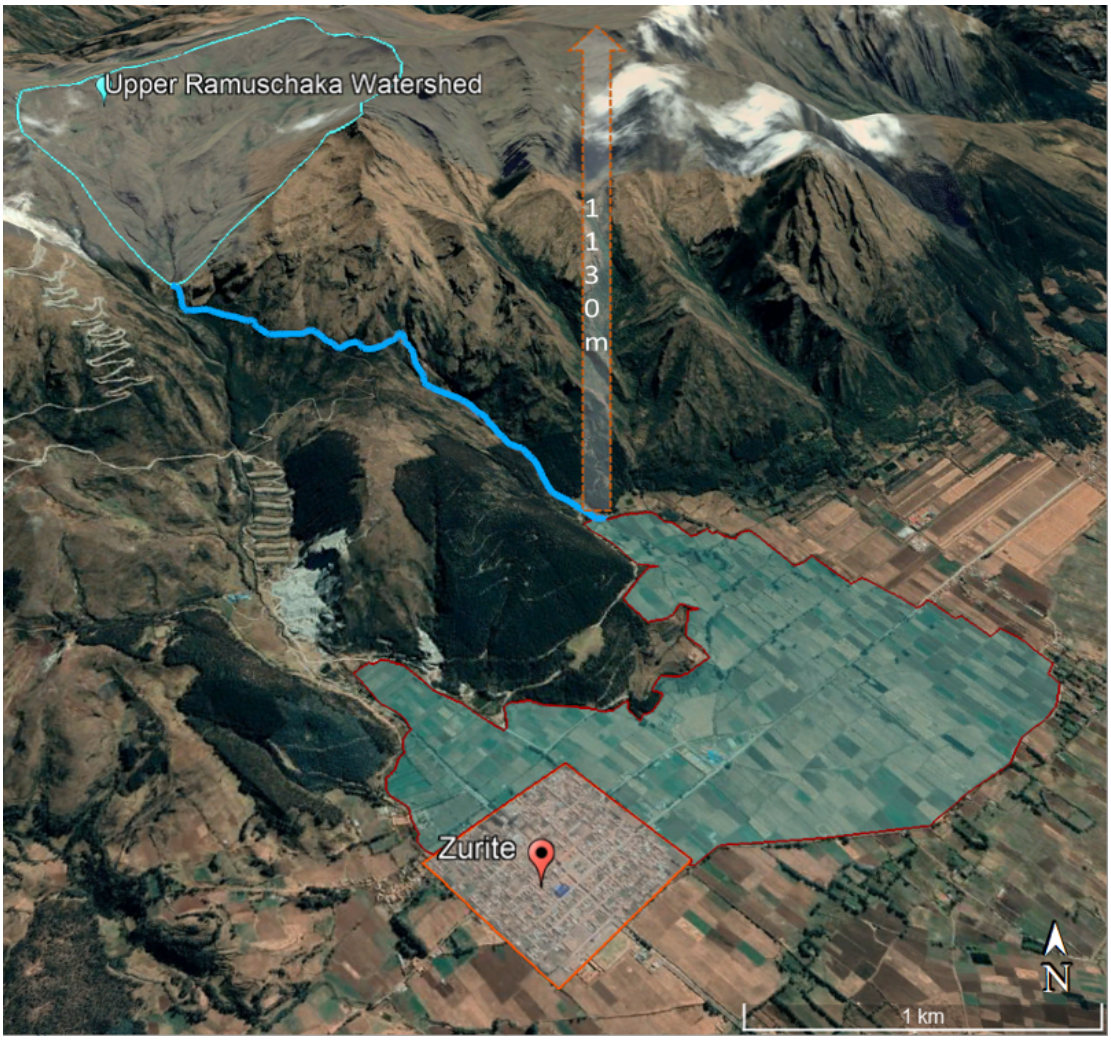

Figure 4. Zurite and surrounding agricultural fields are located on the alluvial fan of the Ramuschaka Watershed. The URW is located approximately 1000 vertical meters above the town of Zurite. An interbasin water canal (blue line) diverts surface water from the URW to the adjacent drainage for agricultural use. The blue shaded region represents the approximate agricultural area (181 ha) that derives irrigation water from the URW. Note the perspective of the Google Earth Image alters scale with distance.

Our study seeks to quantify water resources yielded from the URW and the spatiotemporal dynamics of runoff generation within the URW. We have four overarching research questions that drive our hydrologic methods and analyses:

1) How much water does the humid puna yield?

2) What are the temporal phases of the annual URW water balance?

3) What are the spatiotemporal patterns of water yield in the URW?

4) What is the dynamic seasonal storage capacity of *bofedales* and how much water might they contribute to dry season runoff?

To investigate these questions, we developed an annual water balance for water years 2019 and 2020 (henceforth referred to as WY2019 and WY2020, respectively) and present monthly water yield from the URW for comparison to monthly estimates of irrigation demand in a typical agricultural year. We hypothesized the structure of land cover in the URW, particularly the presence of *bofedales*, would lead to differences in unit runoff. To test our hypothesis, we designed an experiment with 12 campaigns to measure discharge in nested subbasins throughout the URW spanning June 2019 through January 2021.

Finally, we use a combination of monitoring wells, five *bofedal* transects of borehole observations, borehole nuclear magnetic resonance (NMR) measurements, and geospatial interpolations to estimate the drainable portion of seasonally dynamic water storage that might contribute to streamflow in cross-sections of four *bofedales* in the URW. This is the first study to our knowledge that:

a) Uses a spatiotemporal approach of spatially distributed discharge measurements of nested subbasins throughout a headwater humid puna catchment to relate runoff processes and spatial dynamics of watershed yield to the presence and spatial distribution of *bofedales*.

b) Uses NMR methods paired with borehole observations to estimate the *bofedal* seasonal dynamic water storage capacity that might contribute to streamflow, and links *bofedal* storage estimates to catchment-scale hydrology - both quantitatively and with a conceptual model.

c) Explores water yield from a seasonally dry headwater humid puna catchment in the context of agrarian water needs directly downstream.

The results of our study highlight the importance of *bofedales* as landscape features that integrate upslope groundwater contributions which are seasonally stored in

peat and slowly released to streams through a low conductivity lower boundary, thus sustaining dry season runoff.

URW Site Description

The URW drains an area of 2.12 km^2 and spans an elevation range from 4,011-4,543 m.a.s.l. (mean elevation: 4,332 m.a.s.l.). The watershed boundary (Figure 5) is demarcated by the area draining to a concrete surface water diversion weir with a series of water gates dictating flow allocation between the Ramuschaka Watershed and an interbasin canal that drains to the eastern agricultural sector of Zurite (Figure 4). The URW has three subbasins – the Western, Central, and Eastern subbasins – each with perennial streams which form a confluence approximately 150 m upstream of the diversion weir (Figure 5). The dominant structural components of the humid puna that are present in the URW are outcropping and bare earth, upland tussock grasslands, *bofedales*, and areas with sparsely populated xerophytic shrubs. Broad patterns in local basin geomorphology and specific geomorphic features suggest the URW was sculpted by glaciations, perhaps as recent as the Holocene. Steep headwalls and low gradient basins typical of glacially carved cirques are found in the upper portions of all three subbasins, but most notably in the Central subbasin. All subbasins contain elongated morainal features which extend down valley and exhibit hummocky topography (Figure 6). We identified an esker in the upper part of the Central subbasin. We are not certain of how far downstream the glaciers extended; however, field evidence points to a lack of morainal

deposits, and a distinct narrowing of valleys from U-shape to V-shape around 4,200 m.a.s.l., suggesting this may have been the limit of glaciation.

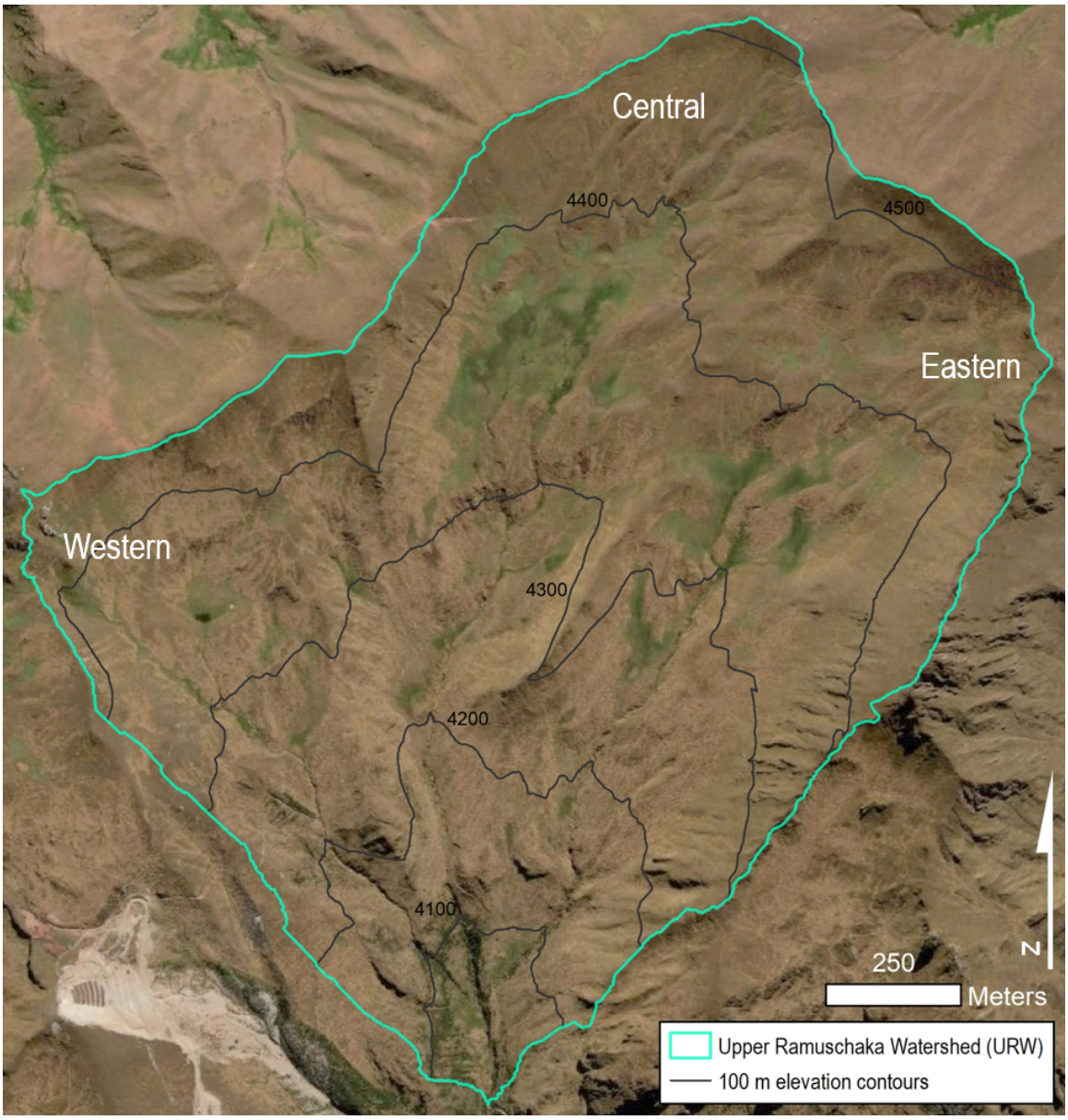

Figure 5. Aerial imagery of the URW with the watershed area that drains to the concrete diversion weir demarcated with a blue line. The total area of the URW is 2.12 km^2 and contains three subbasins – the Western, Central, and Eastern subbasins – from which perennial streams flow and form a confluence 150 m upstream of the diversion weir. The URW spans an elevation range from 4,011 to 4,543 m.a.s.l. (mean 4,332 m.a.s.l.). Elevation contours are shown in 100 m intervals.

The ecosystem and geology of the URW fits the description of 'high Andean and high mountain humid puna' described by Josse et al. (2009) due to the elevation range (between 4,000 – 4,600 m.a.s.l.), dominant grassland plant communities, and the presence of rocky outcrops and sparse woody shrubs; however, the URW also has components of 'High Andean and high mountain wetlands' (*bofedales*) in low-gradient areas that correspond with seasonal or perennial saturation, quaternary deposition, and a distinct hydrophytic plant assemblage.

Outcropping and bare earth in the URW correspond to the regionally predominant geologic units. There are Eocene sedimentary units of limestone, sandstone, and mudstone throughout the URW. The limestone unit is found exclusively in the Western subbasin of the URW and is light- to dark-grey, fine-grained, massive and cliff-forming. It is highly fractured in outcrop with karst weathering. The sandstone unit, found throughout the URW, is hard, fine-grained to conglomerate, cliff-forming, and ranges from medium-thickness bedding to massive structure. The sandstone unit includes a sugary-white crystalline quartzite that forms a boundary between the upper Eastern and Central subbasins. The mudstone is sheared, weak, abundantly fractured, and slumping to slope-forming. It is friable in outcrop and presents as red, greenish-grey, or a beige-brown color. There are Oligocene age intrusive outcrops in the Western subbasin that were determined to be quartz monzodiorite (Carlotto et al., 2010). The quartz monzodiorite unit presents as fine- to medium-grained and is light to medium grey. Quartz monzodiorite phenocrysts include plagioclase, hornblende, biotite, quartz, alkali

feldspar, and secondary epidote. Outcrops of the quartz monzodiorite are typically weathered to the point of saprolite.

Figure 6. The largest *bofedal* wetland is the extensive green area occupying the valley bottom of the upper Central subbasin. The marked color difference between the hillslopes, dominated by *Jarava ichu*, and the verdant green of the *bofedal* is a product of hydrologic conditions that allow for a shallow groundwater table, year-round edaphic humidity, and a hydrophytic plant assemblage. Photo taken from approximately the 4,400 m elevation contour on the ridge dive between the Western and Central subbasins and looking to the NE. Photo credit: Jasper Oshun, June 2019.

Upland tussock grasslands are found on local hillslopes and ridges that are heavily dominated by the perennial bunchgrass *Jarava ichu* (Figure 7). Other grasses of the plant genera *Agrostis*, *Calamagrostis*, and *Festuca* can be found along watercourses and in transitions between hillslopes and low-lying *bofedales*. Upland areas generally have a well-developed A horizon up to 40 cm deep that is dark brown, organic-rich, and generally has high silt and clay content. Underlying subsurface layers typically show increased proportions of weathered bedrock clasts, often intermixed in a red silt and clay-

rich matrix to a depth of approximately one m. The maximum depth of upland plant roots is approximately 1.3 m and generally corresponds with the depth of saprolite.

Figure 7. The puna is characterized by rugged topography, steep slopes, and extensive upland perennial grassland cover. Topographic low points, depressions, and watercourse banks host *bofedales* – unique high alpine wetlands with distinct hydrophytic plant assemblages. These wetlands produce peat with extraordinary water storage capacity and are hypothesized to be important hydrologic features of the puna landscape. Photo taken from a hillslope in the Central subbasin looking N-NE with a DJI Phantom 4. Photo credit: Nick Hawthorne, June 2018.

Bofedales in the URW occur in relatively low-gradient topography that is seasonally or perennially saturated (Figure 6). *Bofedales* of the URW are characterized by a hydrophytic plant community with dominant plant species that include *Distichia*

*muscoide*s, *Oxychloe andina*, and *Plantago tabulosa* – fitting the description of *Distichia* peatlands presented by Fonken (2014) - and may be situated on a highly porous peat layer up to 1.7 m thick. There is typically a layer of fine, very plastic, red quaternary clay and silt sediments (likely glaciofluvial lacustrine deposition) overlying red to red-brown sandstone and/or mudstone clasts intermixed in a clayey matrix. Grey streaking and small sugary-crystalline grey sandy clay pockets can be found intermixed throughout the clayey matrix.

Xerophytic shrubs are found in the lower reaches of the URW, where the highest shrub densities occur near watercourses. Shrub typically do not exceed two m in height Dominant shrubs are from the genera *Baccharis*, *Bereberis*, and *Polylepis,* however, woody shrubs of the families *Asteraceae* and *Solanaceae* can also be found in lower reaches of the URW.

Contemporary land use of the URW is light due to the extreme relief and significant travel distance from any nearby population centers. The primary URW land users are pastoralists grazing small herds of cattle, sheep, or goats in low grazing densities - generally less than 25 individual grazers - and small herds of wild horses. While contemporary human presence in the URW is sparse, anecdotal historical accounts of the URW suggest that there was cultivation of traditional Andean tuber crops and that uplands were used more frequently for extensive grazing in past decades – accounts that are corroborated by several relict stone corrals and apparent hand-dug drainage routes that can be found within the URW. These accounts fit the description of Andean uplands containing *bofedales* as ‘cultural landscapes’ that have been lightly maintained to

optimize the land for grazing and/or water supply (Baied and Wheeler, 1993; Fonken, 2014)

METHODS

Bonanza en los Andes Field Campaigns

We used a combination of methods (geospatial, hydrologic monitoring, and targeted field measurements) to quantify URW water yield, identify spatiotemporal relationships in URW water yield, and estimate potential streamflow contribution from *bofedales* in the URW. A portion of the data presented in this thesis was collected through a water development project titled *Bonanza en los Andes* - a two-year collaborative effort between academic collaborators at HSU and Rutgers University Newark and Zurite government entities (*Comunidad*, *Municipalidad Distrital de Zurite*, and the *Zurite Comisión de Regantes de Agua*). The goals of *Bonanza en los Andes* were to collaborate with the community of Zurite in the design and construction of 1.3 km of irrigation canals to support over 100 families, determine the water yield in the Andean puna, and train a cohort of students from the U.S. and Perú to be community-minded and interdisciplinary researchers.

I assumed a leadership role in *Bonanza en los Andes* that incorporated my Spanish fluency and project management skills to identify community and project needs, develop scientific questions and protocols, lead technical and logistical operations, and serve as a liaison between Zurite and *Bonanza en los Andes*. My role included four field campaigns to Zurite between June 2018 and January 2020, each ranging from two to five weeks in length.

Twenty-six graduate and undergraduate student participants from five academic institutions across the USA and Perú contributed to data collection in the URW during the summers of 2018 and 2019. Data collection efforts included seismic, electrical resistivity, and borehole nuclear magnetic resonance (NMR) geophysical surveys, unmanned aerial vehicle (drone) surveys, geologic mapping, and installation, maintenance, and data downloads from hydrologic monitoring equipment. The data collected in the *Bonanza en los Andes* research project incorporated in this thesis are described in detail below.

Additional field work and data download campaigns were led by Wilner Bandera Perez (Universidad Nacional de San Antonio Abad del Cusco (UNSAAC), undergraduate class of 2019, geology) every 30 to 120 days of WY2019 and WY2020, whom I trained in field methods and protocols. Mr. Bandera Perez downloaded water level and atmospheric logger data and measured discharge and stage height at each of the stream gage stations with each data download event, noting flow conditions, cable length and any data anomalies.

Geospatial Data Collection and Methods

URW land cover classification

We used *ENVI 5.5*, developed by L3Harris Geospatial, and 1-meter resolution Esri World Imagery of the URW to classify six initial land covers in the URW that we hypothesized would be linked to spatiotemporal patterns in water yield. We used a red, green, and blue (RGB) raster layer and example-based feature extraction in accordance

with the online resources, ‘Feature Extraction with Example-Based Classification Tutorial’ (L3Harris Geospatial, 2019) and ‘ENVI Feature Extraction Modile User’s Guide’ (ITT, 2008). We utilized a high merge level for image segmentation to reduce segmentation complexity and defined – ‘Bofedal’, ‘Upland’, ‘Outcrop’, ‘Steep relief’, ‘Lutita mudstone’, and ‘Shrubland’ according to their unique spectral signatures. We used the support vector machine (SVM) supervised classification algorithm to classify the image. We later quality controlled the land cover classification product manually to ensure quality delineation. Following quality control, we merged ‘Steep relief’, ‘Lutita mudstone’, and ‘Outcrop’ all under the ‘Outcrop’ as they all corresponded with exposed bedrock or bare earth features that were verifiable on the high-resolution imagery that we produced in *Agisoft Metashape Professional*, resulting in a total of four classes – ‘Bofedal’, ‘Upland’, ‘Outcrop’ and ‘Shrubland’. We converted the classified raster layer to polygon vectors in Esri *ArcMap 10.6 Desktop*, which were then used for hydrologic analyses that related land cover classification to hydrologic measurements in the URW. We present the land cover classification map product in the methods of this thesis to provide context for other analyses (Figure 8).

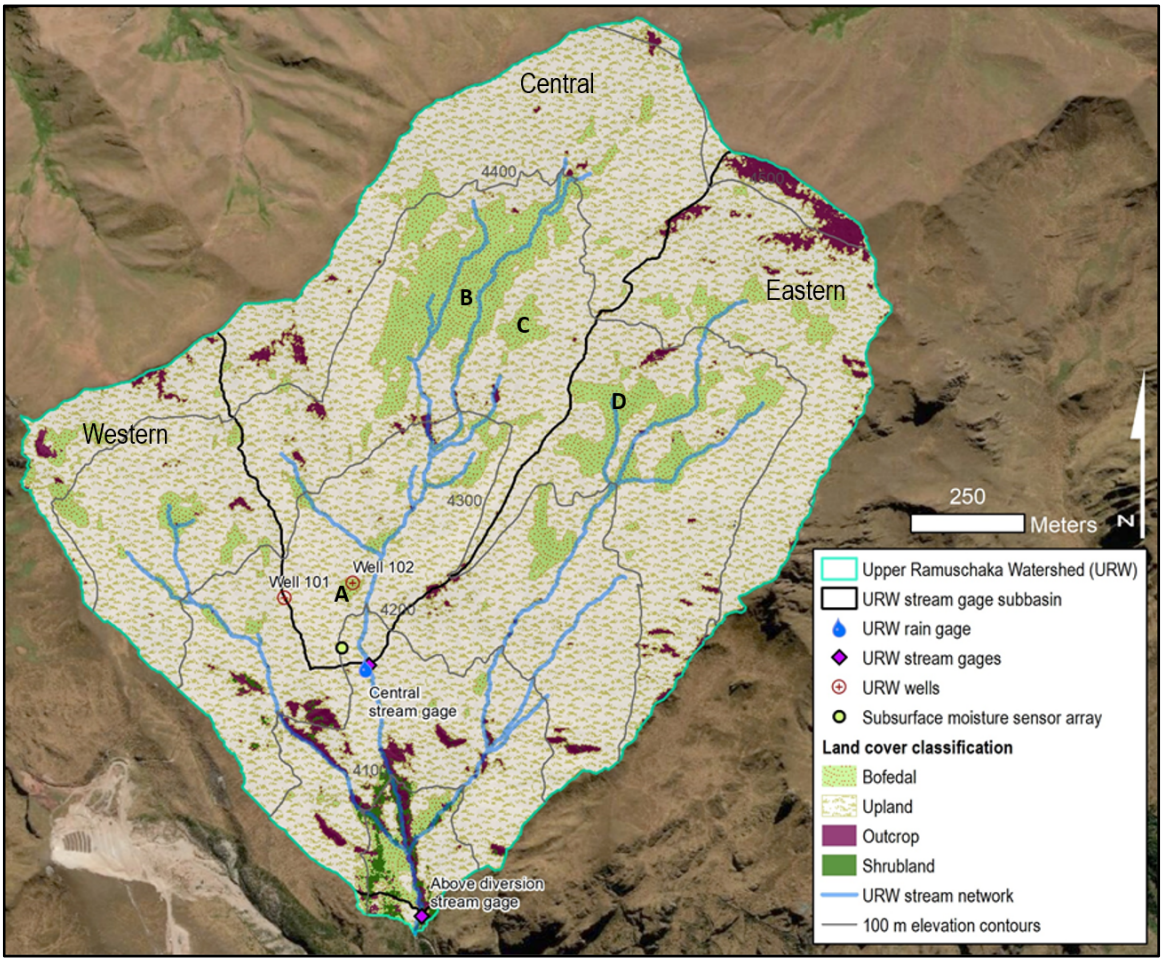

Figure 8. The Upper Ramuschaka Watershed (URW) is a 2.12 km^2 steep upland catchment with a mean elevation of 4,332 m.a.s.l. that is characterized as humid puna. Thick blue lines show branching up into each of the labeled subbasins in the URW from the outlet near the Above Diversion stream gage show the stream network. Monitoring instrument locations of the tipping bucket URW rain gage, subsurface moisture array, stream gages and monitoring wells 101 (local ridgetop) and 102 (*bofedal*) are shown over a land cover classification map. Land cover classification shows four classes that correspond with the structural components of the puna landscape: *bofedales*, upland grasslands, outcropping or bare earth, and shrubland. Bold letters 'A', 'B', 'C' and 'D' refer to specific *bofedal* wetlands surveyed with borehole transects to make estimates of dynamic storage.

Unmanned Aerial Vehicle photogrammetry survey

In June 2019, we flew a DJI Phantom 4 Pro Unmanned Aerial Vehicle (UAV) to collect photographic data of the URW. We conducted flight missions in compliance with Federal Aviation Administration (FAA) standards and regulations and Humboldt State University (HSU) requisites for drone operation. We planned and executed surveys using *MapPilot Terrain Awareness* software features (Drones Made Easy, 2019) and the 1 arc-second Shuttle Radar Topography Mission (SRTM) global digital elevation model (DEM) with 80% coverage overlap of survey areas at 200 feet elevation above the ground surface. Flight mission design, piloting, and ground control point (GCP) design and placement were conducted by Laurel Smith (B.S. Environmental Resources Engineering, HSU, 2019). We installed 26 GCPs throughout the 2.12 km^2 URW which we surveyed with an Eos Real Time Kinematic (RTK) Global Positioning System (GPS) to ground truth photogrammetric elevation products. Reported mean horizontal error on surveyed GCPs was 0.097 m and mean vertical error was 0.113 m.

UAV data processing and DEM production We used *Agisoft Metashape Professional* to post-process UAV surveys into 1-m/cell resolution DEM (Figure 9) and 8.3cm/pixel resolution orthomosaic products using protocols and recommendations from the online resources: 'Unmanned Aircraft Systems Data Post-Processing manual' (United States Geologic Survey, 2017) and 'Agisoft Photoscan Crash Course' (Dietrich, 2015). Data processing was conducted at the 'Medium' quality level, resulting in a DEM of 8.3-cm/cell resolution that we then down-sampled to 1-m/cell resolution for analysis. There were three small data gaps at the margins of the aerial surveyed area where the SRTM

DEM had erroneous cell values due to steep relief and was unable to provide adequate *Terrain Awareness* for topographic tracking of the UAV during survey. We filled these areas by up-sampling a 12.5-m/cell resolution DEM produced from the Advanced Spaceborne Thermal Emission and Reflection (ASTER) satellite and clipping and filling the margins in which there were holes in the 1-m DEM. The filled area was less than 500 m^2 (of 2.12 km^2 total URW area, primarily on the steep URW eastern ridge) and had no apparent impact on area estimates or hydrologic flow analyses. Figure 9 shows a hillshade made from the 1-m resolution DEM of the URW.

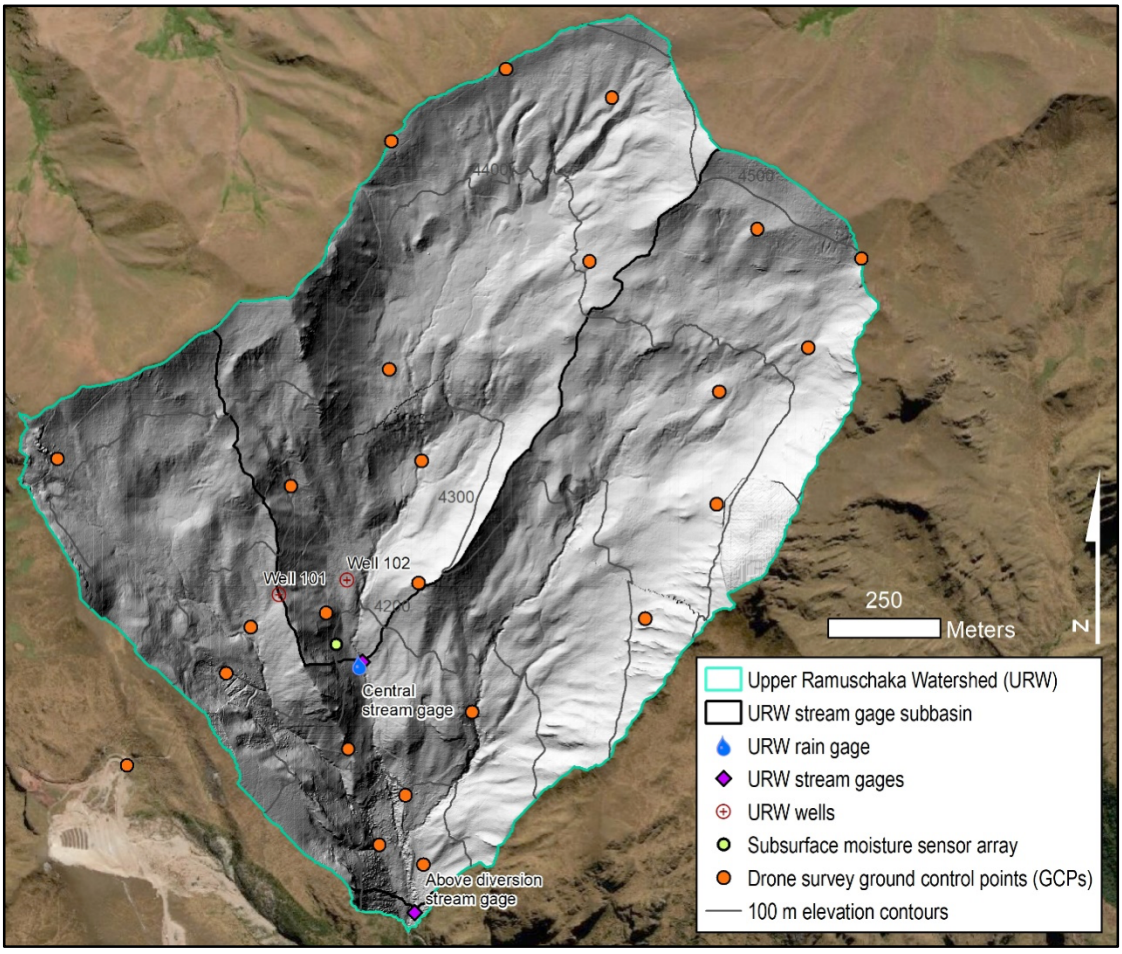

Figure 9. Hillshade map of the 1-m/cell resolution DEM of the URW produced with photogrammetric drone surveys flown in June 2019. Orange points are GCPs that were surveyed with an Eos Arrow Gold RTK GPS (1-4 cm accuracy). The locations of hydrologic monitoring instrumentation are shown on the hillshade map along with the subbasin delineations draining to each stream gage that were produced with the DEM used to create the hillshade layer. Broad, amphitheater valleys, depressions, and hummocky topography visible in the upper portions of the URW are relict geomorphic features of past glaciation and generally correspond to areas classified as 'Bofedal'.

Subbasin delineations, area calculations, and stream network rendering

We delineated watershed boundaries of streamflow gaging stations and discharge points using the 1-m resolution DEM (Figure 9). We pre-processed the DEM for hydrologic analysis with *Whitebox Geospatial Analysis Tools (GAT)* (Lindsay, 2016) 'Breach Depressions (Fast)' tool (Soille, 2004; Wang, 2006), which forced continuous flow within the URW to the concrete diversion weir that marks the outlet of the URW. We opted for this tool over the Esri *ArcMap 10.6 Desktop* 'Fill sinks' tool for DEM pre-processing because it utilizes a more dynamic approach to removing sinks and dams within the DEM while minimizing DEM alterations, thus maintaining microtopographic features that are important within *bofedales*. All other watershed delineation steps followed standard protocol with Esri *ArcMap 10.6 Desktop* software 'Hydrology' toolset using the 'D8 Flow Direction' algorithm. We calculated watershed area measurements and the percentage of each watershed classified as 'Bofedal' using the ENVI land cover classification layer and standard Esri *ArcMap 10.6 Desktop* geospatial functions in projected coordinate reference system WGS84 UTM Zone 18S.

To accurately depict the URW stream network in geospatial products, we used the standard *ArcMap 10.6 Desktop* 'Hydrology' toolset with a flow accumulation threshold of 35,000 cells (i.e., 35,000 m^2). We settled on the 35,000-cell threshold in an iterative process of cross-checking the stream network against the URW orthomosaic produced with *Agisoft Metashape Professional* to ensure accurate representation of the URW stream channel network. The resulting stream network corresponded to the observed

perennial stream extent in the URW, however, also included ephemeral streams and former streams terrestrialized by *bofedales* in the smallest upland catchments (Figure 8).

Annual Water Balances

We estimated annual water balances of the URW to quantify annual and seasonal water yield that might satisfy downstream water demand via the following equation:

$$P = Q + ET + \Delta S$$

where P is annual elevation-adjusted precipitation of the subbasin (Appendix A), Q is runoff at either the Central or Above Diversion stream gage (Figure 8), ET is the sum of evapotranspiration from 'Upland', 'Shrubland', and 'Bofedal' land cover (Figure 8), and ΔS is an estimate of interannual water storage, subsurface drainage below measured stream runoff, or due to measurement error. Each of the instruments and associated data set processing steps used to measure the water balance components is described in greater detail in the 'Instrumentation, Surveys, and Data Processing' section, below. Uncertainty for each of the water balance components is reported as a '+/-' value in both mm and percentage in results.

Water year wet and dry seasons

We defined the water year from September 1 – August 31 of the following calendar year. The start of the annual water year corresponds with the end of the regionally dry austral winter and marks a gradual transition into the wet season. We distinguished the dry season as the period when cumulative 15-day precipitation at the

URW rain gage (Figure 8) was less than 10 mm. Conversely, the wet season began when cumulative 15-day precipitation was equal to or exceeded 10 mm.

Instrumentation, Surveys, and Data Processing

Hydrologic monitoring equipment was installed to measure annual water balance parameters in the URW. In this section, we describe the installation of each device as well as the data collection and data processing conducted to produce the annual water balances.

Geospatial survey equipment

We surveyed locations of equipment and points of interest using an Arrow Gold Eos real-time kinematic GPS unit (1-4 cm accuracy) or Garmin Legend H etrex handheld GPS units (reported 3-5 m accuracy). We used World Geodetic System 1984 (WGS84) datum and collected data in either decimal degree or Universal Transverse Mercator Zone 18 South (UTM 18S) coordinate reference system. Long-term equipment installations and points of high-accuracy importance - including stream gages, tipping bucket rain gages, wells, ground control points (GCPs) and geophysical surveys – were surveyed using the Eos RTK GPS system.

URW rain gage

Precipitation and air temperature were measured from June 2018 through January 2021 in the Central subbasin near the Central stream gage (Figure 8) using a HOBO Onset RG3 tipping bucket rain gage with 0.2 mm precipitation per event resolution (Figure 10).

Figure 10. The URW rain gage located in the Central subbasin near the Central stream gage at 4171 m.a.s.l. The URW rain gage measured precipitation from June 2018 until January 2021. An identical rain gage was also installed in the town of Zurite.

Subsurface moisture sensor array

Seasonal subsurface moisture dynamics in a hillslope were measured with a moisture sensor array installed along the rooting depth profile of the dominant upland bunchgrass – *J. ichu*. We used the subsurface moisture sensor array to estimate upland ET in the URW. We installed four Teros-12 volumetric water content (VWC) sensors horizontally in the upslope face of undisturbed soil and saprolite of a 10.5 cm diameter auger hole (Location in Figure 8, photograph of hillslope in Figure 11). Sensors were installed at depths of 20 cm, 60 cm, 90 cm, and 120 cm in accordance with recommended installation procedures (Appendix B, Figure 38 shows schematic of installation) (Meter Group Inc., 2018). Once installed, columns were backfilled and lightly tamped. VWC, temperature, and electrical conductivity (EC) were recorded by the Teros-12 sensors every 15-minutes from January 2019 through August 2020.

Subsurface sensor depth ranges and material observations We calculated mm of moisture gained or lost over the sensor profile by assigning depth ranges to each sensor. The depth range for the 20 cm sensor was 0 to 40 cm and measured moisture of the well-developed A horizon that was a dark brown clayey silt loam with abundant coarse and fine roots from nearby *J. ichu* grasses. The 60 cm sensor depth range was from 40 to 75 cm and measured the B horizon, which had mixing of the dark brown clayey silt loam with red clay pockets, and some red angular sandstone and mudstone weathered bedrock clasts intermixed with medium-density fine roots, ranging from 1-2 mm diameter. The 90 cm sensor range was 75 to 105 cm and measured moisture of the B/C horizon gradient, which was a transition from primarily red clay with light grey clay/mineral pockets and

angular sandstone and mudstone clasts up to 35 mm diameter intermixed with very few fine roots down to wet, red medium-grained clayey sand with intermixed angular sandstone and mudstone clasts up to 40 mm in diameter. The 120 cm sensor depth range was from 105 cm to 135 cm and measured saprolite comprised mostly of coarse-grained sand with angular sandstone clasts up to 40 mm, clayey pockets intermixed, and no visible roots at the lower end of the range. Observations along roadcuts confirmed the maximum rooting depth of *J. Ichu to* be approximately 120 cm.

Figure 11. The Meter Group subsurface moisture sensor array on a hillslope of the Central subbasin. The data logger and cables are protected with a makeshift cage to prevent wire damage from rodents in the URW. The moisture sensors measure VWC at depth intervals along the rooting zone of the dominant bunchgrass – *J. ichu* the abundant green grass throughout the URW upland. Photo taken in January 2020.

Subsurface moisture array ET estimates

Field capacity is the maximum water content of a freely drained media (e.g., Abdelnour et al., 2011). We estimated field capacity to be the mean value of the mode histogram bin for each sensor over the wettest period of the WY2020 wet season, from January 31 – April 8, 2020 (Appendix B). While our method relied on a simple interpretation of subsurface moisture dynamics during the wet season, the resulting field capacity estimates occurred in similar slope-break positions in the VWC time series as field capacity estimates made with VWC sensors in experimental settings (Bean et al., 2018). We assumed that all increases in VWC beyond field capacity would cause vertical drainage below the depth of the sensors and lead to either increased moisture content in unsaturated weathered bedrock, or a rise in groundwater. We assumed that all decreases in VWC below field capacity were due to ET. We calculated daily losses in VWC per sensor and used a conditional function in *Excel* to estimate daily ET loss if below the field capacity threshold. We summed the daily VWC difference across all layers and distributed the loss in VWC per-layer to estimate daily ET across the vertical profile in mm/day. ET estimates were derived from the product of VWC decline below field capacity at each sensor multiplied by the depth ranges in the 'Subsurface sensor depth ranges and material observations' section. We extrapolated the ET estimates from the hillslope profile for the entire area classified as 'Upland' and 'Shrubland', accounting for approximately 84% and 0.65% of the URW, respectively (Figure 8). We acknowledge that deeper-rooted shrubs likely accessed deeper sources of moisture beyond the 120 cm deep profile we measured. We likely underestimate ET beneath the small proportion of

the URW covered in shrubs. Extrapolated ET estimates were used in annual water balances for WY2019 and WY2020 in the URW. We relied upon the reported instrument error of +/- 3.00% for an uncalibrated Teros-12 sensor in a mineral soil system (Meter Group, Inc, 2019) to estimate error in ET measurements.

Groundwater monitoring wells

Seasonal groundwater dynamics in the URW were measured in two groundwater monitoring wells (Well 101 and Well 102, Figure 8). Wells were drilled in June 2019 using a three-phase 5.5 horsepower Delcrosa rotary drill with attachable 3.5 m pipe segments and a 65 mm diamond drill bit. Well installation was performed by Unu Kumachiq S.A.C., regional groundwater consulting experts based in Cusco. Well 101, located on the ridge divide between the Western and Central subbasins (Figure 8), was 21.3 m deep and groundwater was found at a depth of 20 m during drilling. The water table depth was below the depth of Well 101 for most of the water year and so Well 101 water table data were not used in our analyses. Well 102, located in *bofedal* A (Figure 8), was drilled to a depth of 11 m and was fully saturated at the time of well installation.

We cased both wells with slotted 65 mm diameter polyvinyl chloride (PVC) pipe with endcaps and installed HOBO U20-001 30-ft water level loggers to measure changes in water table depth at 15-minute intervals. When downloading well data we measured cable length of the securing vinyl-coated cable and took a manual water-depth measurement with a Solinist 101 water level meter.

Bofedal ET estimates. *Bofedales* cover 11.5% of the URW. We accounted for ET in bofedales with a temperature-driven daily model in the *Visualizing Ecosystems Land*

Management Assessment 2.0 (VELMA 2.0) user interface (Abdelnour et al., 2011) with a modified calculation from Hamon (1963) to estimate potential evapotranspiration (PET):

$$PET = K_{PET} \times L \times \rho_{vsat}(T_a)$$

$$with \begin{cases} \rho_{vsat}(T_a) = 0.622 \times \rho_a \times \left(\frac{e_{sat}(T_a)}{\rho_{SL}}\right) \\ e_{sat}(T_a) = 6.11 \times exp\left(\frac{17.3 \times T_a}{T_a + 273.3}\right) \end{cases}$$

where $\rho_{vsat}(T_a)$ is the air saturation absolute humidity (g/m^3) at the mean daily air temperature T_a (^{o}C) measured at the URW rain gage, ρ_a is an estimated air density at the mean elevation of the URW (770 g/m^3), $e_{sat}(T_a)$ is the saturation vapor pressure (kPa) at T_a, ρ_{SL} is the mean pressure at sea level (101.3 kPa), K_{PET} is a calibration constant, and L is the local day length expressed in hours (Dingman, 1994).

We assumed that for the time window in which the Well 102 water table was at the surface, all *bofedales* across the URW were saturated and water was evaporating off the surface as it would off an open body of water to satisfy PET demand. For time periods in which Well 102 was not full, we applied the ET estimates from the subsurface moisture sensor array to the area classified as 'Bofedal' (Figure 8). To account for error in PET estimates made from daily temperatures, we used the maximum error reported (+/- 30%) from a study that assessed temperature driven PET estimate error in the Ecuadorian páramo (Córdova et al., 2015).

Stream gage stations

To measure stream discharge in the URW, we installed two stream gaging stations in June 2018 (Figure 8, Figure 12). Each gaging station consisted of a 2 m long

by 38 mm diameter PVC staff gage that was secured to rebar stakes driven into the channel bed. A strip of tape with engineering feet measurements to the 1/50th-ft (~6 mm) was adhered to the outside of the staff gage for visual and independent recording of stage height during data downloads campaigns. A HOBO U20L-001 water level logger was secured within the PVC pipe by a vinyl-coated cable measuring approximately 2 m and tied to the PVC cap. Each HOBO U20L-001 water level logger was paired with an identical atmospheric pressure logger nearby to correct for barometric pressure using *HOBOware Pro Barometric Compensation data assistant*. We installed the Central stream gage (Figure 12) in the Central subbasin of the URW in a meandering reach of stream that drains an area of 0.806 km^2 (Figure 8). We installed the Above Diversion stream gage (Figure 12) downstream of the three-way confluence of the Eastern, Central, and Western subbasins, located just upstream of the concrete diversion weir and draining an area of 2.11 km^2 (Figure 8).

Figure 12. Left - the Above Diversion stream gage, and right - the Central stream gage. Both photographs are looking upstream. The grey PVC pipe is slotted, and a measuring tape adhered to the exterior to serve as a staff gage to determine water height for quality control and data correction of sensor depths to water level.

Streamflow. *Water level height.* We post-processed stream gage water level height with a correction by normalizing measured water level to the recorded stage height when data was downloaded. We corrected the sensor depths for each data series by a correction factor:

$$CF_{WL} = \frac{(H_{t1} - S_{t1}) + (H_{t2} - S_{t2})}{2}$$

Where CF_{WL} is the correction factor for water level recorded by the sensor, H_{t1} and H_{t2} are the stage heights recorded at the beginning and end of the time series, respectively, and S_{t1} and S_{t2} are the corresponding sensor depths. We applied the correction factor for each water level time series at the Above Diversion and Central stream gages and developed rating curves for each water year with salt dissolution discharge measurements to convert water level to discharge.

Salt dissolution discharge measurements. The URW hosts watercourses with small channels, steep channel gradients, and complex edge effects - rendering the watershed unsuitable for discharge measurements with traditional flow-meter equipment (Hudson and Fraser, 2005). Dry injection salt dissolution discharge measurements are conducted by inputting a known mass of salt upstream from an electrical conductivity logger and deriving discharge from the breakthrough concentration curve as the salt plug moves downstream (e.g., Hudson and Fraser, 2005). These methods proved appropriate and reliable for measuring surface water flow in the URW using the recommended protocol made by Hudson and Fraser (2005). We took discharge measurements using the salt dissolution technique at gaging stations and at additional locations up the Central and Eastern subbasins to characterize spatiotemporal variability in water yield. Channel morphology ranged from relatively shallow-sloped reaches (local channel slope < 5%) that ran through *bofedal* and grassland settings to steep reaches with bedrock-confined flow. In most locations, the channel was incised into either bedrock or into *bofedales*.

We programmed a HOBO Onset U24-001 electrical conductivity logger to record electrical conductivity at 1-second intervals and injected a known mass of dry salt upstream. We secured the electrical conductivity logger within a short, slotted 38 mm diameter PVC tube that was secured to the channel banks with a wooden stake. A typical trial was conducted uninterrupted for at least 10 minutes. We opted for a 10-minute minimum trial time as it substantially exceeded the necessary time for the dry injected salt tracer to pass discharge points when initially establishing URW salt dissolution protocol. We dry injected a pre-measured mass (between 50 g and 400 g, depending on the size and flow rate of the channel) of table salt from a sealed plastic bag a distance of at least 20 times the channel width upstream of the discharge point, typically 10 to 15 m upstream. We dry injected salt in a single motion, and the operator would stir the water where the salt was dry injected immediately following injection to ensure complete mixing. When a trial was concluded, the logger was removed, and the data uploaded and processed using *HOBOware Pro*.

To elucidate spatiotemporal patterns in URW runoff relative to *bofedal* land cover, we conducted additional field campaigns to systematically measure discharge in nested subbasins focused on the URW Central and Eastern subbasins (Figure 13) on 12 dates between June 2019 and January 2021 using salt dissolution streamflow gaging methods.

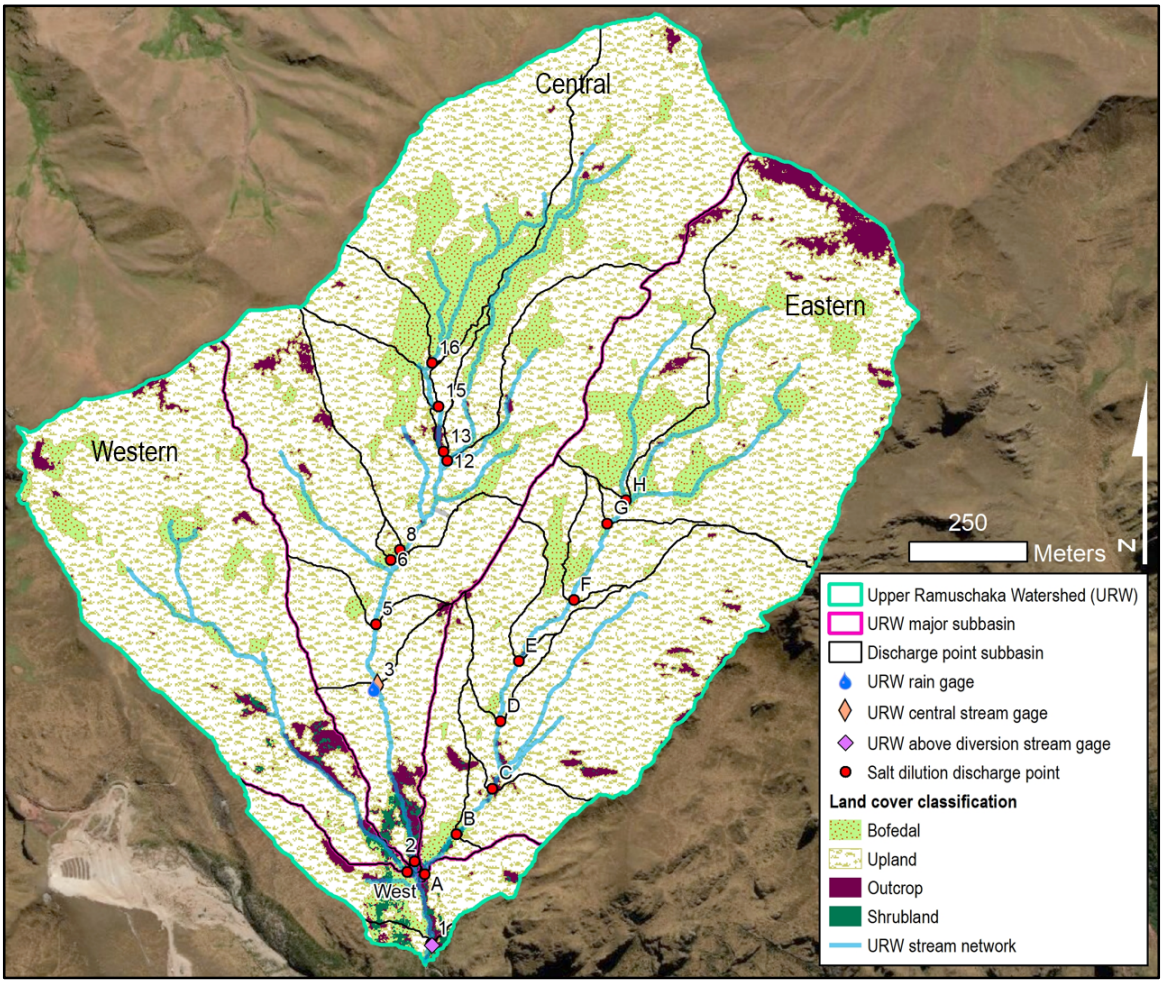

Figure 13. Salt dilution discharge campaign locations in nested subbasins of the URW. Numbers (Central subbasin) and letters (Eastern subbasin) show the locations of salt dilution discharge measurements taken on 12 dates from May 2019 – January 2021. Black boundaries delineate the subbasins draining to each point.

Salt dissolution discharge data processing. We post processed electrical conductivity data by reviewing conductivity breakthrough curves to ensure quality data collection. We removed any measurements with anomalous breakthrough curves from the data set. Once we confirmed data quality, we used the *HOBOware Pro Conductivity*

Assistant to convert electrical conductivity to specific conductance using the non-linear function, an electrical conductivity reading normalized to a temperature of 25^{o} C (Onset Computer Corporation, 2011), as recommended by Hudson and Fraser (2005). Once electrical conductivity data had been normalized to specific conductance, we converted specific conductance to salt concentration using the suggested correction factor of 0.486 (Hudson and Fraser, 2005). We then normalized concentration to the baseline concentration at the start of each trial in *Excel*, where we calculated discharge by dividing the known mass of dry injected salt by the area under the concentration curve (Hudson and Fraser, 2005).

In some cases, when discharge was low and an abundance of daily discharge measurements were made to compare with one-another, 10-minute electrical conductivity trials were inadequate to complete the entire measurement. We conducted individual quality control checks on all salt dissolution discharge measurement trials. In most cases, the missing tail of the terminated conductivity curve represented significantly less than 5% of the total salt mass measured (based on analysis from complete trial measurements). In cases where incomplete trial data were otherwise of good quality, we fit a power function to the decay tail of the curve in Excel for at least 10 mg/L of concentration decay curve points (e.g., from 20 mg/L to 10 mg/L) and projected the remainder of the trial to a concentration of 1 mg/L (Figure 14). Post-processing analyses showed that differences in calculated discharge between power-projected and measured curve tails on complete measurements did not exceed 5%. To maintain consistency across measurements, all post-processing extended to a 1 mg/L concentration threshold. There

were select cases when projecting a power curve trendline was inadequate to complete measurement trials. There were few of these cases (< 10), and they generally occurred when the projected power curve did not approach 1 mg/L in a comparable elapsed time to other measurements on the same date due to an unrealistically low decay exponent. We removed such trials from our analyses.

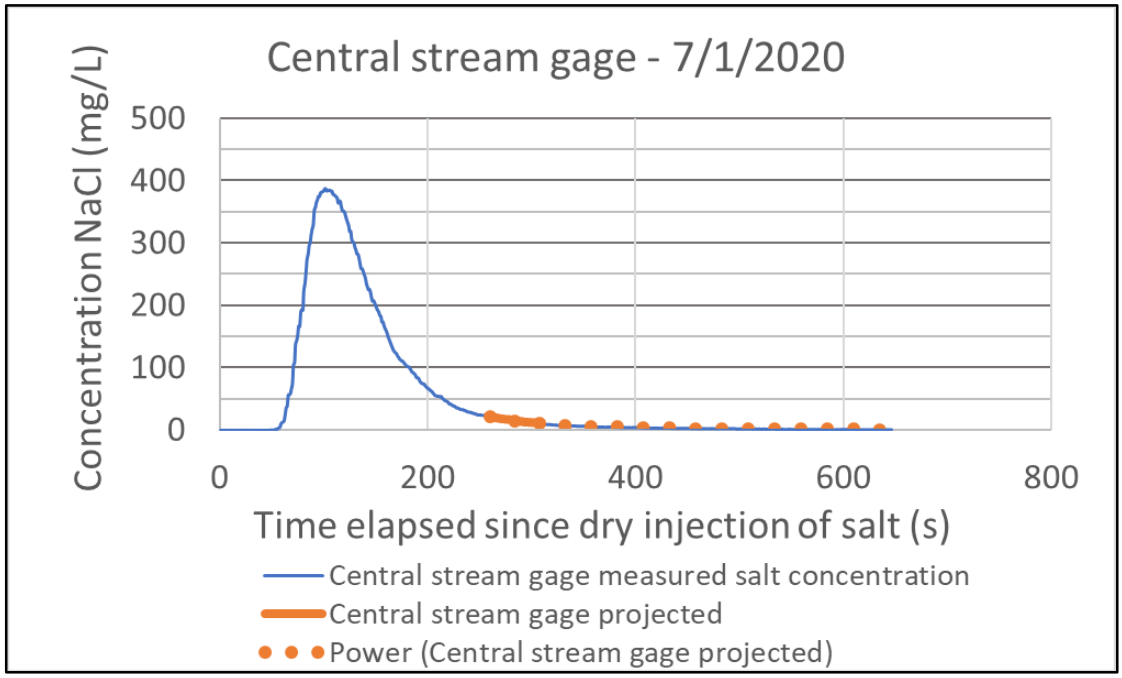

Figure 14. Demonstrative breakthrough salt dissolution trial is plotted adjacent to a power curve trendline fit to the salt concentration decay from 20 mg/L to 10 mg/L and projected forward to display the process of 'projecting' a prematurely terminated trial. The blue line tail shows the measured concentration of the complete trial to 1 mg/L, the solid orange line shows a power curve trendline and the dashed orange line shows the power curve function projected to 1 mg/L concentration. There was a 1.6% difference between measured and projected discharge at the Central stream gage on 7/1/2020, a difference of 0.09 L/s discharge.

Discharge rating curves. Rating curves (Appendix C) were developed from the initial corrected water level sensor reading of each data period and salt dissolution streamflow discharge measurements at the Central and Above Diversion stream gages. Each water year rating curve had two parts: a general rating curve that incorporated all discharge taken during the water year and fit with a second-degree polynomial function, and a low-end rating curve that was made from the lowest five or six discharge measurements taken and fit with a power curve function (Appendix C). Stream gage discharge estimates used the polynomial rating curve above the lowest intersection point between the polynomial function and the low-end power rating curves and used the low-end rating curve if below the lowest point of intersection between rating curves. We estimated potential error in rating curve predictions of discharge as:

$$Error = \frac{\left(\sum_{i=1}^{n} \left| \frac{Q_{observed} - Q_{predicted}}{Q_{observed}} \right| \right)}{n}$$

Where $Q_{observed}$ is the measured discharge from salt dissolution streamflow measurements, $Q_{predicted}$ is the predicted discharge from the observed stage height of the water year rating curve at the time the discharge measurement was taken, and n is the number of salt dissolution discharge measurements included in each water year rating curve.

Runoff and hydrographs. We scaled discharge to runoff in mm/day by dividing discharge by the subbasin area draining to the discharge measurement point. We made annual hyetographs and runoff hydrographs for the Central stream gage for WY2019 and for both the Central and Above Diversion stream gages for WY2020. We opted not to use

water level data from the Above Diversion stream gage for WY2019 because of a large debris flow event that occurred in March 2019 and notably altered the channel geometry, resulting in a poor rating curve at the Above Diversion stream gage. We calculated hydrograph runoff error estimates per rating curve, applied per water year to estimate potential runoff error at each stream gage.

Bofedal borehole surveys

We selected four *bofedales* in the upper URW to measure subsurface material properties via direct observations, laboratory tests, and via nuclear magnetic resonance (NMR) borehole logs. We conducted borehole surveys on five transects across four *bofedales* in the URW Central and Eastern subbasins, referred to as *bofedales* 'A', 'B', 'C', and 'D' (Figure 8, Figure 15). We strategically selected survey transect locations to capture a complete representation from *bofedal* centers to the transitions with the hillslopes draining into them. We used a telescoping hand auger with a Humboldt Mfg Co. 2.25 in (57.15 mm) diameter detachable auger bucket to create boreholes. We utilized telescoping auger quick attachments as needed to reach a maximum depth of 3.25 m, or to the depth of refusal, typically due to encountering saprolite or large rock chips. *Bofedal* surveys consisted of extracting material in approximately 20 cm depth increments and noting subsurface material properties, boundaries between subsurface materials and depth of the water table, if encountered.

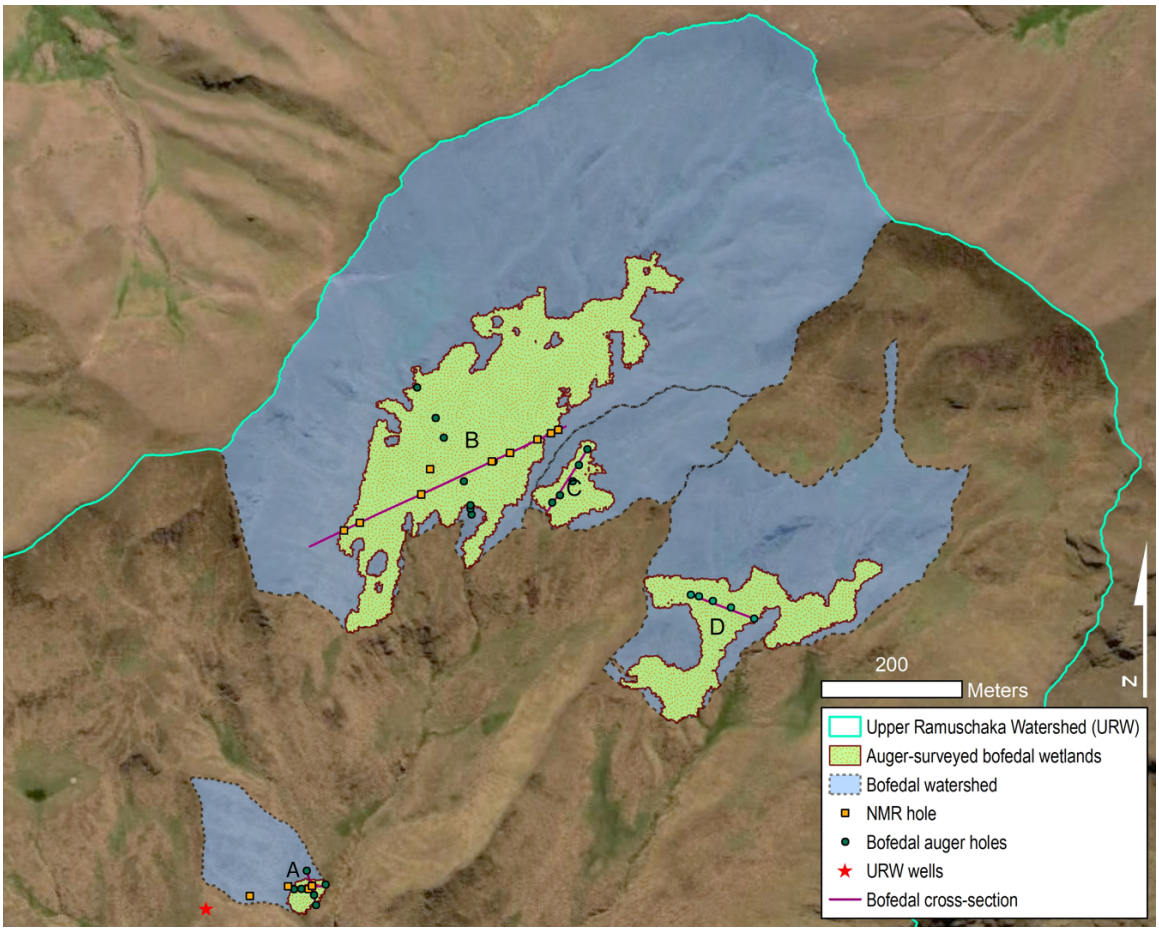

Figure 15. Locations of borehole surveys and NMR logs in four URW *bofedales* – labeled 'A', 'B', 'C', and 'D'. We determined the drainage area to each *bofedal* using a high-resolution 1-meter DEM and standard ArcMap 10.6 Hydrology tools. Purple lines in each of the four surveyed *bofedales* show the locations where cross-section analyses were made. Note that Well 102 in *bofedal* A (red star) is located at the intersection of the two *bofedal* A transects and is obscured by a yellow point as it was also surveyed with NMR.

Borehole NMR surveys

NMR borehole logging is a geophysical method that is used in near surface environments to determine the porosity or water content of sediments and to estimate pore-size distributions and hydraulic conductivity (Behroozmand et al., 2015). NMR

probes the nuclear spin of protons in hydrogen atoms placed in a static magnetic field and measures their response after being perturbed by a series of radio frequencies pulses. Borehole NMR measurements are commonly used to characterize water content and hydraulic conductivity of aquifers (Knight et al., 2012; Dlubac et al., 2013); have been heavily deployed in critical zone studies to determine the depth to the water table and porosity (Flichum et al., 2018, 2109); and more recently, have been used to determine the dynamic water storage in unsaturated fractured bedrock (Schmidt and Rempe, 2020). This study is the first to use borehole NMR to characterize hydrologic properties in peat.

We surveyed boreholes in June 2019 (Figure 15) with a portable NMR Logging System (Dart, Vista Clara, Inc., Mukilteo, Washington, USA). Measurements were collected downward from the ground surface elevation at 0.25 m increments. The volume of investigation of each measurement was a cylindrical shell of 0.23 m height, 1–2 mm thickness, and 6.5–7.6 cm radius, centered on the central axis of the tool (Walsh et al., 2013). NMR data were acquired using the Carr-Purcell-Meiboom-Gill pulse sequence at two operational frequencies (420 and 480 kHz). Two-sets of decays were collected using an approach similar to Heaton et al. (2000), both with an echo time of 0.4 ms. The first set used a short recovery time (0.1 s), which allowed a large number of averages (180 to 500 units) to be collected in a short measurement time and maximized the signal-to-noise ratio of the fast-decaying portion of the signal. The second set used a long recovery time (3 s with 30 to 40 units averages), which allowed the system to reach thermal equilibrium between pulses and yielded the slow-decaying portion of the signal.

Borehole NMR data NMR data were quality controlled and processed by Dr. Kristina Keating (Rutgers University, Earth and Environmental Sciences Department, Associate Professor) using *Javelin-Process_v4.4* commercial software. All stacks, stages, and frequencies associated with each depth interval were combined, and the resulting NMR decay curve was fit with a multiexponential decay function determined via a nonnegative least squares inversion algorithm with second-order Tikhonov regularization (Whittall et al., 1991). Water content estimated from our NMR measurements, θ_{nmr} (m^3/m^3), was taken as the value of the multiexponential decay curve fit at time equals zero. Saturated conductivity of subsurface materials (K_{sat}) was estimated using the Schlumberger Dole Research (SRD) equation, which is derived from the Kozeny-Carmen estimate of K_{sat} based on pore-geometry and has been shown to work well for unconsolidated sediments (Dunn et al., 2002; Dlubac et al., 2013).

Analyses and Calculations

Runoff and proportion of subbasin covered in *bofedales*

We used discharge measurements distributed throughout the URW to plot runoff (discharge scaled to subbasin area) from nested subbasins (Figure 13) against the percent of each subbasin classified as *'*Bofedal*'* to explore the relationship between streamflow and water yield from *bofedales*.

Watershed spatial runoff maps

To better understand relative hydrologic productivity within the URW, we made 'snapshot' runoff accounting maps for subbasin nested discharge measurements for four

dates in WY2020: December 2019, March 2020, July 2020, and August 2020. Spatial runoff maps were made by subtracting the measured discharge at a nested subbasin from the discharge measured downstream in the next greater subbasin (e.g., site 'A' – site 'B'), performing standard GIS functions to calculate the area between the two subbasin polygons, and converting to runoff by scaling the resulting discharge to the remaining polygon area in Esri *ArcMap 10.6 Desktop*.

Bofedal cross-section models

Seasonal dynamic storage is the seasonally saturated subsurface zone that fills and drains annually. We used a combination of borehole and NMR logs to construct *bofedal* cross-sections and estimate seasonal dynamic water storage in *bofedales* A, B, C and D (Figure 15). *Bofedal* borehole layers were categorized as either peat, clay, or an underlying mineral layer – generally either quaternary deposits or weathered bedrock. We assumed that the groundwater table in *bofedal* A (Well 102) was representative of *bofedales* throughout the URW; and that the dynamic storage capacity of *bofedales* extended beyond the peat and clay layers into the underlying mineral layer, as supported by field observations in multiple *bofedal* sites and Well 102 groundwater data. The water table was at the surface in *bofedales* A, B, C, and D in January 2020, which we assumed represented a 'full' state. The cross-sectional area between the January 2020 water table deepest measured water table depth in *bofedal* A (Well 102) represented the seasonal dynamic storage capacity for all URW *bofedal* cross-sections except for *bofedal* B. *Bofedal* B was the largest *bofedal* and found to have the deepest peat layer, thus the

seasonal dynamic storage zone was assumed to extend 1 m below the clay layer, corresponding with our observations of Well 102 groundwater logs.

Layer and water table depths were interpolated between boreholes. The water table depth was interpolated in *bofedales* A and B in June 2019, and in *bofedales* A, B, C and D in January 2020 (Figure 15). We included points where the water table was visible on the ground surface in the 8.3 cm/pixel orthomosaic image from June 2019 in the interpolation. Interpolations were implemented with inverse distance weighted (IDW) using between three and six points, depending on the transect and spatial resolution of boreholes. We used a power of two weighting to determine cell values. Points were generated every 1 m along *bofedal* transects in *bofedales* A, B, C and D in Esri *ArcMap10.6 Desktop*. We extracted ground surface elevation values from the 1-m/cell resolution DEM (Figure 9), and *bofedal* layer depths to transect points. Due to greater borehole NMR survey density in *bofedal* B, we also extracted NMR-derived porosity values of peat, clay, and the underlying mineral layer from NMR surveys in H7-H11 to *bofedal* B transect points. The transect points were imported to *Excel*, where we made cross-sections and estimated the dynamic storage in each *bofedal* transect.

Bofedal drainable dynamic storage estimates

We estimated the 'drainable' portion of seasonal dynamic storage that contributes to URW runoff to be the difference between saturation and field capacity water contents (e.g., Abdelnour et al., 2011). We refer to NMR measurements that considered only saturated media as porosity measurements and specify otherwise if NMR measurements from unsaturated media were used. We used the mean porosity values measured in each

of the three *bofedal* A layers to estimate dynamic storage in *bofedal* A. In *bofedal* B, we used the extracted IDW of mean layer porosity values per borehole due to greater borehole NMR survey density. For *bofedales* C and D, the borehole surveys were conducted in January 2020 (post NMR surveys), thus we used the mean layer porosity values from the complete NMR data set from June 2019. We estimated the field capacity by calculating the mean NMR water contents measured in each unsaturated layer. The field capacity value for peat was determined from the water content of unsaturated, superficial peat above the June 2019 water table, and the clay and underlying mineral layer field capacities were determined from unsaturated NMR layer measurements at the margin of *bofedal* B, in H5 and H6.

We made drainable dynamic storage estimates in *Excel* by calculating the difference between each layer porosity and field capacity water contents and multiplying it by the layer cross-sectional area below the January 2020 water table, mid wet season. In all *bofedal* cross-sections, we divided the sum of transect dynamic storage by the length of the transect to calculate an average cross-sectional dynamic storage depth. We report a range of drainable dynamic storage in each *bofedal* determined by the average storage value +/- NMR standard deviation of storage per layer. We extrapolated the range in seasonal dynamic storage capacity from the five *bofedal* cross-sections across URW land cover classified as 'Bofedal' to estimate a range of total drainable dynamic storage of *bofedales* in the URW. We then compared drainable dynamic storage estimates of *bofedal*es to runoff, with emphasis on the temporal phases that corresponded with the dry season and downstream water demand.

RESULTS

Water Yield in the Humid Puna

We took a water balance approach to quantify water yield from the URW. In the following sections, we present the data products associated with each component of the water balance and summarize values for WY2019 and WY2020.

Precipitation

In WY2019, the URW rain gage received 749 mm in WY2019, corresponding to an elevation-adjusted value of 792 mm for the Central stream gage subbasin (Appendix A). In WY2020, the URW rain gage received 825 mm, resulting in elevation-adjusted values of 867 mm in the Central stream gage subbasin and 859 mm in the Above Diversion stream gage subbasin. The methodology used for these calculations and associated maps can be found in Appendix A (Figure 36, Figure 37).

Dry and wet seasons

The dry season, defined as the time window when 15-day cumulative precipitation at the URW rain gage was less than 10 mm, spanned May 7th, 2019 to October 15th in 2019, and May 19th to October 18th in 2020. The WY2019 wet season spanned from September 14th, 2018 to May 6th, 2019, and the WY2020 wet season spanned from October 16th, 2019 to May 7th, 2020. Dry and wet season precipitation

totals are presented in annual water balances and shown as highlighted time windows in monitoring instrument data products.

Evapotranspiration

Subsurface moisture sensor array and upland ET estimates

ET was estimated from seasonal dynamics in subsurface moisture content (Figure 16). Sensors at 20 and 60 cm were in soil horizons A and B, respectively, the sensor at 90 cm was in the transition between soil and saprolite (B/C horizon), and the 120 cm sensor was in saprolite. Dashed horizontal lines show field capacity estimates at each depth (Appendix B). The initial fill-up, saturation, and recession responses of Well 102, in *bofedal* A, are plotted for reference (Figure 11Figure 16).

In the wet season, subsurface moisture contents rose to quasi-steady state upper VWC values, from which we defined field capacity, and declined steadily over the dry season. In WY2020, subsurface moisture contents reached field capacity between November 2019 and January 2020. Field capacity was reached in the two intermediate sensors (60 cm and 90 cm) before Well 102 saturated (Figure 16), while the deepest sensor (120 cm) reached field capacity shortly after Well 102 saturated. The shallowest sensor (20 cm) did not reach field capacity until January, suggesting that large amounts of moisture are delivered to depth via preferential flow pathways while the shallow subsurface is still wetting up. For each depth, we report field capacity, minimum and maximum VWC, and annual ET estimates (in mm) (Table 2).

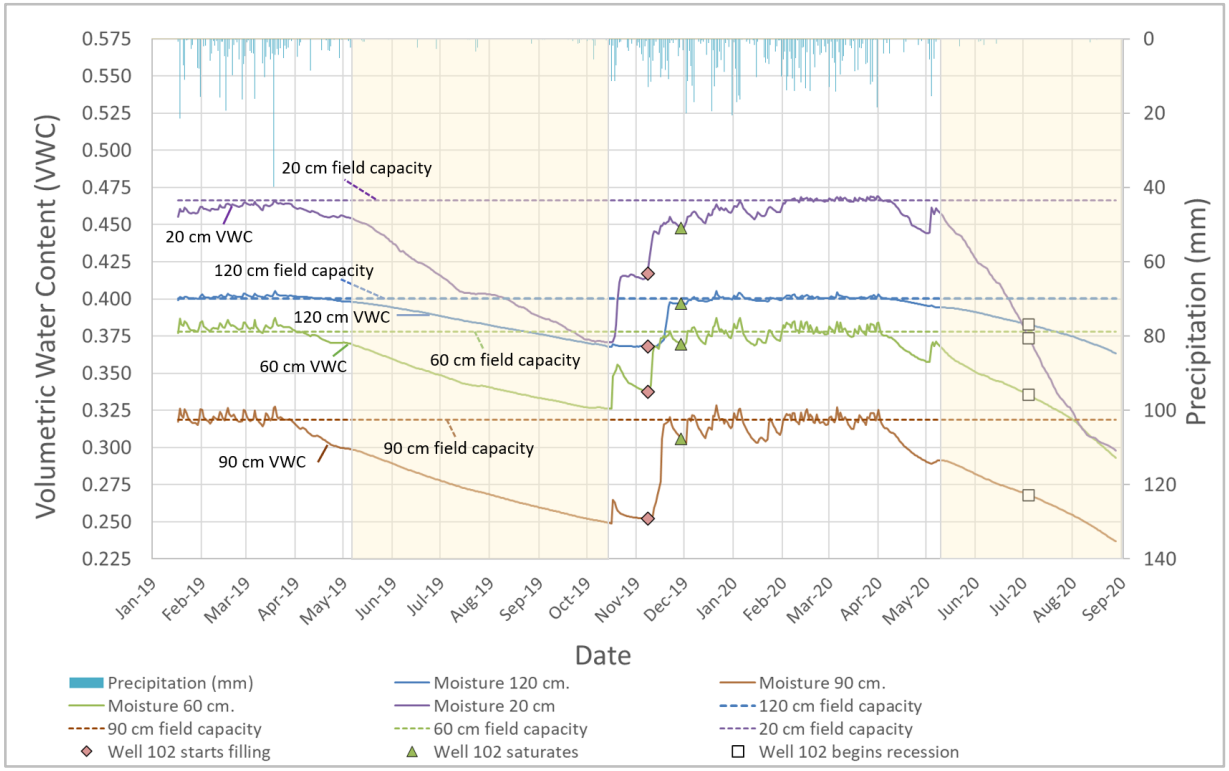

Figure 16. Volumetric water content (VWC) for all depths from January 17, 2019 – August 31, 2020. VWC was measured with four Teros-12 subsurface sensors (Meter Group LLC, 2019) installed at 20 cm, 60 cm, 90 cm, and 120 cm depths in a vertical profile of undisturbed material beneath upland puna grasses (see Figure 8 map for location and Appendix B for schematic diagram). Precipitation, in mm/day is shown above and plotted against the flipped y-axis to the right. Yellow-shaded time periods correspond with the dry season. The orange diamond shows when Well 102 (in *bofedal* A) began to fill up, the green triangle shows the time at which the water table in Well 102 (in *bofedal* A) reached the surface, and white square shows the time when the water level in Well 102 began to recede. See Appendix B for subsurface material descriptions and horizon designations

Table 2. Subsurface moisture monitoring and ET estimation results from the subsurface moisture sensor array. Note that estimates of ET in WY2019 are incomplete because the sensors were installed on January 17th, 2019, months after the start of WY2019.

Sensor depth (cm)	**Minimum VWC**	**Maximum VWC**	**Field Capacity**	**WY2019 ET (mm)**	**WY2020 ET (mm)**
20	0.295	0.469	0.466	43	106
60	0.290	0.387	0.378	17	62
90	0.234	0.328	0.319	21	55
120	0.362	0.405	0.400	7	17

ET estimates for WY2019 are from the portion of the water year during which the subsurface moisture sensor array was installed (January 17th, 2019 to August 31st, 2019, Table 2); WY2020 ET estimates were calculated for the entire water year (September 1st, 2019 to August 31st, 2020, Table 2). The three shallowest sensors – at 20, 60 and 90 cm – show a decline to substantially lower VWC in WY2020 than in WY2019 (Figure 16, Table 2); likely due to a light-severity grassland fire that burnt through the hillslope where the subsurface moisture array was installed. We observed vigorous regrowth of *J. ichu* grasses and other vegetation in January 2020. The increase in growth was likely accommodated by greater uptake of shallow subsurface moisture and resulted in greater ET. The minimum VWC at a depth of 120 cm was similar in the dry seasons of WY2019 and WY2020, suggesting limited access of roots at this depth, which was consistent with our observations of rooting depth along roadcuts.

Groundwater monitoring well 102 and *bofedal* ET estimates

Groundwater in Well 102 rose to the surface of *bofedal* A in the wet season, and only began to drain well into the dry season (Figure 17). We measured two remarkably similar annual cycles of recession, recharge, and sustained wet season saturation in the Well 102 groundwater table between July 2019 and January 2021. From the installation of Well 102 in early July 2019 until November, the groundwater table fell at a constant rate of 15.2 mm/day and reached a maximum depth of 1.77 m. On November 29th, 2019, after 173.8 mm of cumulative precipitation in WY2020, the groundwater table reached the surface of *bofedal* A. The groundwater table remained at the surface until July 4th, 2020, at which point *bofedal* A began to drain and the groundwater table fell at a constant rate of 13.4 mm/day and reached a maximum depth of 1.94 m. On December 9th, 2020 after 181.5 mm of cumulative precipitation in WY2021, the groundwater table returned to the surface. In each dry season, the groundwater table fell more than 1 m into the clay and mineral layers underlying the superficial peat layer (the depth of peat was 0.6 m).

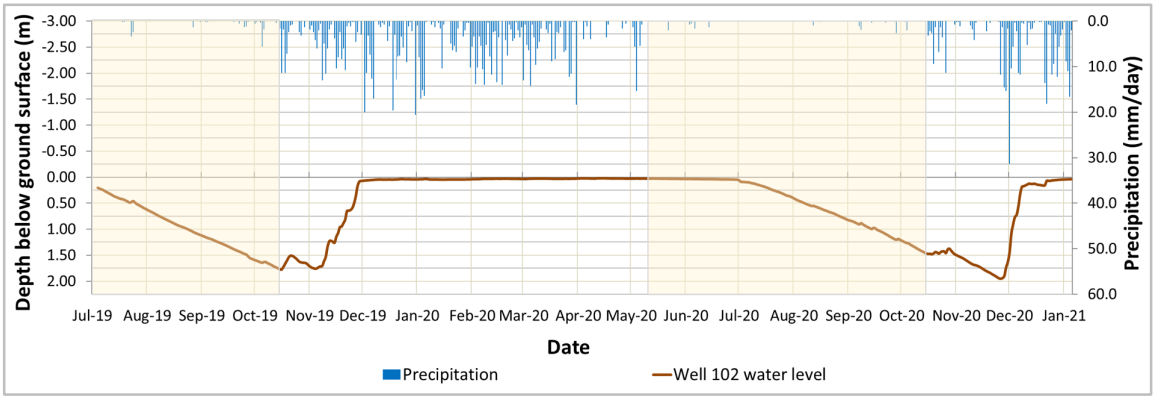

Figure 17. Water level in Well 102, located within *bofedal* A in the Central URW subbasin from July 2019 to January 5, 2021. Dry seasons are shown with the yellow highlighted time periods. The water table in Well 102 was at the ground surface from November 29th, 2019 to June 29th, 2020. The groundwater table did not begin to fall until 45 days into the 2020 dry season.

Cumulative ET estimates in the URW

We combined estimates of ET from the hillslopes – via soil and saprolite moisture dynamics – and estimates of ET from bofedales – using the modified Hamon (1963) equation for PET, to estimate cumulative ET in the URW (Figure 18). The time over which we summed ET on hillslopes with ET from *bofedales* is represented with the dashed orange line and corresponded to when *bofedal* A was saturated (Figure 17).

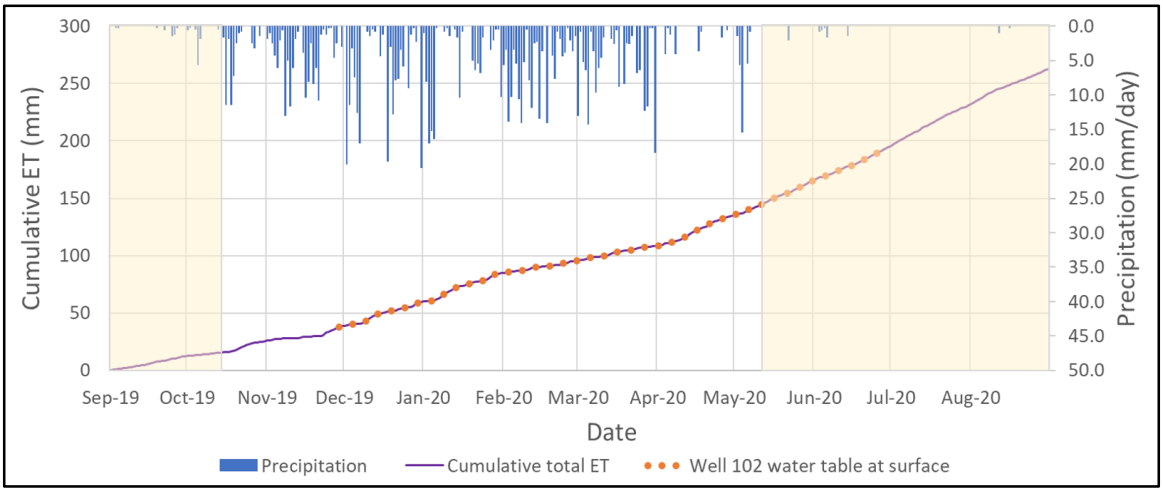

Figure 18. Hyetograph and cumulative ET estimates from the URW Central stream gage subbasin. The dry season is shown with the yellow highlighted time periods. ET estimates were made from measured VWC moisture loss from the subsurface moisture sensor array plus modeled estimates of potential evapotranspiration (PET) from saturated *bofedales*. PET estimates were made from a modified version of Hamon (1963) temperature-based numerical model (orange dashed line) for the period when the Well 102 water table, in *bofedal* A, was at the surface. For periods over which this was not the case, we applied the modeled hillslope ET to *bofedal* cover area (solid purple lines).

ET in the URW underwent various rate changes in the first half of WY2020 until approximately April 2020, indicated by increases and decreases in the slope of cumulative ET (Figure 18). The ET rate was steady from April 2020 until the end of WY2020, in August 2020. The sustained steeper slope of cumulative ET in the WY2020 dry season following the wet season suggests that there were adequate subsurface moisture stores in the hillslope to meet atmospheric demand despite the lack of precipitation during the dry season. One outlier period is the window from February 2020 until April 2020 when there was a shallower slope of cumulative ET estimates despite an

abundance of austral summer precipitation. The shallower-sloped period may be due to underestimation of ET from the subsurface moisture monitoring array in the hillslope (Figure 18) during the wet season, as the conditional structure of estimating ET from daily VWC values below field capacity did not account for ET during periods of continuous or intense precipitation during the wet season. Uncertainty from our ET estimates relied upon the reported error of 3.00% from VWC moisture sensors and assumed stable function and performance of the moisture sensor array. To account for uncertainty in estimates of *bofedal* ET from temperature-modeled PET, we applied the maximum error reported for similar methods by Córdova et al (2015).

Runoff

Hydrographs and hyetographs show the dynamics of URW precipitation inputs and seasonal runoff at the Central and Above Diversion stream gages (Figure 19, Figure 20). Diamonds represent the dates when discharge was measured via salt dissolution to build rating curves (Appendix C), and the dry season is demarcated by the yellow highlighted time windows. Runoff from each subbasin is a function of daily discharge divided by the subbasin area draining to each gage (0.806 km^2 for the Central stream gage, and 2.11 km^2 for the Above Diversion stream gage). Hydrographs and hyetographs span WY2019 and WY2020 at the Central stream gage (Figure 19) and WY2020 at both the Central and Above Diversion stream gages (Figure 20).

Runoff at the Central stream gage showed small responses to precipitation at the beginning of the wet up of WY 2019 (Figure 19). However, low flow conditions

extended until late December 2018. In late December, after 280 mm of cumulative precipitation, runoff rose sharply and remained high (above ~ 1.8 mm/day) through the remainder of the wet season. Storms caused a series of runoff peaks, most notably the March 18th event, which produced landslides downstream. Beginning in April 2019, runoff declined steadily throughout the dry season to a baseflow of 0.22 mm/d, or 2.05 L/s. WY2020 showed a similar transition from dry to wet season, however the sustained increase in wet season runoff occurred in early December after 178 mm of cumulative precipitation. Again, runoff responded rapidly to precipitation throughout the remainder of the wet season. The dry season recession began later, between late April and early May 2020, due to several storms in early May. The WY2020 dry season showed a similar slow recession of runoff with baseflows sustained above 0.21 mm/day, or 1.96 L/s.

Runoff at the Above Diversion gage in WY2020 showed similarities to the Central stream gage throughout the wet season (Figure 20). In the dry season, however, runoff at the Above Diversion stream gage sustained substantially greater baseflow (~0.45 mm/d, or 11 L/s) suggesting large inputs of water to the stream between the two stations.

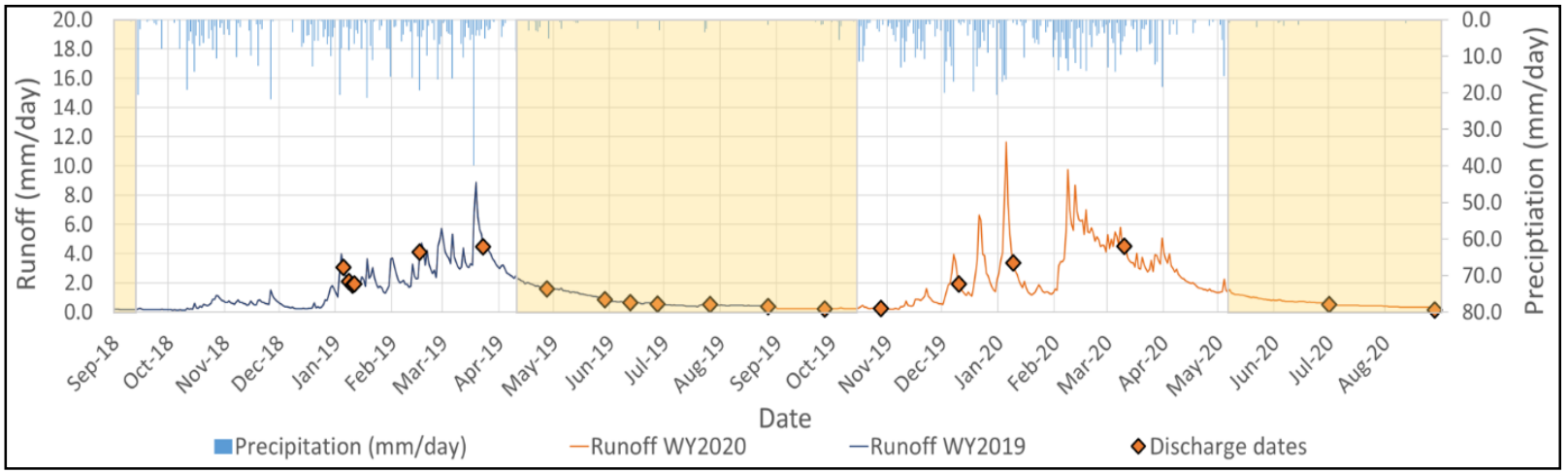

Figure 19: Hyetographs and hydrograph of the Central stream gage for water years 2019 and 2020. Dry season flows for the two water years were defined by the period over which 15-day cumulative antecedent precipitation is less than 10 mm and shaded orange. The dry season corresponds to when downstream irrigation water demand is the greatest. Orange diamonds indicate the dates on which salt dissolution discharge measurements were taken to construct the rating curve for each water year (Appendix C). The hydrograph y-axis is shown in runoff (mm/day), or discharge scaled by the total watershed drainage area (0.806 km^2).

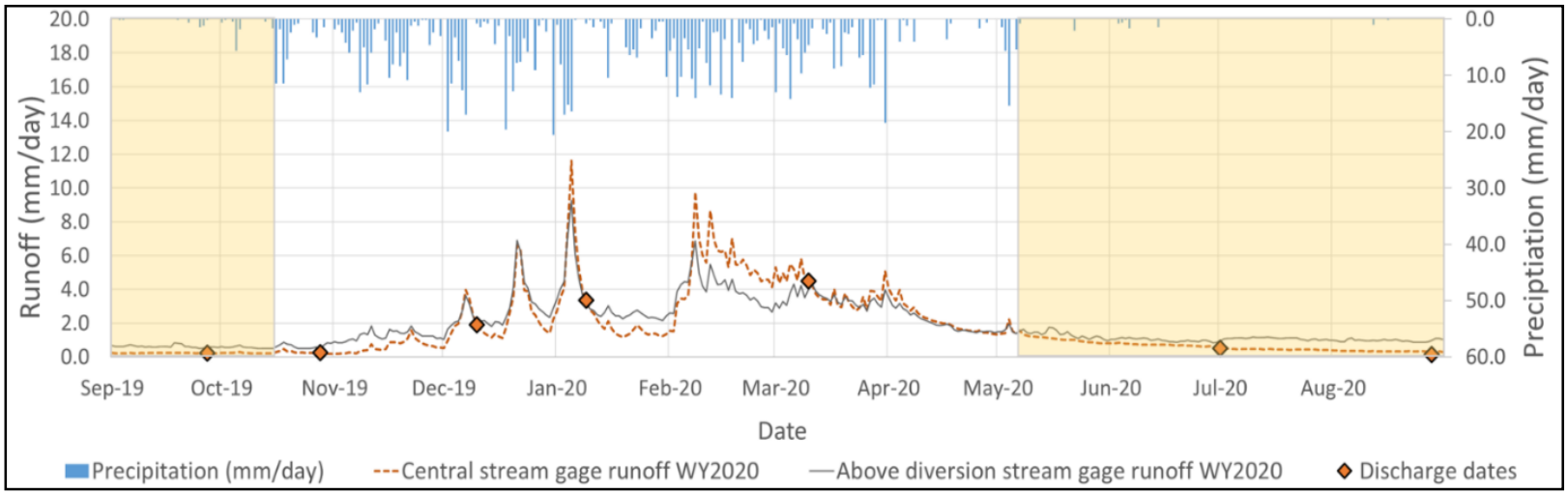

Figure 20: Hyetograph and hydrograph of runoff at Above Diversion stream gage (area: 2.11 km^2, solid blue line) plotted alongside the Central stream gage (area: 0.806 km^2, dashed orange line) for WY2020. Dry season flows for WY2020 were defined by the period over which 15-day cumulative antecedent precipitation was less than 10 mm and are noted by the orange shaded sections. Orange diamonds indicate the dates on which salt dissolution discharge measurements were taken to construct the rating curve. The hydrograph y-axis is shown in runoff (mm/day), or discharge scaled by the total watershed drainage area.

Water Balances

We combined water inputs (precipitation) and outputs (runoff, ET, and ΔS - the difference between water balance inputs and outputs) to construct annual water balances for WY2019 and WY2020 (Table 3). We report annual values as well as values for the wet and dry seasons only.

Table 3A shows the WY2019 annual water balance for the subbasin draining to the Central stream gage (Figure 8). The URW rain gage received 749 mm of precipitation in WY2019, resulting in an elevation-adjusted precipitation value of 792 mm for the mean elevation of the Central stream gage subbasin (Appendix A), 17 mm of which fell during the dry season. The URW Central stream gage measured 489 mm of annual runoff, 75 mm of which (15%) occurred during the dry season. Runoff in WY2019 accounted for 62% of precipitation in the Central subbasin watershed. Corresponding total discharge volumes by wet and dry season are shown in Table 3A. The WY2019 water balance for the URW Central stream gage (Table 3A) underestimated ET due to the installation of the subsurface moisture monitoring array in January 2019, over three months past the start of WY2019. Additionally, the reliability of the first several months of subsurface moisture data was likely of lower quality due to disturbance in the subsurface moisture profile from the borehole installation process. While the WY2019 water balance was short of being closed due to the ET data gap, seasonal estimates of runoff and precipitation are useful for comparison to WY2020 water balances. ET totals

in WY2020 suggest most of the 181 mm of unaccounted for moisture in the WY2019 water balance was likely unmeasured ET.

Table 3B shows the WY2020 annual water balance for the subbasin draining to the Central stream gage subbasin (Figure 8). The URW rain gage received 825 mm of precipitation in WY2020, resulting in an elevation-adjusted value of 867 mm of precipitation for the mean elevation of the URW Central stream gage subbasin (Appendix A). The Central stream gage measured 614 mm of runoff (71% of precipitation), 65 mm of which (11%) occurred during the dry season. Corresponding discharge volumes by wet and dry season are shown in Table 3B. ET estimates for the Central stream gage subbasin were 263 mm, which accounted for 30% of the annual water balance. The WY2020 Central stream gage subbasin (Table 3B) was the nearest to closing the annual water balance with a ΔS of 1% (i.e., runoff and ET estimates accounted for 101% of the elevation-adjusted annual precipitation), which is well within our estimated error.

Table 3C shows the WY2020 annual water balance for the subbasin draining to the Above Diversion stream gage (Figure 8). The 825 mm of precipitation received at the URW rain gage in WY2020 resulted in an elevation-adjusted value of 859 mm of precipitation. This value is less than the elevation-adjusted annual precipitation in the Central subbasin watershed due to the slightly lower mean elevation of the Above Diversion stream gage subbasin (Appendix A). The Above Diversion stream gage measured 685 mm of runoff (80% of precipitation), 130 mm of which (19%) occurred during the dry season. Corresponding total runoff volumes by wet and dry season are presented in Table 3C. ET estimates for the Above Diversion stream gage subbasin were

262 mm, accounting for 31% of the annual water balance. The ΔS of the WY2020 Above Diversion stream gage water balance was -8%. While not closed, the WY2020 Above Diversion stream gage watershed (Table 3C) provides useful annual and seasonal water yield data that can guide water resources management in Zurite.

Table 3: Annual water balances for the Central stream gage subbasin for WY2019 and WY2020, and for the Above Diversion stream gage subbasin for WY2020. WY2019 was not included for the above diversion site due to alterations in stream channel geometry at the Above Diversion stream gage site from landslides in March 2019. Precipitation values received in each water balance represents the measured precipitation value at the URW rain gage adjusted for orographic effects on precipitation (See Appendix A for methodology).

Site		**Precipitation**		**Runoff**				**Estimated ET**	**ΔS**
		Wet season (mm)	***Dry season (mm)***	***Wet season (mm)***	***Dry season (mm)***	***Wet season (m^3)***	***Dry season (m^3)***		
***A)* Central stream gage WY2019**	**Total**	775	17	415	75	334,101	60,320	122 ± 14	181
		792 ± 8		489 ± 59		394,420 ± 50,000			
	Percentage	100		62 ± 12				15 ± 11	23
***B)* Central stream gage WY2020**	**Total**	847	20	549	65	442,198	52,384	263 ± 22	-10
		867 ± 4		614 ± 63		494,580 ± 51,500			
	Percentage	100		71 ± 10				30 ± 8	-1
***C)* Above Diversion stream gage WY2020**	**Total**	840	19	554	130	1,171,060	275,130	262 ± 19	-70
		859 ± 4		685 ± 98		1,446,190 ± 104,500			
	Percentage	100		80 ± 14				31 ± 7	-8

Temporal Phases of the Annual Water Balance

While the three annual water balances were comparable, differences in runoff values between water years and stream gages led to further inquiry regarding temporal and spatial dynamics of runoff within the URW. The Central stream gage WY2020 cumulative daily water balance plot (Figure 21) presents a three-phase temporal framework to consider distinct windows of the water year. The three-phase plot of WY2020 includes ‘Fill-up’, ‘Steady-state’ and ‘Release’ phases (Figure 21, Table 4).

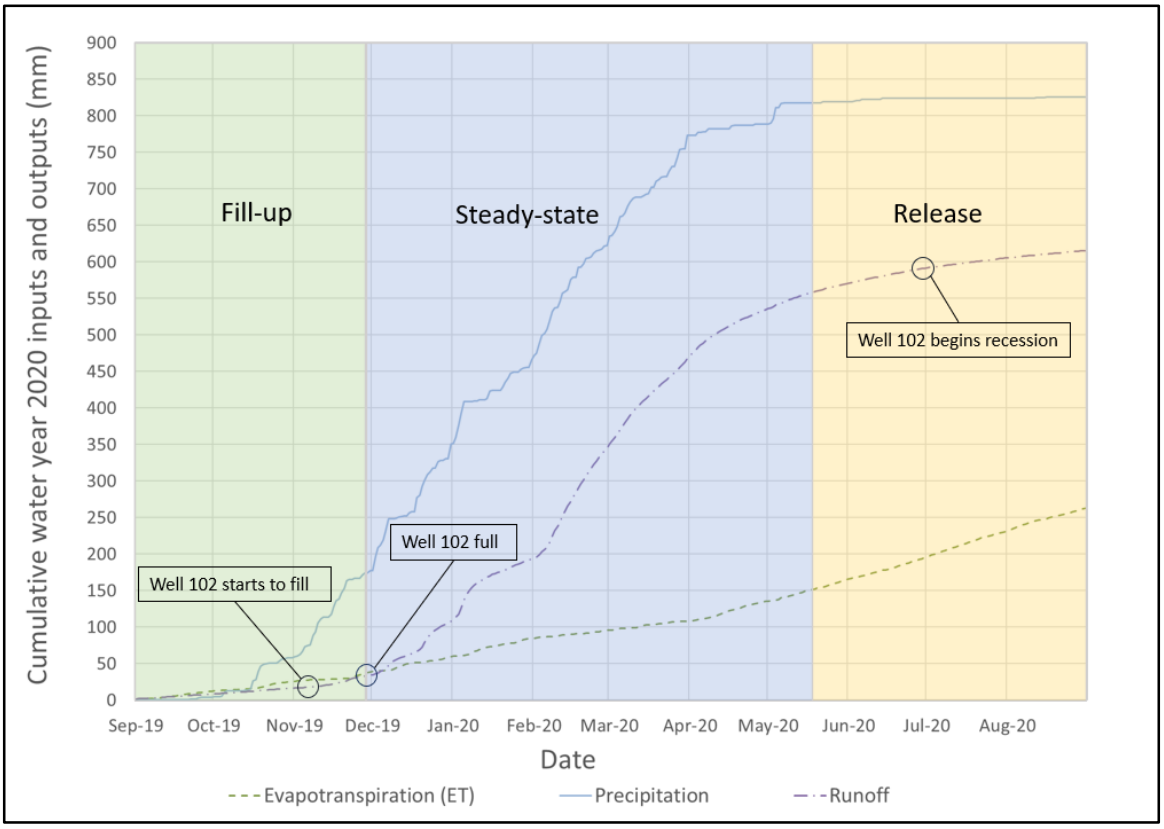

Figure 21. The flux of moisture through the URW can be assigned to three different phases for WY2020. Early in the 'Fill-up' phase, ET exceeded runoff. Precipitation inputs primarily went into storage – replenishing a moisture deficit – and little response was observed in streamflow. Once dynamic subsurface moisture is filled (indicated by Well 102 filling up after approximately 174 mm of precipitation input) cumulative runoff closely tracks cumulative precipitation and the system is at quasi 'Steady-state.' As the URW enters the dry season and cumulative precipitation levels off, the system enters a 'Release' phase. Cumulative runoff also begins to level off as moisture is drained from hillslopes and *bofedales* (Well 102).

The Fill-up phase begins on September 1st with the new water year and spans the period over which initial precipitation inputs recharge moisture deficits in the subsurface. During the WY2020 Fill-up phase, precipitation, which was approximately four to five

times greater than ET and runoff, and primarily recharged URW water storage pools that were depleted throughout the dry season. Soil and saprolite moisture showed steady increases and Well 102 began to recharge, but streamflow showed only very modest responses (Figure 21, Table 4).

The Steady-state phase began when soil moisture reached field capacity and the groundwater table in Well 102 reached the surface of *bofedal* A. Once field capacity was reached on the hillslopes and *bofedal* A saturated, the watershed entered a quasi-steady state in which precipitation inputs were roughly equal to the combined outputs of runoff and ET. During the Steady-state phase, cumulative ET increased steadily due to increased temperature and moisture content during the austral summer. The absolute values of ET however, remained approximately 20% of both runoff and precipitation totals.

The Release phase began on May 19th, 2020, when 15-day antecedent precipitation fell below 10 mm. With precipitation inputs nearly absent (Table 4), runoff rates declined - indicated by a decrease in the slope of cumulative runoff (Figure 21). Importantly, streamflow continued, albeit at decreasing values, and cumulative runoff continued to increase through the dry season. Baseflow remained above 1.96 L/s at the Central stream gage and above 11 L/s at the Above Diversion stream gage. ET accounted for the greatest total moisture loss over the Release period as upland grasses and hydrophytic vegetation took up moisture, leading to depletion in subsurface moisture content that would be recharged during the Fill-up phase of the following water year.

Table 4. Cumulative and daily rates of precipitation, runoff, and evaporation for the three phases of Fill-up, Steady State and Release over WY2020.

Water year phase	**Fill-up**	**Steady State**	**Release**
Date range	9/1/2019 - 11/29/2019	11/30/2019 – 5/18/2020	5/19/2020 - 8/31/2020
Precipitation total (mm)	173.8	643.6	7.8
Precipitation daily rate (mm/day)	1.93	3.76	0.07
Runoff total (mm)	32.4	524.4	57.3
Runoff daily rate (mm/day)	0.36	3.07	0.55
ET total (mm)	37.6	114.1	111.1
ET daily rate (mm/day)	0.42	0.67	1.06

Linking Water Supply to Zurite Agricultural Water Demand

Figure 22 compares monthly water yield from the URW to typical monthly irrigation needs across the 181 ha of Zurite agricultural fields with infrastructure to irrigate using URW derived water (Figure 4). The five major crop classes considered for irrigation demand were feed crops, fava beans, corn, quinoa/onions/carrots (combined due to overlapping growing season and water needs), and potatoes. The total irrigation demand of each crop is summed on the y-axis. To estimate the volume of irrigation water demand for a crop in a month, the crop type and corresponding irrigation demand in mm can be multiplied by the total area of cultivation to determine a volumetric irrigation demand. The total approximate irrigation water demand of a typical annual planting regime (Table 1) per month is the total depth value of each month's stacked crop unit water demand columns, multiplied by 181 ha. The combined water supply of mean monthly precipitation and URW water yield can meet all or most of the monthly water demand between October and April, with the greatest impact from URW derived water in April, May, October, and November. The combined water supply from monthly precipitation and URW water yield, however, falls significantly short of the water demand from May until September. Crop irrigation demand exceeds the combined water supply by 830 mm over the same period, a deficit that is pronounced by the absence of long-term surface water storage in Zurite.

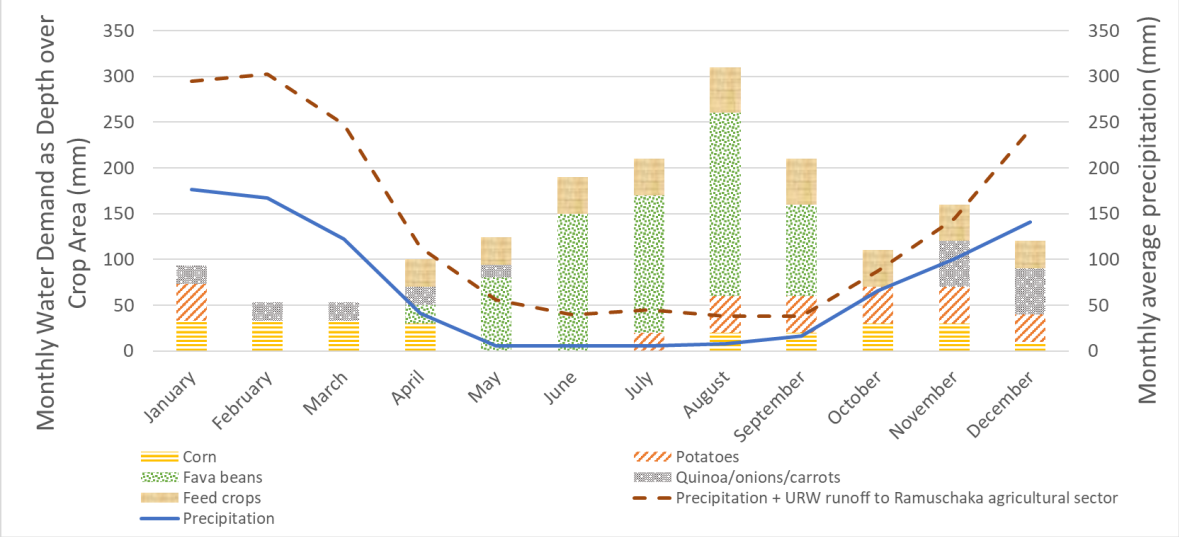

Figure 22. Average monthly water supply plotted with monthly precipitation and irrigation water demand in Zurite. The solid blue line is historic mean monthly precipitation. The dashed brown line shows monthly precipitation in addition to URW (Above Diversion stream gage) runoff distributed across the agricultural sector with existing infrastructure to distribute water from the URW, an area measuring approximately 181 hectares (Figure 4).

Spatiotemporal Patterns of Water Yield in the URW

In this section, we present the results of our spatially distributed discharge measurements conducted in nested subbasins throughout the URW (Figure 13); first relating runoff to the spatial distribution of bofedales, and then comparing WY2020 spatiotemporal snapshots of hydrologic productivity throughout the URW.

Links between *bofedales* and runoff

Spatially distributed discharge measurements in nested subbasins measured spatiotemporal dynamics of runoff throughout the URW. Subbasin drainage areas, the

areas and corresponding percentages of the total subbasin areas classified as 'Bofedal', and the mean slopes of subbasins are shown in Table 5. Table 6 presents the 12 discharge dates from June 2019 to January 2021 and corresponding flow percentiles at the Central stream gage, calculated from September 1st, 2018 – January 5th, 2021. Discharge measurements were located within the Central (n = 9), Eastern (n = 8), and Western (n = 1) subbasins, nested within site '1' (the Above Diversion stream gage subbasin) (Figure 13, Table 5). The 'West' discharge point (Figure 13) measured discharge from the Western subbasin - which we treated differently due to the widespread extent of karst limestone weathering found exclusively in the Western subbasin headwaters.

Table 5. Total subbasin drainage area, drainage area classified as *bofedal*, percent *bofedal* cover and mean subbasin slope for all discharge measurement points throughout the Central and Eastern catchments. We delineated all subbasin areas using standard GIS protocols on a 1-m resolution DEM. All subbasins are nested within the greater URW, Site 1.

Subbasin	**Site**	**Drainage area (km^2)**	**Subbasin area classified as *bofedal* (km^2)**	**Subbasin area classified as *bofedal* (%)**	**Mean subbasin slope (degrees)**
Central	1 – Above Diversion stream gage	2.112	0.244	11.53	23.91

Subbasin	Site	Drainage area (km^2)	Subbasin area classified as *bofedal* (km^2)	Subbasin area classified as *bofedal* (%)	Mean subbasin slope (degrees)
	2	0.873	0.127	14.51	23.17
	3 – Central stream gage	0.806	0.126	15.59	22.53
	5	0.756	0.124	16.43	22.05
	6	0.600	0.118	19.73	20.96
	8	0.597	0.118	19.71	20.93
	12	0.198	0.0312	15.75	20.29
	13	0.219	0.0617	28.21	20.48
	15	0.209	0.0594	28.41	20.65
	16	0.172	0.0506	29.42	19.04
Eastern	A	0.797	0.0801	10.05	23.98
	B	0.754	0.0761	10.09	23.90
	C	0.725	0.0755	10.41	23.62
	D	0.521	0.0750	14.40	21.84
	E	0.477	0.0738	15.48	21.42

Subbasin	Site	Drainage area (km^2)	Subbasin area classified as *bofedal* (km^2)	Subbasin area classified as *bofedal* (%)	Mean subbasin slope (degrees)
	F	0.443	0.0672	15.17	21.47
	G	0.408	0.0632	15.50	21.61
	H	0.096	0.0239	24.84	17.45
Western	West	0.373	0.0288	7.71	24.74

Table 6. Discharge dates and corresponding flow percentiles calculated from the Central stream gage for water years 2019 and 2020. Light blue filled cells are dates for which "hydrologic productivity" maps were made in Figure 24 and Figure 25.

Date	Flow percentile
6/12/2019	49.0
6/27/2019	44.4
7/26/2019	42.3
8/27/2019	29.6
9/27/2019	8.9
10/28/2019	14.3
12/10/2019	76.3
1/9/2020	88.5
3/10/2020	94.4
7/1/2020	42.8
8/28/2020	1.4
1/5/2021	88.8

Figure 23 shows the relationship between the percent of each subbasin classified as *bofedal* (x-axis) and runoff (y-axis, log scale). The measurements from each subbasin are distinguished by the shape of symbols. The color of each symbol corresponds to flow conditions via the flow percentile on the respective discharge date (Table 6). Runoff declined steadily through the dry season at all sites. There is strong a correspondence between the percent of subbasin classified as *bofedal* in the Central and Eastern subbasins

and runoff across all seasons. This relationship is stronger in the dry season. Generalized linear model analyses of all Central and Eastern runoff values in March 2020 and August 2020 (maximum and minimum flow percentile dates, respectively) showed different types of best fit trendlines in the highest and lowest flow percentile dates, where $y = 0.2135x - 0.0338$ ($r^2 = 0.62$) in the wet season and $y = 0.0076x^{1.29}$ ($r^2 = 0.40$) in the dry season. Trendline fits greatly improved on both dates if discharge sites '1' (Above Diversion stream gage), '2' (measuring the Central subbasin at the confluence of the three main subbasins) (March 2020 and August 2020 $r^2 = 0.73$ and 0.79, respectively), suggesting distinct hydrologic conditions in the lower subbasin compared to all other upland sites. The start of the dry season corresponds with the 68.3 flow percentile in WY2019 and the 59.2 percentile in WY2020.

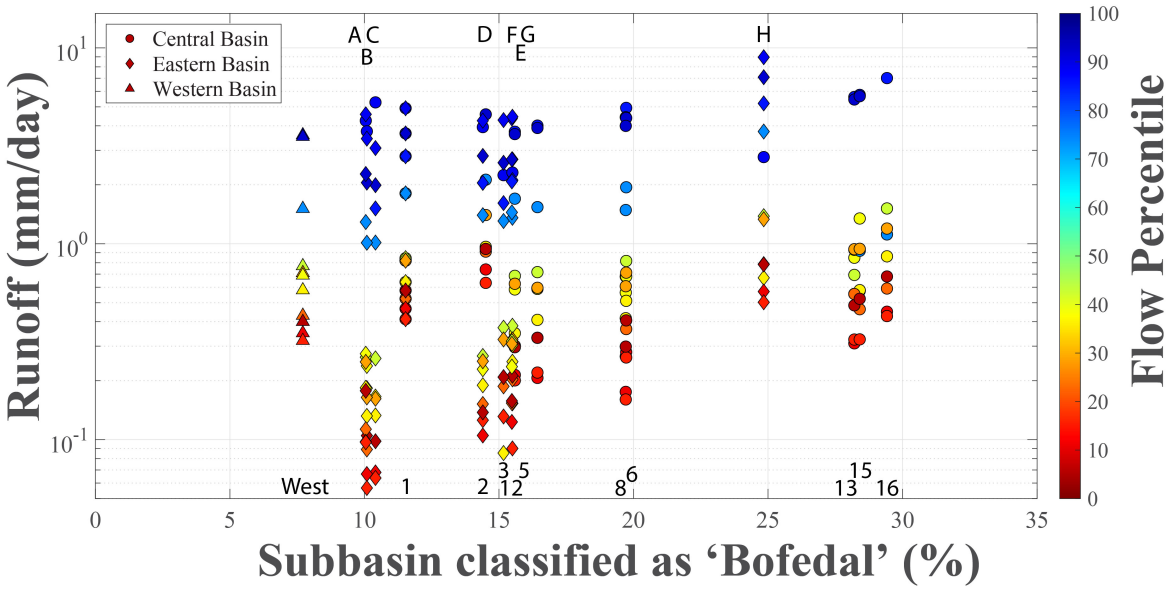

Figure 23. Scatterplot of the percent of each subbasin classified as *bofedal* (x-axis, linear) plotted against runoff (y-axis, log scale) for the URW Central and Eastern subbasins. The C-scale color-bar represents flow percentile of discharge at the Central stream gage over the course of water years 2019 and 2020. We measured discharge from the Western subbasin but treated it separately due to the abundance of karst weathered limestone in the upper Western subbasin not found in either the Central or Eastern subbasins. There is a suggestive positive correlation between percentage of a subbasin classified as 'Bofedal' and runoff.

Hydrologic productivity maps of the URW

We explored spatial variability of WY2020 runoff in the URW with four snapshots of hydrologic productivity created from distributed discharge measurements in nested subbasins taken in December 2019 and March 2020 (Figure 24, A and B, respectively), and July 2020 and August 2020 (Figure 25, A and B, respectively). Dates and associated flow percentiles of hydrologic productivity maps are highlighted blue in Table 6. The four dates correspond with the start of the wet season (December 2019), the

peak of the wet season and highest flow percentile measured via salt dissolution (March 10, 2020), the early dry season (July 1, 2020), and the late dry season and lowest flow percentile measured via salt dissolution (August 10, 2020). Site ‘1’ runoff (URW average unit water yield) for each corresponding date was 0.89 mm/day in December 2019, 3.66 mm/day in March 2020, 0.82 mm/day in July 2021, and 0.56 mm/day in August 2020. Hydrologic productivity maps display runoff in mm/day; thus, each discharge value has been scaled to its corresponding drainage area - enabling unit water yield comparison throughout the URW. Darker blue indicates greater runoff from a given region, and the diagonally striped salmon-colored regions are losing reaches when measured stream flow upstream exceeded streamflow at the immediate downstream discharge site. The same runoff bin values were used in all four maps to maintain consistency for data visualization purposes, and the darkest blue regions with runoff values that exceeded 5.0 mm/day on a given date are labeled with their respective runoff value.

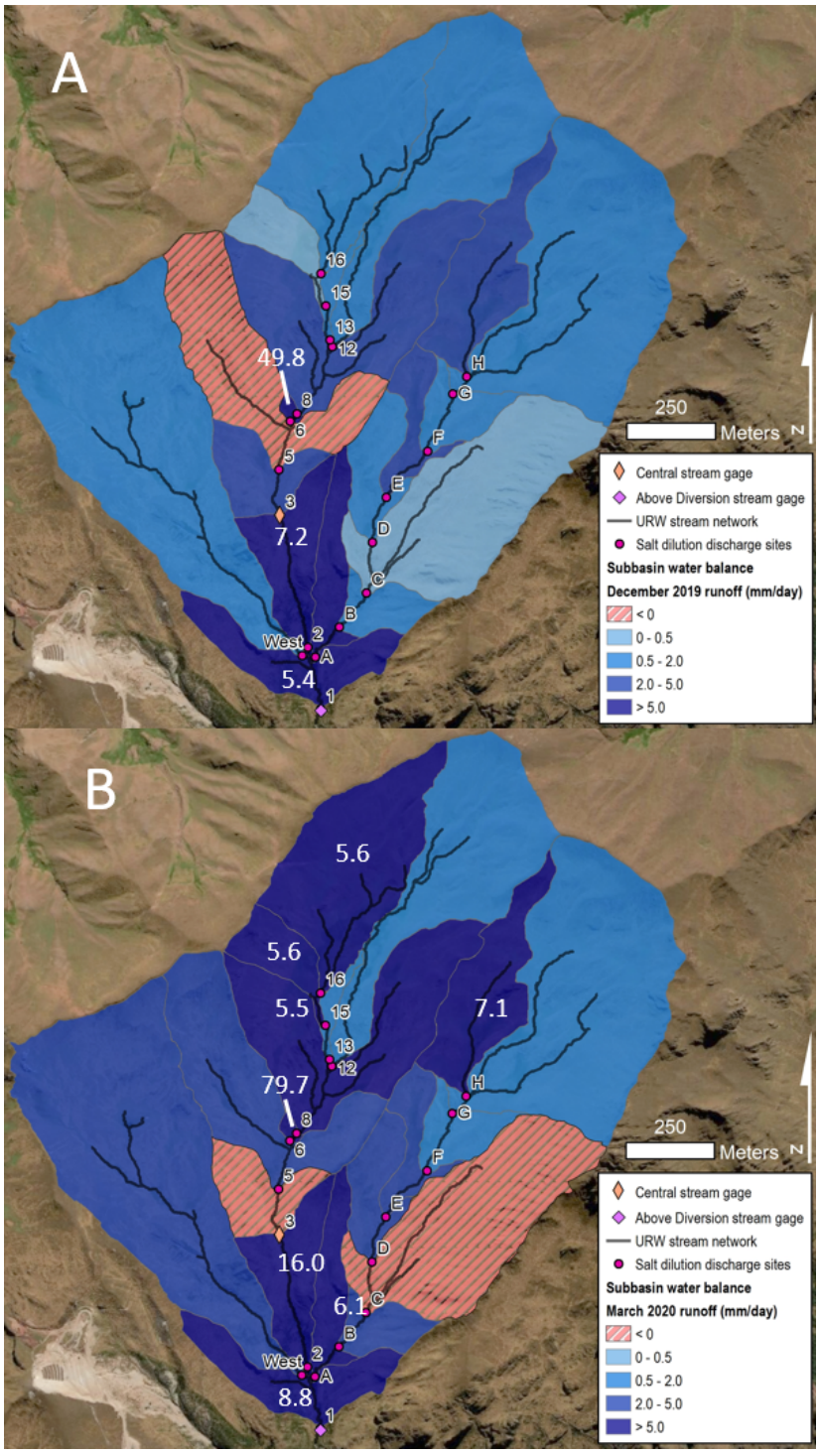

Figure 24. Two snapshots of 'hydrologic productivity' for subbasins during WY2020 wet season in A) December 2019, and B) March 2020. Salmon-colored regions

represent losing reaches and blue represents gaining reaches, scaled by runoff quantity. Site ‘1’ subbasin runoff (URW average unit water yield) for each corresponding date was A) 0.89 mm/day, and B) 3.66 mm/day, and flow percentiles for each date are listed in Table 5. The runoff value from regions that exceed daily runoff 5.0 mm/day (dark blue) are labeled in white on each map.

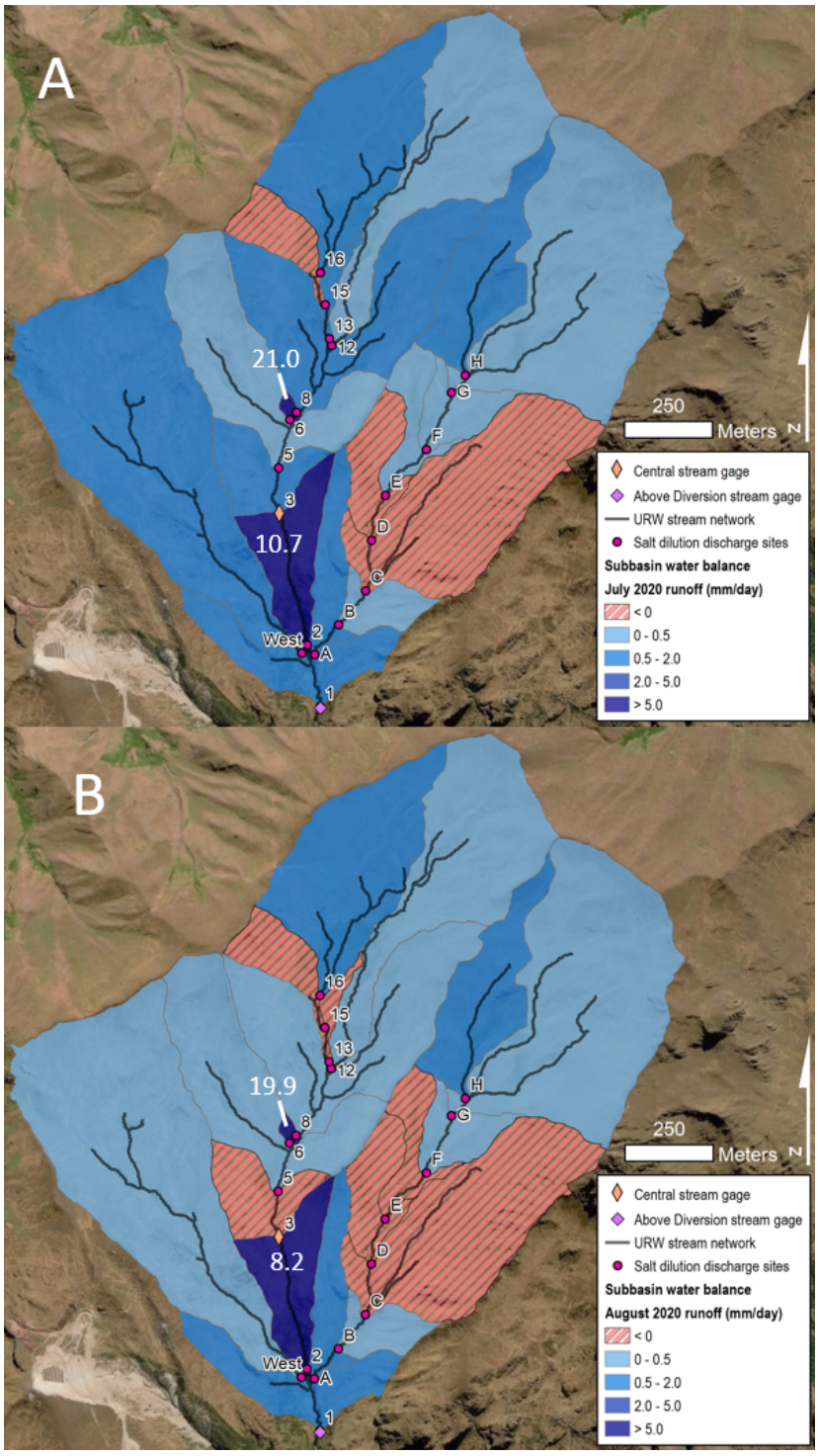

Figure 25. Two snapshots of 'hydrologic productivity' for subbasins during the WY2020 dry season in A) July 2020, and B) August 2020. Salmon-colored regions

represent losing reaches and blue represents gaining reaches, scaled by runoff quantity. Site ‘1’ subbasin runoff (URW average unit water yield) for each corresponding date was A) 0.82, and B) 0.56 mm/day, and flow percentiles for each date are listed in Table 5. The runoff value from regions that exceed daily runoff 5.0 mm/day (dark blue) are labeled in white on each map.

Two regions sustain the greatest runoff values on all four dates, displaying an order of magnitude greater runoff than the rest of the URW regardless of wet or dry season – the regions between sites ‘2’ and ‘3’ and between sites ‘6’ and ‘8’. Other regions of consistently high unit water yield are the subbasins draining to sites ‘16’ and ‘H’ in the Central and Eastern subbasin uplands, the region between sites ‘8’ and ‘12’, the Western subbasin, and the area between site ‘1’ and the confluence of the three major URW subbasins. The most consistent losing region occurred between sites ‘C’ and ‘D’ in the Eastern subbasin, which only measured a positive runoff value in December 2019. The area between site ‘15’ and ‘16’ was either losing or yielding relatively low runoff except for the wettest date surveyed in March 2020, and the region between sites ‘3’ and ‘5’ was a losing reach in March 2020 and August 2020 while producing substantial runoff contributions in December 2019 and July 2020.

Discharges along longitudinal profiles of the URW

Discharge results from nested subbasin discharge measurements are shown on the Central and Eastern subbasin longitudinal profiles (Figure 26). Figure 26 shows longitudinal profiles (top panel) of the Central (blue) and Eastern (red and grey dashed) subbasins and discharge in L/s on a log y-axis with position downstream along the longitudinal profile on the x-axis (bottom panel). Central subbasin discharge points are shown as circles and Eastern subbasin points as diamonds, with color corresponding to flow percentile calculated at the Central stream gage per date (Table 5). Note that discharge site labels for the Eastern and Central subbasin sites are placed on the top and

bottom of the discharge plot, respectively. Site 12 was omitted because its drainage area forms a small side tributary containing no upstream measurement sites.

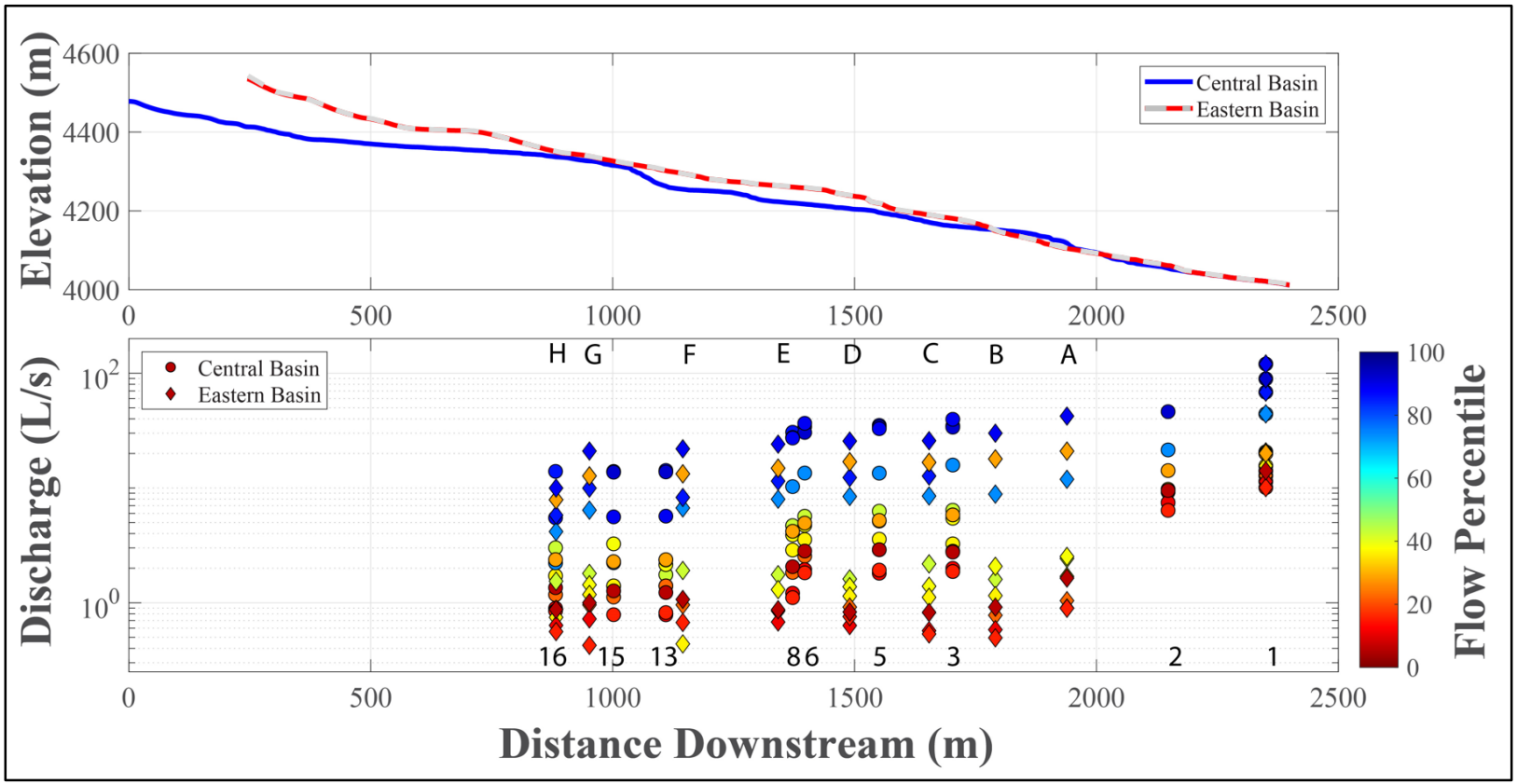

Figure 26. Longitudinal profiles (top) of the URW Eastern subbasin channel (red and black dashed line) and Central subbasin channel (blue solid line) with measured discharge shown (bottom) on a log y-axis, and position downstream along the longitudinal profile on the x-axis. Discharge values are colored with the c-axis color bar in correspondence with flow percentile of the date of discharge measurement, calculated from the Central stream gage daily discharge volumes. Discharge site label are placed on the bottom plot for reference, with Eastern subbasin site labels placed on the upper

part of the bottom plot (letters) and Central subbasin labels placed on the lower part of the bottom plot (numbers). Discharge site locations are shown on the map in Figure 13.

.

Estimations of *Bofedal* Contributions to URW Streamflow

To estimate total dynamic storage in *bofedales*, we combined *bofedal* borehole log observations from transects to calculate the 'drainable' portion of *bofedal* storage. We scaled up the drainable dynamic storage estimates to calculate a depth of storage per *bofedal* transect. Our results in this section present the results of the various components of our approach and then proceed to the storage estimate ranges for each *bofedal* transect, the mean range of which we upscaled to estimate total dynamic storage across all *bofedales* in the URW.

Table 7. Measurements of *bofedal* wetlands in which borehole transects were surveyed.

Bofedal	**Area (m^2)**	**Contributing hillslope area (m^2)**	**Maximum surveyed peat depth (cm)**
A	1,855	22,394	60
B	84,932	428,391	175
C	6,775	36,031	100
D	27,373	112,923	50

Bofedal cross-section models

The categorized peat, clay, and the underlying mineral layers observed in *bofedal* borehole surveys are shown along with water table depths in five cross-sections of borehole transects in *bofedales* A-D (Figure 27 - Figure 30). *Bofedal* boreholes where

NMR logs were taken are represented with a yellow point on the ground surface and an 'H' label (Figure 27, Figure 28), and points where borehole surveys were conducted without NMR represented with a brown square point on the ground surface. In Figure 27 - Figure 30, the ground surface elevation is represented by a bright green line if classified as 'Bofedal' and as beige asterisks if classified as 'Upland'. Boreholes with NMR logs in *bofedales* 'A' (Figure 28) and 'B' (Figure 27) are depicted in greater detail with the lower boundary of each observed layer delineated by a horizontal line. The lower boundary of peat is depicted as a solid beige line, the very plastic clay is depicted as a dashed red-brown line, and the water table depth is depicted as a dashed light blue line. The bottom boundary of each *bofedal* cross-section is represented by the dark blue dashed line, which was determined from the maximum water table depth observed from the seasonally dynamic range in the water table of Well 102 (*bofedal* A). The January 2020 water table in *bofedal* B is not displayed because it was at or near the ground surface, and we did not present the June 2019 water table in *bofedal* A due to a lack of data point density to interpolate a water table surface. IDW confidence of the *bofedal* cross sections in Figure 27 - Figure 30 is generally highest near borehole survey points and lowest where there is a large distance between borehole surveys and at the outer margins of the cross-sections.

Borehole NMR measurements are shown as blue circles in plots associated with Figure 27 and Figure 28. NMR plots show survey hole elevation on the y-axis, and x-axes of percent water content (left) and hydraulic conductivity estimates (right, logarithmic scale).

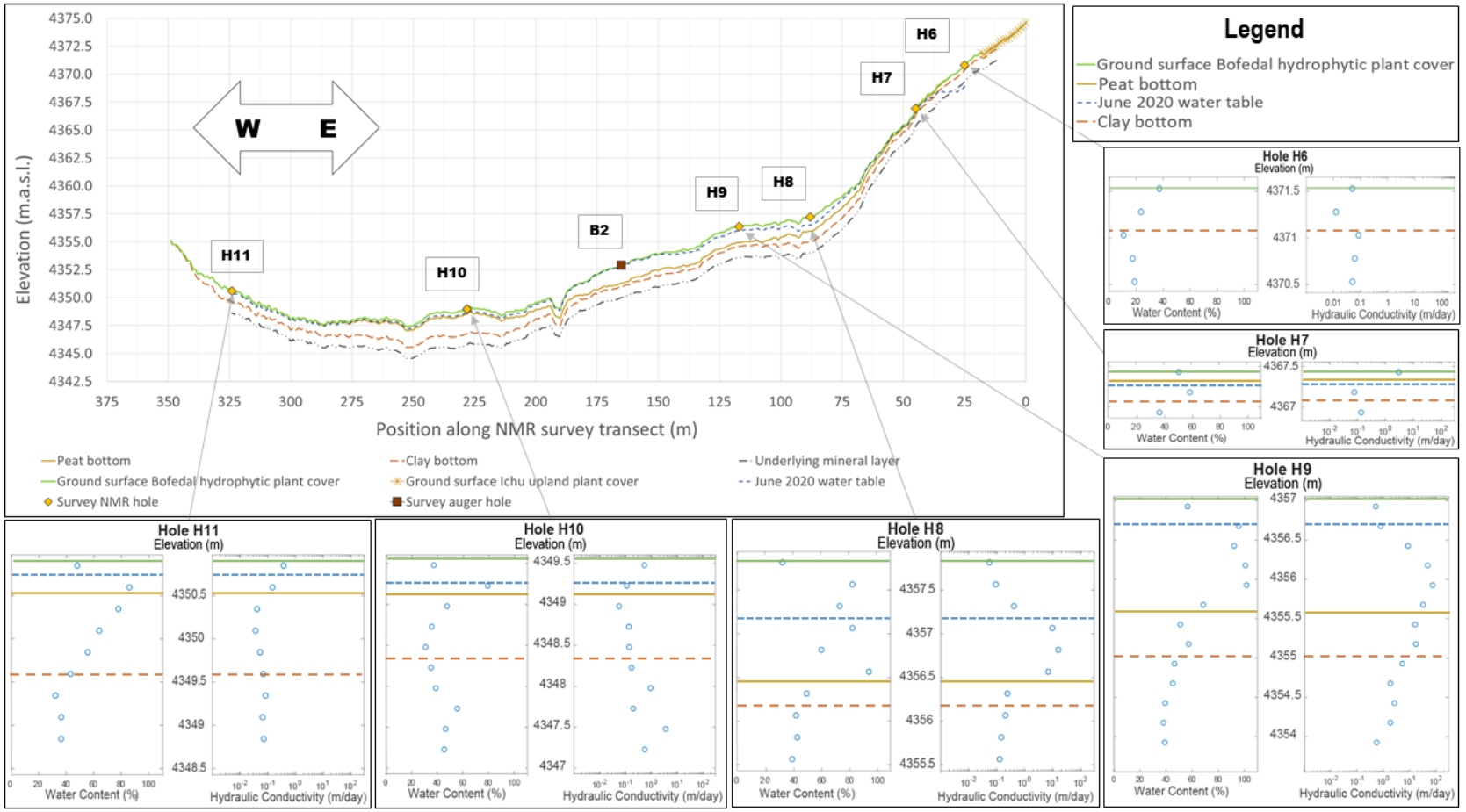

Figure 27. East-west cross-section of the largest URW *bofedal* (*bofedal* B) in the Central subbasin of the URW. Boreholes were augered in June 2019 ('H' series) and January 2020 ('B' series). Profiles are generated via a combination of borehole logs and downhole nuclear magnetic resonance (NMR) calculations of water content. We extracted the

ground surface elevation of points along the transect from a high-resolution 1-meter DEM that we produced from a photogrammetry drone survey (Figure 9) and extracted layer depth and porosity values using an inverse distance weighted (IDW) spatial interpolation approach in *ArcMap 10.6 Desktop*.

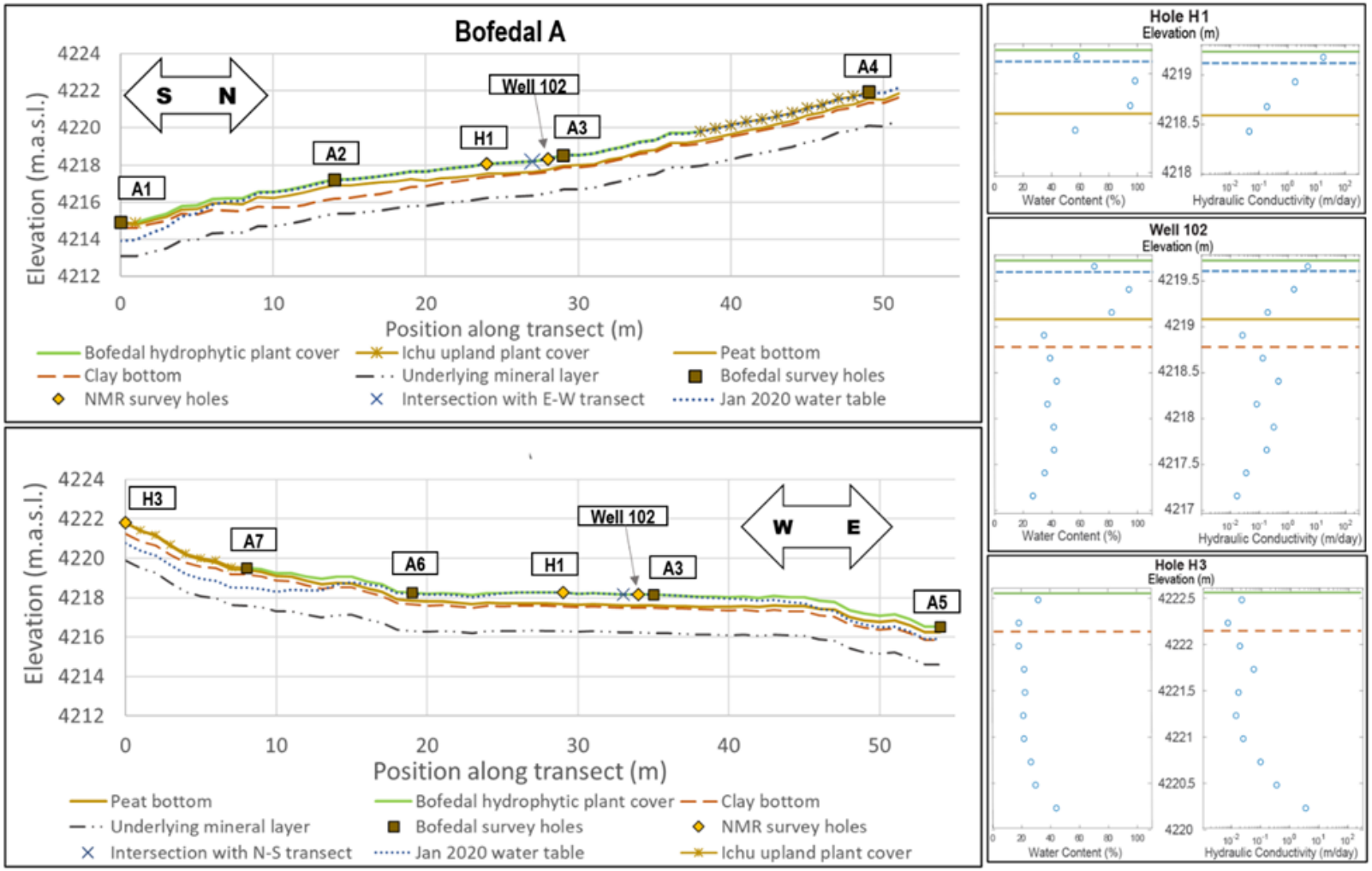
Bofedal A
S
N
A1
A2
H1
Well 102
A3
A4
Elevation (m.a.s.l.)
Position along transect (m)
Bofedal hydrophytic plant cover
Ichu upland plant cover
Peat bottom
Clay bottom
Underlying mineral layer
Bofedal survey holes
NMR survey holes
Intersection with E-W transect
Jan 2020 water table
H3
A7
A6
H1
Well 102
A3
A5
W
E
Peat bottom
Bofedal hydrophytic plant cover
Clay bottom
Underlying mineral layer
Bofedal survey holes
NMR survey holes
Intersection with N-S transect
Jan 2020 water table
Ichu upland plant cover
Hole H1
Elevation (m)
Well 102
Elevation (m)
Hole H3
Elevation (m)
Water Content (%)
Hydraulic Conductivity (m/day)

Figure 28. South-North and East-West cross-sections of *bofedal* A, located in the Central subbasin of the URW. 'H' series holes were augered in July 2019 and 'A' series holes were augered in January 2020. Profiles are generated via a combination of borehole logs and downhole nuclear magnetic resonance (NMR) calculations of water content. We extracted the ground surface elevation of points along the transect using a high-resolution 1-meter DEM that we produced from a photogrammetry drone survey (Figure 9) and extracted layer depths and porosity values using an inverse distance weighted (IDW) spatial interpolation approach in *ArcMap 10.6 Desktop*.

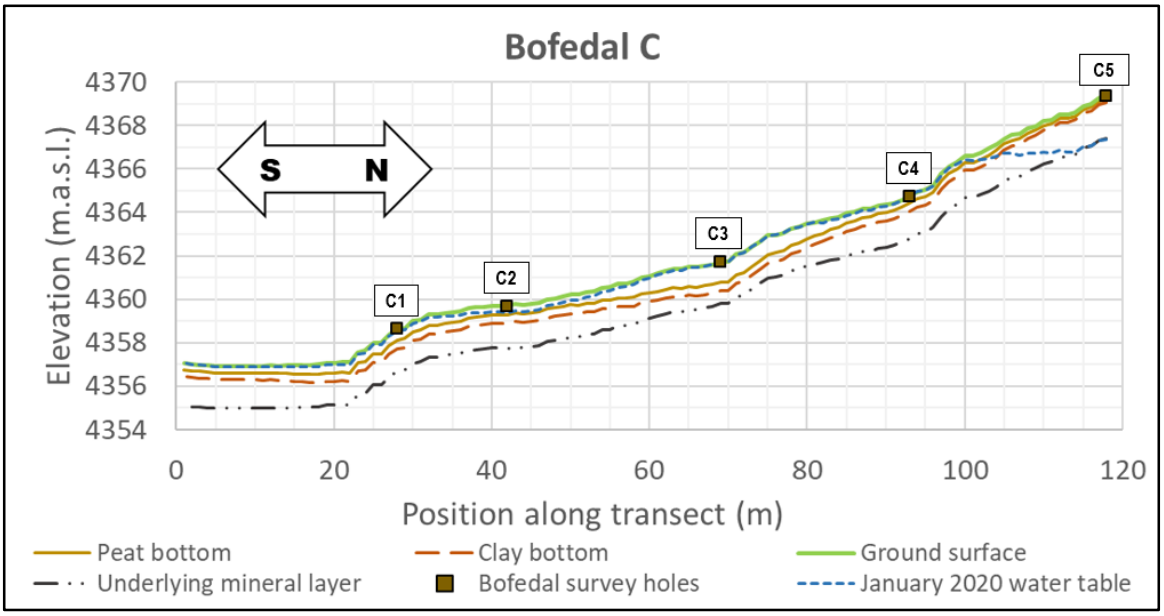

Figure 29. South-North cross-section of *bofedal* C, located in the Central subbasin of the URW. All *bofedal* C transect boreholes were taken with no NMR measurements in January 2020. We extracted the ground surface elevation of points along the transect using a high-resolution 1-meter DEM that we produced from a photogrammetry drone survey (Figure 9) and extracted layer depths using an inverse distance weighted (IDW) spatial interpolation approach in *ArcMap 10.6 Desktop*. Storage estimates were made with mean layer porosity values from *bofedales* A and B downhole NMR surveys conducted in June 2019.

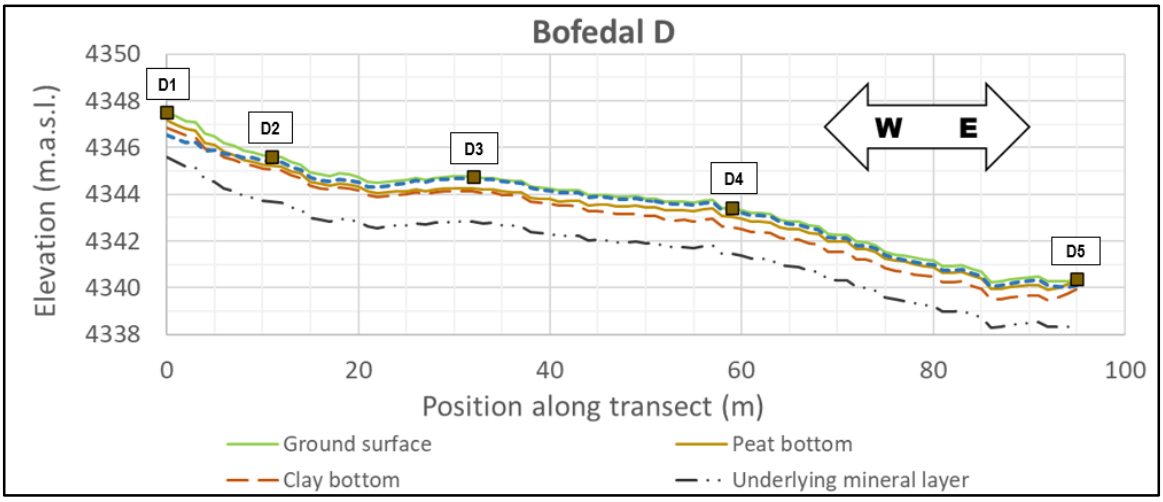

Figure 30. West-East cross-section of *bofedal* 'D', located in the Eastern subbasin of the URW. All *bofedal* D transect boreholes were taken with no NMR measurements in January 2020. We extracted the ground surface elevation of points along the transect using a high-resolution 1-meter DEM that we produced from a photogrammetry drone survey (Figure 9) and extracted layer depths using an inverse distance weighted (IDW) spatial interpolation approach in *ArcMap 10.6 Desktop*. Storage estimates were made with mean layer porosity values from *bofedales* A and B downhole NMR surveys conducted in June 2019.

Bofedal hydraulic parameters and storage estimates

NMR derived mean porosity and field capacity estimates of peat, clay, and underlying mineral layers used to calculate drainable dynamic storage in cross-sections (Figure 27 - Figure 30) are shown in Table 8. Standard deviations of NMR layer porosity measurements are shown by a '±' value. Drainable dynamic storage estimates in *bofedal* cross-sections are shown in Table 9.

Table 8. Calculated porosities and standard deviations for peat, clay, and the underlying mineral layer from saturated downhole NMR measurements during June 2019 surveys. Field capacity estimates were made from unsaturated NMR water content measurements in each layer at the margins of *bofedales* A and B in June 2019. Reported average porosity values per material layer were derived across the entire data set and thus may deviate from the average value of the reported porosities in *bofedales* A and B due to more measurements logged in *bofedal* B.

Subsurface layer	**Peat**	**Clay**	**Underlying mineral layer**
Bofedal A porosity	0.92 ± 0.12	0.46 ± 0.13	0.38 ± 0.046
Bofedal B porosity	0.86 ± 0.12	0.52 ± 0.13	0.39 ± 0.046
Mean NMR data set porosity	0.88 ± 0.12	0.51 ± 0.13	0.39 ± 0.046
Field capacity estimate	0.46	0.30	0.20

Table 9. Estimate ranges of drainable seasonal dynamic water storage in each *bofedal* cross-section.

Transect	**Drainable dynamic storage range (mm)**
Bofedal A S-N	400 - 460
Bofedal A W-E	325 - 375
Bofedal B	680 - 840
Bofedal C	390 - 470
Bofedal D	330 - 390
Mean	**430 - 510**

Expanding *bofedal* dynamic storage to local subbasin and URW scales

Drainable dynamic storage estimates from cross-sections in the four surveyed *bofedales* were upscaled to determine the drainable dynamic storage that each *bofedal* represents relative to its contributing upslope area (Table 10), and the mean drainable dynamic storage upscaled to determine the storage of all *bofedales* relative to the URW (Table 10). We determined that the dynamic storage of *bofedales* across the URW contributes 50 - 60 mm to dry season runoff in the URW.

Table 10. Estimate ranges of drainable seasonally dynamic water storage of *bofedal* wetlands for the contributing watershed to each surveyed *bofedal* and across the entire URW.

Site	**Area (m^2)**	**Contributing area (m^2)**	**Drainable dynamic storage range (mm)**
Bofedal A	1,855	22,394	30 - 35
Bofedal B	84,932	428,391	135 - 166
Bofedal C	6,775	36,031	73 - 88
Bofedal D	27,373	112,923	80 - 95
URW	**244,000**	**2,112,000**	**50 - 60**

Hydraulic conductivity estimates in *bofedal* layers

NMR derived estimates of mean saturated hydraulic conductivity of peat were 14.3 m/day, clay was 2.6 m/day, and the underlying mineral layer was 0.5 m/day (Table 11). In all layer cases, the standard deviation was of a similar or greater value than the mean hydraulic conductivity estimate, indicating that there was substantial heterogeneity and range in the subsurface pore size distribution of NMR borehole survey layers. While standard deviations in the hydraulic conductivity measured in each layer are substantially large there is a general trend of both decreasing hydraulic conductivity and decreasing standard deviation with increasing depth (Table 11).

Table 11. Estimates of saturated hydraulic conductivity and standard deviations of peat, clay, and the underlying mineral layer. Data generated from downhole NMR surveys of saturated peat, clay, and underlying mineral layer in *bofedales* 'A' and 'B'.

Subsurface layer	**Peat**	**Clay**	**Underlying mineral layer**
Mean saturated hydraulic conductivity (m/day)	14.32 ± 13.05	2.63 ± 6.22	0.50 ± 0.75

DISCUSSION

The URW is a small (2.12 km^2) humid puna headwater catchment in the Vilcanota Watershed. Our study, over WY2019 and WY2020, integrated comprehensive *in-situ* monitoring, hydrologic analyses and novel approaches to quantify dynamic storage in *bofedales* and spatiotemporal patterns in water yield. In this section, we discuss the core findings and implications of our study pertaining to water yield in the humid puna, with a focus on dynamic storage and contributions from *bofedales*. We present a conceptual model of *bofedal* hydrology in the puna landscape. We intend that our findings and interpretations be used to inform regional scientific, conservation, and management approaches pertaining to *bofedales*, the humid puna landscape, and population centers that rely on puna derived water resources.

Water Yield in the Humid Puna

Multiple studies seeking to predict how climate change will influence water resources in the Andes point to a paucity of multi-year hydrologic data sets at the catchment scale (Bradley et al., 2006; Herzog et al., 2011; Drenkhan et al., 2015; Somers et al., 2019). There are, however, very few published annual water balances that establish quantitative baselines for comparison, thus our study makes a valuable contribution towards establishing reference headwater catchment water balances in the context of regional water resources *in-situ* data scarcity (Bradley et al., 2006; Herzog et al., 2011; Wohl et al., 2012; Drenkhan et al., 2015; Buytaert et al., 2017; Somers et al., 2019). Our

study expands upon the water balances presented by Ochoa-Tocachi et al. (2016) and fills in a mechanistic gap of where moisture is stored and from where runoff is sourced within a humid puna catchment.

In the water balances produced over the two water years, runoff at the Central stream gage (0.806 km^2) accounted for 489 mm (62%) and 614 mm (71%) of annual precipitation in WY2019 and WY2020, respectively (Table 3). Central stream gage runoff differences between WY2019 and WY2020 were largely attributable to greater precipitation in WY2020 than in WY2019. Despite more precipitation received in WY2020 than in WY2019, dry season runoff in WY2019 composed a greater proportion of precipitation (15%) than in WY2020 (11%) (Table 3). The difference between WY2019 and WY2020 dry season runoff proportions was likely due to the light-severity grassland fire that swept through parts of the URW Western and Central subbasins in July 2019, resulting in a vigorous WY2020 growth response from plants in burnt areas that retained intact root systems - evidenced by the increased subsurface moisture deficit at the end of WY2020 (Figure 16).

Runoff accounted for 80% of precipitation (689 mm) in WY2020 at the Above Diversion stream gage (2.11 km^2, Table 3). Importantly, runoff measured at the Above Diversion stream gage represents the total URW water yield that may be diverted for agricultural use in the eastern sector of Zurite and was thus the metric used to compare agricultural water demand to the potential irrigation subsidy from the URW (Figure 22). Runoff over the dry season amounted to 130 mm (19% of all WY2020 runoff) – double the dry season runoff at the Central stream gage over the same period (Table 3). Although

there was a substantial difference in WY2020 runoff estimates between the Above Diversion and Central stream gage water balances (Table 3), both stream gage rating curves reflect high quality data and good rating curve fits (Appendix C). Additionally, results from spatially distributed discharge measurements in nested subbasins corroborate large streamflow contributions from the Central subbasin between the Central and Above Diversion stream gages, regardless of wet or dry season (reach between sites '2' and '3', Figure 24, Figure 25), as well as large streamflow contributions from the URW Western subbasin ('West' site, Figure 24, Figure 25), the details of which we discuss further, below.

Our results in the URW demonstrate the hydrologic productivity of humid puna landscapes and suggest that key mechanisms exist which result in sustained perennial streamflow over a 5-month dry season with 20 mm, or less, of precipitation. Furthermore, the hydrologic productivity of humid puna catchments such as the URW may explain a substantial portion of dry season runoff in the Vilcanota Watershed not derived from glacier sources (Buytaert et al., 2017).

Despite sustained baseflow water yield in the URW (11 L/s or greater at the Above Diversion stream gage, Figure 20, Table 3), irrigation water demand in Zurite substantially exceeds combined precipitation and potential irrigation subsidies from the URW during the dry season (Figure 22). Irrigation demand for crops grown in Zurite during the dry season – namely fava beans and feed crops – is greater than that of crops grown in the wet season. The greatest potential impact that URW water yield can have as a direct irrigation subsidy (excluding interseasonal water storage for irrigation) occurs in

the transitions between the wet and dry seasons (early in the Release and Fill-up phases, Figure 21) during the months of April, May, October, and November (Figure 22).

Historic interruptions to the regional Sambor Huaypo irrigation distribution network (spanning months without reliable water supply) and an absence of long-term water storage leave Zurite, like many communities throughout the Andes, in a tenuous position of water security. The URW is, thus, an important local perennial water supply that can augment irrigation demand. We recommend that Zurite pair the development of additional water storage infrastructure with approaches to improve irrigation efficiency, such as converting to sprinkler or drip irrigation systems. Implementing proactive solutions to address future water shortages will boost the resilience of Zurite agriculture to drought conditions and may increase crop yields - particularly in periods of water scarcity during the dry season.

Bofedales and Water Yield in the URW

The annual runoff ratio in the URW (the proportion of precipitation leaving the watershed as runoff) ranged from 0.62 to 0.80. Dry season runoff accounted for up to 19% of annual runoff (Table 3). To our knowledge, the only hydrologic data from a comparable humid puna catchment reported a runoff ratio of 0.70 in HUA 1 (Ochoa-Tocachi et al., 2106). HUA 1 is a minimally disturbed 4.22 km^2 headwater humid puna catchment located in the Peruvian Andes uplands of Huaraz, Ancash, spanning an elevation range from 4,280 to 4,480 m.a.s.l. (Ochoa-Tocachi et al., 2016). The land cover description of HUA 1 shares many commonalities to the URW in both land cover types

and proportions - with 60% tussock grass, 25% nude rock/bare soil, and 15% wetland coverage. Of the catchments studied in Ochoa-Tocachi et al (2016), HUA 1 was the only humid puna catchment with a comparable proportion of wetland area to the URW and measured the highest runoff ratio amongst the studied humid puna catchments by a substantial margin. Runoff data from HUA 1 indicated a perennial stream with sustained baseflows that had a nearly identical runoff range to the URW Central stream gage, from 0.1 to 10 mm/day, however there was no distinction in the percentage of runoff that occurred during the dry season. Similar to our results, however, both headwater humid puna catchments had high runoff ratios, sustained perennial runoff, and had high proportions of wetland (*bofedal*) area, highlighting the need to elucidate the role of *bofedales* in sustaining perennial streamflow.

Our data suggest that perennial streamflow in the URW is linked to land cover, and in particular the presence of *bofedales*. *Bofedales* cover 11.5% of the URW. We found that the proportion of subbasins covered in *bofedales* was a key indicator for hydrologic productivity. Runoff increased with the percent of *bofedal* covering each subbasin area (Figure 23), and this trend strengthened through the dry season. Whereas the relationship between percent *bofedal* and runoff was represented by a linear trend in the wet season ($q = 0.2135(\%\ bofedal) - 0.0338$, $r^2 = 0.62$), the relationship was best represented by a power law during the lowest flow percentile date of the dry season ($q = 0.0076(\%\ bofedal)^{1.29}$, $r^2 = 0.40$) (Figure 23). We note the general trend in the URW does not apply to three outliers at sites '1' (Above Diversion stream gage), '2' (Central subbasin), and 'West' (Western subbasin).

Site ‘1’ received streamflow contributions from the ‘2’ and ‘West’ outlier sites. In the reach between sites ‘2’ and ‘3’, large runoff contributions may be due to a steep reach of bedrock-confined channel and a broad shift in valley morphology from a U-shaped valley upstream to a narrower, V-shaped valley downstream. Runoff in the reach was substantial in both the wet and dry seasons (Figure 24, Figure 25), comprising URW streamflow contributions that were likely linked to the high proportion of annual runoff (80%) in the WY2020 Above Diversion stream gage water balance (Table 3). The narrowing in valley morphology and the presence of bedrock in the channel may force water held in off-channel aquifers in the upstream U-shaped section of the reach to the channel. This interpretation is supported by large groundwater contributions to streamflow where talus slopes impinged upon a meadow aquifer in a proglacial catchment of the Cordillera Blanca (Gordon et al, 2015).

Large runoff values in the Western subbasin may be associated with large extents of limestone karst in the headwaters, which may store and transmit large volumes of water (Somers and McKenzie, 2020). Our study did not focus on the role of limestone in Western basin runoff, however, baseline electrical conductivity measurements taken during salt dissolution discharge measurements at the ‘West’ site were abnormally high - often exceeding twice the baseline readings throughout the Central and Eastern subbasins. This suggests higher rates of chemical dissolution and the potential of large amounts of groundwater storage in the limestone karst of the Western subbasin.

Despite potential morphological and lithologic controls on runoff in the URW, the positive relationship between *bofedal* extent and runoff in the URW is consistent with the

reported relationship between increased wetland extent and increased runoff in the Ecuadorian Páramo (Mosquera et al, 2016). Our study contributes a novel finding of positive correspondence between the extent of *bofedales* and runoff generation in a headwater humid puna catchment.

Drainable dynamic storage of *bofedales*

Bofedales A-D integrate upslope contributing areas ranging from 4 - 12 times their respective areas (Table 7). The WY2020 recharge and saturation of Well 102, in *bofedal* A, corresponded with the period over which VWCs in the soil and saprolite reached field capacity in the hillslope (Figure 16). These observations suggest that *bofedales* fill and drain in response to upslope groundwater contributions, consistent with recent studies in southern Perú (Cooper et al., 2019). Furthermore, our results suggest that the supply of hillslope groundwater into *bofedal* A either matched or exceeded the groundwater discharge rate from *bofedal* A over the first 45 days of the Release phase (i.e., start of the dry season), when Well 102 was saturated with a virtual absence of direct precipitation to recharge outflow (Figure 21, Table 4).

Our estimates of drainable dynamic storage in URW *bofedales* A-D focused on the annual groundwater recession that occurred primarily throughout the dry season, between the Release and Fill-up phases (Figure 17, Figure 21), from July 4th to November 25th in 2020. Estimates of the quantity of water held primarily in peat, but also in the underlying clay and mineral layers, ranged from 325 mm to 840 mm - with an average drainable dynamic storage range of 330 mm to 410 mm (Table 9). At the scale of the URW, the mean range of *bofedal* drainable dynamic storage applied to the total extent

of *bofedales* in the URW indicated that *bofedales* could contribute 50 – 60 mm of runoff over the period when the Well 102 groundwater dropped. During this same period, runoff in the URW was 135 mm. Our estimate of *bofedal* contributions to streamflow represent approximately half of the measured URW runoff over the same period.

The only published study to our knowledge that quantified the storage capacity of a *bofedal* estimated 2,000 mm of potential storage (Valois et al., 2020), approximately four times the range in drainable dynamic storage that we estimated. However, there were two notable limitations to the study of Valois et al. (2020). First, the storage estimates of Valois et al. (2020) relied exclusively on the measured porosity values of alluvial fill to estimate *bofedal* storage and did not account for the substantial storage capacity of superficial peat that was demonstrated by NMR results in our study (Table 8). The second limitation of Valois et al. (2020) is a lack of distinction between total storage capacity and the portion of *bofedal* storage that might contribute to streamflow (e.g., Abdelnour et al., 2011) - leaving a notable gap in published studies that estimate potential streamflow contributions from *bofedales*. Our results make a valuable contribution to hydrologic studies of *bofedales* by addressing the key limitations of Valois et al. (2020) while also linking trends between *bofedal* spatial distribution and runoff to estimates of *bofedal* runoff contributions.

Error in bofedal drainable dynamic storage estimates

There are three primary sources of error that may not have been accounted for in our approach to quantify *bofedal* drainable dynamic storage. First, there may be error associated with the spatial heterogeneity of *bofedal* layer depths and hydraulic parameters

that was not fully captured in our approach. Although we designed *bofedal* borehole transects to capture spatial heterogeneity within each *bofedal,* there was likely heterogeneity within each of the layers and layer hydraulic parameters that was not fully captured - evidenced by the substantial range in standard deviation reported for layer saturated hydraulic conductivity estimates (Table 11). Conversely, NMR derived porosity results were much better constrained (Table 8), allowing for reasonable confidence in drainable dynamic storage estimates (Table 9).

The second potential source of error lies within the assumption that the annual dynamic depth range of the groundwater table in *bofedales* B-D was similar to the measured groundwater table depth range in *bofedal* A. The saturation of Well 102, in *bofedal* A (Figure 21), corresponded with the abrupt WY2020 increase in URW runoff response, corroborating the assumption that *bofedales* across the URW saturated and began to shed precipitation inputs within a similar time frame (i.e., entered the Steady state phase). However, there remains a degree of uncertainty regarding the annual dynamic groundwater depth range in *bofedales* B-D.

The third source of potential error in our estimates lies within the extrapolation of *bofedal* drainable dynamic storage estimates to the URW catchment scale (Table 10). There are likely differences in *bofedal* characteristics and hydrology within the URW that were not captured when drainable dynamic storage estimates were extrapolated to the catchment scale. We did not explicitly quantify the potential propagation of error in extrapolated URW *bofedal* drainable dynamic storage estimates; however, there is likely

unquantified error in estimated *bofedal* runoff contributions that is associated with the extrapolation to the catchment scale.

We applied the standard deviations of NMR derived porosity values per subsurface layer material (Table 8) to the portions of drainable dynamic storage calculated in each layer cross-section (Figure 27 - Figure 30) as our primary source of spatial uncertainty. We did not explicitly quantify spatial error that may be associated with the IDW interpolation approach used to develop *bofedal* A-D transect cross sections (Figure 27 - Figure 30). Future research efforts that seek to quantify streamflow contributions of *bofedales* via estimations of drainable dynamic storage should incorporate groundwater monitoring wells in each studied *bofedal* to accurately capture the annual range in groundwater table depth. Additionally, improved data resolution of the spatial heterogeneity of *bofedal* layering could be achieved with a higher density of borehole logs throughout studied *bofedales*, or perhaps via surface based geophysical techniques. These efforts may better quantify heterogeneity in hydrologic properties to predict *bofedal* contributions to runoff more accurately.

Conceptual Model of *Bofedal* Hydrology

Bofedales form an important hydrologic interface between groundwater draining the humid puna uplands and streamflow. We interpret *bofedales* as waystations that collect groundwater contributions from large areas and limit the release of this water to streams (Figure 31). The combination of a low gradient groundwater table within the gently sloping *bofedales*, a voluminous reservoir present in the high porosity peat, and an

underlying low conductivity layer allow for a large capacity of seasonally dynamic storage and a 'valve' that regulates the flow of water off the landscape. Here, we discuss the function of *bofedales* in relation to groundwater drainage from the hillslopes in the context of the three-phase water year (Figure 21).

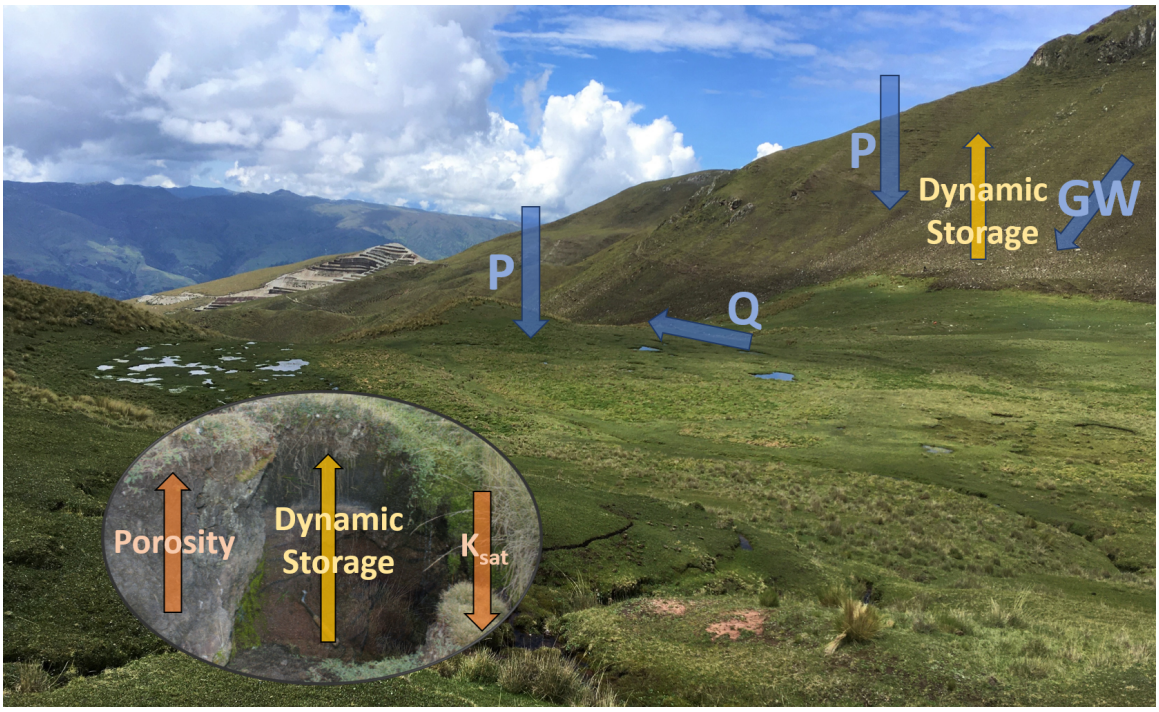

Figure 31. Conceptual model of *bofedal* hydrology with a photo of *bofedal* B looking southwest towards the quartzite ridge divide between the Central and Western subbasins. Yellow arrows indicate dynamic storage in the hillslopes and in the *bofedal.* Orange arrows represent increasing porosity upwards through the mineral layer, clay, and peat, and decreasing conductivity with depth. Blue arrows represent the pathway of precipitation inputs, groundwater delivery to the *bofedal* and runoff generation in streams.

The return of precipitation at the beginning of the water year marks the start of the Fill-up phase. Subsurface soil and saprolite moisture on the hillslope have been depleted

to water contents well below field capacity due to grass water uptake, and the groundwater table in the *bofedales* is 1-2 m below the ground surface. During the first part of the Fill-up phase, precipitation recharges the rooting zone of grasses on the hillslope and a portion of the dynamic storage in the *bofedales.* In WY2020, 160 mm of cumulative precipitation directly recharged *bofedal* A, causing a Well 102 groundwater table response in which approximately 40% of the seasonal dynamic storage filled, approaching the subsurface boundary between peat and clay. Although we did not directly measure moisture dynamics in the deep (20 + m) unsaturated zone beneath the hillslopes, we observed the rooting depth of grass to be limited to approximately 120 cm. There is thus no physical mechanism for the water contents of unsaturated bedrock to fall below field capacity. Once field capacity is reached in the rooting zone of hillslope grasses, additional precipitation infiltrates rapidly through the rooting zone and underlying unsaturated bedrock to cause a rise in the hillslope groundwater table, leading to increased drainage of hillslope moisture towards *bofedales*. *Bofedales* integrate hillslope areas 4-12 times their size, and thus the groundwater table in *bofedales* rises rapidly to the surface, saturated. In WY2020, the remaining 60% of seasonal dynamic storage in *bofedal* A, represented mostly by porous peat, filled with an additional 10-20 mm of precipitation that caused the Well 102 groundwater table to reach the surface (Figure 17).

Once the groundwater table in the *bofedales* reaches the surface, the system enters the Steady-state phase. At this point, there is little additional dynamic storage in the URW, and successive precipitation causes rapid runoff responses via preferential flow

pathways, sustaining high flows throughout the wet season (Figure 21). Although precipitation event frequency decreases through the transition between the wet and dry seasons, cumulative runoff continues to track cumulative precipitation while the seasonal dynamic storage pools in the system remain mostly full (Figure 21).

The start of the dry season occurs when cumulative 15-day antecedent precipitation drops below 10 mm, marking the beginning of the Release phase (Figure 21). With a near absence of precipitation, dynamic storage pools on the hillslope and in the *bofedales* begin to drain. On the hillslopes, drainage occurs primarily via evapotranspiration that depletes soil water contents to values substantially below field capacity (Figure 16). Groundwater in the hillslopes continues to drain into *bofedales*, sustaining the saturated state of *bofedales* well into the Release phase (45 days in WY2020). As the hillslope groundwater table drains, the groundwater gradient linking hillslopes to *bofedales* becomes shallower, and the rate of water leaving the *bofedales* likely exceeds contributions from hillslopes. Consequently, there is a slow and steady *bofedal* water table recession as *bofedales* drain water to streams, sustaining baseflow. Moisture depletion below field capacity likely occurs in the peat and upper clay layers, sustaining ET from hydrophytic plants that reside in *bofedales*.

Our interpretation is that *bofedales* represent a shallow and distributed aquifer network that integrates groundwater contributions from upslope, stores large volumes of water, and ultimately slows the drainage of water to streams, sustaining baseflow. Our estimates of dry season streamflow contributions from *bofedales* represent a water yield quantity from two snapshots of the dynamic range bounds of *bofedal* groundwater table

depths. However, they do not account for the cumulative volume of water which passes through *bofedales*. Our conceptual model suggests that *bofedales* pass far more water to streams than 50-60 mm and should thus be considered active regulators of streamflow rather than static pools that fill and drain seasonally. They may play a large role in baseflow generation throughout the Vilcanota Watershed; however, expanded monitoring and modeling efforts are needed to test this hypothesis.

CONCLUSION

This study quantified the water yield from a humid puna headwater catchment with WY2019 and WY2020 annual water balances of two nested subbasins within the 2.12 km^2 URW in Zurite, Perú. Runoff accounted for the greatest proportion of the annual water balance by a substantial margin, ranging from 62% up to 80% of the annual precipitation. Dry season runoff comprised between 11% and 19% of all runoff, demonstrating the capacity of headwater humid puna catchments to generate perennial streamflow within the Vilcanota Watershed.

Spatiotemporal analyses of water yield with 12 spatially distributed discharge measurement sets in 19 nested subbasins of the URW showed a positive relationship between the percentage of *bofedal* land cover and runoff throughout the year. The relationship appeared to strengthen in the dry season.

Our data suggests that *bofedales* are closely linked to hillslope groundwater that drains from upland areas multiple times the area of *bofedales* themselves, and that hillslope groundwater continued to flow into *bofedales* well into the dry season. We estimate the drainable dynamic storage in *bofedales* across the URW to be 50-60 mm, accounting for approximately half of the dry season streamflow; however, these estimates should be considered minimum dry season contributions to streamflow. Our study indicates that the role of *bofedales* in integrating, storing, and releasing water from hillslopes appears to sustain baseflow.

The results of our study show the hydrologic importance of *bofedales* to water resources in the Andean puna. Future research should be directed at coupling predictions of the expansion of the humid puna into glacierized areas and assessing the source of perennial streamflow from additional catchments distributed throughout the humid puna. We intend that our findings be used to inform local water management and land conservation decisions in the district of Zurite, and that our analyses may be used to proactively address regional water security concerns in the semi-arid climate of the Vilcanota Watershed and the Central Andes.

LITERATURE CITED

Aybar, C., Fernández, C., Huerta, A., Lavado, W., Vega, F., Felipe-Obando, O. (2020). Construction of a high-resolution gridded rainfall dataset for Perú from 1981 to the present day, Hydrological Sciences Journal, 65:5, 770-785, DOI: 10.1080/02626667.2019.1649411.

Barnett, T.P., Adam, J.C., Lettenmaier, D.P., (2005). Potential impacts of a warming climate on water availability in snow-dominated regions. Nature 438, 303–309.

Baraer M, McKenzie JM, Mark BG, Bury J and Knox S (2009). Characterizing contributions of glacier melt and groundwater during the dry season in a poorly gauged catchment of the Cordillera Blanca (Perú). Adv. Geosci., 22, 41–49.

Baraer, M., McKenzie, J., Mark, B. G., Gordon, R., Bury, J., Condom, T., et al. (2015). Contribution of groundwater to the outflow from ungauged glacierized catchments: a multi- site study in the tropical Cordillera Blanca, Perú. Hydrological Processes, 29(11), 2561–2581.

Bean, E.Z., Huffaker, R.G. and Migliaccio, K.W. (2018), Estimating Field Capacity from Volumetric Soil Water Content Time Series Using Automated Processing Algorithms. Vadose Zone Journal, 17: 1-12 180073. https://doi.org/10.2136/vzj2018.04.0073

Behroozmand, A. A., Dalgaard, E., Christiansen, A. V., & Auken, E. (2013). A comprehensive study of parameter determination in a joint MRS and TEM data analysis scheme. Near Surface Geophysics, 11(5), 557–567. https://doi.org/10.3997/1873-0604.2013040

Bradley, R. S., Vuille, M., Diaz, H., and Vergara, W. (2006). Threats to water supplies in the tropical Andes. Science, 312: 1755–1756.

Buytaert, W., Celleri, R., De Bièvre, B., Hofstede, R., Cisneros, F., Wyseure, G. and Deckers, J. (2006). Human impact on the hydrology of the Andean páramos. Earth-Sci. Rev. 79, 53–72.

Buytaert W, Moulds S, Acosta L, De Bièvre B, Olmos C, Villacis M, Tovar C, Verbist KMJet al. (2017). Glacier melt content of water use in the tropical Andes, Environmental Research Letters, Vol: 12, ISSN: 1748-9326

Carlotto, V., Concha, R., Cárdenas, J., Garcia, B., Villafuerte, C. (2010) Geoloía y Geodinåamica en la Quebrada Qenqo: Aluviones que Afectaron Zurite-Cusco. Informe Tecnico. INGEMMET, UNSAAC.

Célleri, R., Buytaerte, W., Bievre, B., Tobon, C., Crespo, P., Molina, J. Feyen, J. (2010). Understanding the hydrology of tropical Andean ecosystems through an Andean Network of Basins. IAHSAISH Publication 336: 209–212.

Chimner, R. A., and Karberg, R. (2008). Long-term carbon accumulation in two tropical mountain peatlands, Andes Mountains, Ecuador. Mires and Peat, 3 (article 4): 1–10.

Cooper, D. J., Wolf, E., Colson, C., Vering, W., Granda, A., and Meyer, M. (2010). Alpine peatlands of the Andes, Cajamarca, Perú. Arctic, Antarctic, and Alpine Research, 42: 19–33.

Cooper, D., Kacynaski, K., Slayback, D. Karina, Y. (2015). Growth and Organic Carbon Production in Peatlands Dominated by Distichia muscoides, Bolivia, South

America. Arctic, Antarctic, and Alpine Research, Vol. 47, Nov. 3, 2015, pp. 505-510.

Cooper, D. J., Sueltenfuss, J., Oyague, E., Yager, K., Slayback, D., Caballero, E. M. C., Mark, B. G. (2019). Drivers of peatland water table dynamics in the Central Andes, Bolivia and Perú. Hydrological Processes, 33(13), 1913–1925. https://doi.org/10.1002/hyp.13446.

Córdova M, Carrillo-Rojas G, Crespo P, Wilcox B, Célleri R. (2015). Evaluation of the Penman-Monteith (FAO 56PM) method for calculating reference evapotranspiration using limited data. Mountain Research and Development 35(3): 230–239. DOI:10.1659/MRDJOURNAL- D-14-0024.1

Dralle, D.N., Hahm, W.J., Rempe, D.M., Karst, N.J., Thompson, S.E., Dietrich, W.E. (2018): Quantification of the seasonal hillslope water storage that does not drive streamflow. Hydrological Processes . DOI: https://doi.org/10.1002/hyp.11627

Drenkhan, F., Carey, M., Huggel, C., Seidel, J., Ore, M.T. (2015). The changing water cycle: climatic and socio-economic drivers of water-related changes in the Andes of Perú.WIREs Water, 2 (2015), pp. 715-733.

Drenkhan, F., Guardamino, L., Huggel, C., Frey, H. (2018) Current and future glacier and lake assessment in the deglaciating Vilcanota-Urubamba basin, Peruvian Andes, Global and Planetary Change,Volume 169, 2018, Pages 105-118, ISSN 0921-8181, https://doi.org/10.1016/j.gloplacha.2018.07.005.

Dlubac, K., Knight, R., Song, Y. Q., Bachman, N., Grau, B., Cannia, J., & Williams, J. (2013). Use of NMR logging to obtain estimates of hydraulic conductivity in the High Plains aquifer, Nebraska, USA. Water Resources Research, 49(4), 1871–1886. https://doi.org/10.1002/wrcr.20151

Dunn, K.-J., Bergman, D.J., Latorraca, 2002, Nuclear magnetic resonance petrophysical and logging applications. Handbook of Geophysical Exploration: Seismic Exploration, Vol 32, Pergamon https://doi.org/10.1016/S0950-1401(02)80001-5.

Earle, L. R., Warner, B., and Aravena, R. (2003). Rapid development of an unusual peat-accumulating ecosystem in the Chilean Altiplano. Quaternary Research, 59: 2–11.

EPS SEDA CUSCO S.A. (2019). Memoria Anual 2019. Wanchaq, Cusco. (In Spanish). Accessed online January 2021. https://www.sedacusco.com/transparencia/memoria/2019.pdf

Flinchum, B. A., Holbrook, W. S., Grana, D., Parsekian, A. D., Carr, B. J., Hayes, J. L., & Jiao, J. (2018). Estimating the water holding capacity of the critical zone using near-surface geophysics. Hydrological Processes, 32(22), 3308–3326. https://doi.org/10.1002/hyp.13260

Flinchum, B. A., Holbrook, W. S., Parsekian, A. D., & Carr, B. J. (2019). Characterizing the Critical Zone Using Borehole and Surface Nuclear Magnetic Resonance. Vadose Zone Journal, 18(1), 0. https://doi.org/10.2136/vzj2018.12.0209

Fonken, M. (2014). An introduction to the *bofedales* of the Peruvian High Andes. Mires and Peat Volume 15(Article 4): 1-13.

Garreaud, R. D. (2009). The Andes climate and weather. Advances in Geosciences. 22, 3-11.

Garreaud, R., Vuille, M., Compagnucci, R., and Marengo, J. (2009). Present-day South American climate. Paleogeography, Paleoclimatology, Paleoecology. doi:10.1016.

Glas, R., Lautz, L., McKenzie, J., Moucha, R., Chavez, D., Mark, B., & Lane, J. W. (2019). Hydrogeology of an alpine talus aquifer: Cordillera Blanca, Perú. Hydrogeology Journal, 27(6), 2137-2154.

Gordon, R. P., Lautz, L. K., McKenzie, J. M., Mark, B. G., Chavez, D., & Baraer, M. (2015). Sources and pathways of stream generation in tropical proglacial valleys of the Cordillera Blanca, Perú. Journal of Hydrology, 522, 628–644. https://doi.org/10.1016/j.jhydrol.2015.01.013

Harden, C., Scruggs, P. (2003). Infiltration on mountain slopes: a comparison of three environments. Geomorphology 55; 5 –24.

Josse, C., Cuesta, F., Navarro, G., Barrena, V., Cabrera, E., Chacón-Moreno, E., Ferreira, W., Peralvo, M., Saito, J., Tovar, A. (2009) Ecosistemas de los Andes del Norte y Centro. Bolivia, Colombia, Ecuador, Perú y Venezuela. (Ecosystems of Northern and Central Andes. Bolivia, Colombia, Ecuador, Perú and Venezuela). Documento Técnico, Programa Regional ECOBONA-Intercooperation, CONDESAN-Proyecto Páramo Andino, Programa BioAndes, Secretaría General de la Comunidad Andina, Lima, 96 pp. (in Spanish).

Kaser, G. (1999). A review of the modern fluctuations of tropical glaciers. Global and Planetary Change 22, 93–103.

Kaser, G., M. Großhauser, and B. Marzeion. (2010). Contribution potential of glaciers to water availibility in different climate regimes. Proceedings of the National Academy of Sciences, 107, 20223-20227.

Kronenberg, M., Schauwecker, S., Huggel, C., Salzmann, N., Drenkhan, F., Frey, H., Giraáldez, C., Gurgiser, W., Kaser, G., Juen, I., Suarez, W., Garćía Hernaández, J., Fluixaá Sanmartín, J., Ayros, E., Perry, B., Rohrer, M. (2016) The Projected Precipitation Reduction over the Central Andes may Severely Affect Peruvian

Glaciers and Hydropower Production, Energy Procedia, Volume 97, 2016, Pages 270-277, ISSN 1876-6102, https://doi.org/10.1016/j.egypro.2016.10.072.

Lenters, J. and Cook, K. (1995). Simulation and diagnosis of the regional summertime precipitation climatology of South America, J. Climate, 8, 2988–3005, 1995.

Mosquera G, Lazo P, Célleri R, Wilcox B, Crespo P. 2015. Runoff from tropical alpine grasslands increases with areal extent of wetlands. Catena 125: 120–128. DOI:10.1016/j.catena.2014.10.010

Mosquera, G. M., Célleri, R., Lazo, P. X., Vaché, K. B., Perakis, S. S., & Crespo, P. (2016). Combined use of isotopic and hydrometric data to conceptualize ecohydrological processes in a high- elevation tropical ecosystem. Hydrological Processes, 30(17), 29302947.

Municipalidad Dsitrital de Zurite. (2017). Plan de Desarrollo Concertado del Distrito de Zurite al 2017 (Spanish). Accessed online: https://www.scribd.com/document/436252392/PLAN-DE-DESARROLLO-CONCERTADO-DEL-DISTRITO-DE-ZURITE-AL-2017.

Ochoa-Tocachi, B., Buytaert, W., Antiporta, J. et al. (2018). High-resolution hydrometeorological data from a network of headwater catchments in the tropical Andes. Sci Data 5, 180080. https://doi.org/10.1038/sdata.2018.80

Ochoa-Tocachi, B., Buytaert, W., De Bièvre, B., Célleri, R., Crespo, P., Villacís, M., Llerena, C., Acosta, L., Villazón, M., Guallpa, M., Gil-Rios, J., Fuentes, P., Olaya, R., Viñas, P., Rojas, G., Arias, S. (2016). Impacts of land use on the hydrological response of tropical Andean catchments, Hydrological Processes, Vol: 30, Pages: 4074-4089, ISSN: 1099-1085.

Oliveras, I., Girardin, C., Doughty, C. E., Cahuana, N., Arenas, C. E., Oliver, V. Malhi, Y. (2014). Andean grasslands are as productive as tropical cloud forests. Environmental Research Letters, 9, 115011.

Polk, M. H. Young, K. R. Cano, A. Leon, B. 2019. Vegetation of Andean wetlands (*bofedales*) in Huascarán National Park, Perú. Mires and Peat, Volume 24 (2019), Article 01, 1–26. DOI: 10.19189/MaP.2018.SNPG.387.

Polk, M.H., K.R. Young, M. Baraer, B.G. Mark, J.M. McKenzie, J. Bury and M. Carey. 2017. Exploring hydrologic connections between tropical mountain wetlands and glacier recession in Perú's Cordillera Blanca. Applied Geography 78:94–103 doi: 10.1016/j.apgeog.2016.11.004.

Rabatel, A., Francou, B., Soruco, A., Gomez, J., Caceres, B., Ceballos, J. L. (2013). Current state of glaciers in the tropical Andes: A multi-century perspective on glacier evolution and climate change. The Cryosphere, 7, 81e102. http://dx.doi.org/10.5194/tc-7-81-2013.

Salvador, F., Monerris, J., and Rochefort, L. (2014). Peatlands of the Peruvian Puna ecoregion: types, characteristics and disturbance. Mires and Peat, 15 (article 03): 1–17.

Schittek, K., Forbriger, M., Mächtle, B., Schäbitz, F., Wennrich, V., Reindel, M., Eitel, B. (2015). Holocene environmental changes in the highlands of the southern Peruvian Andes (14° S) and their impact on pre-Columbian cultures. Climate of the Past. 11. 27-44. 10.5194/cp-11-27-2015

Schmidt, L., and Rempe, D. (2020). Quantifying dynamic water storage in unsaturated bedrock with borehole nuclear magnetic resonance. Geophysical Research Letters, 47, e2020GL089600. https://doi.org/10.1029/2020GL089600

Segnini, A., Posadas, A., Quiroz, R., Milori, D.M.B.P, Saab, S.C., Martin Neto, L. and Vaz, C.M.P. (2010). Spectroscopic assessment of soil organic matter in wetlands from the High Andes. Soil Science Society of America Journal, 74, 2246–2253.

Somers, L., Gordon, R. P., Lautz, L. K., McKenzie, J. M., Wigmore, O., Glose, A., Glas, R., Aubry- Wake, C., Mark, B., Baraer, M., & Condom, T. (2016). Quantifying groundwater- surface water interactions in a proglacial valley, Cordillera Blanca, Perú. Hydrological Processes. https://doi.org/10.1002/hyp.10912

Somers, L. D., McKenzie, J. M., Mark, B. G., Lagos, P., Ng, G.- H. C., Wickert, A. D., et al. (2019). Groundwater buffers decreasing glacier melt in an Andean watershed—but not forever. Geophysical Research Letters, 46, 13016– 13026. https://doi.org/10.1029/2019GL084730

Somers, LD and McKenzie, JM. A review of groundwater in high mountain environments. WIREs Water. (2020); 7:e1475. https://doi.org/10.1002/wat2.1475

Squeo, F., Warner, B., Aravena, R., Espinoza, D., (2006). *Bofedales*: high altitude peatlands of the central Andes. Rev. Chil. Hist. Nat. 79, 245–255.

Tovar, C., Arnillas, C.A., Cuesta, F., Buytaert, W. (2013). Diverging responses of tropical Andean biomes under future climate conditions. PLoS One 8 (5), e63634.

Valois, R., Schaffer, N., Figueroa, R., Maldonado, A., Yanez, E., Hevia, A., Carrizo, G., MacDonell, S. (2020). Characterizing the Water Storage Capacity and Hydrological Role of Mountain Peatlands in the Arid Andes of North-Central Chile. Water 2020, 12, 1071; doi:10.3390/w12041071.

Vuille, M., Francou, B., Wagnon, P., Juen, I., Kaser, G., Mark, B., and Bradley, R. (2008). Climate change and tropical Andean glaciers: past, present, and future. Earth Science Reviews, 89: 79–96.

Vuille, M., M. Carey, C. Huggel, W. Buytaert, A. Rabatel, D. Jacobsen, A. Soruco, M Villacis, C. Yarleque, O. Elison-Timm, T. Condom, N. Salzmann and J.E. Sicart. (2018) Rapid decline of snow and ice in the tropical Andes – Impacts, uncertainties and challenges ahead. Earth Sci. Rev., 176, 195-213.

Whittall, K. P., Bronskill, M. J., and Henkelman, R. M. (1991). Investigation of analysis techniques for complicated NMR relaxation data. Journal of Magnetic Resonance (1969), 95(2), 221–234. https://doi.org/10.1016/0022-2364(91)90213-D

Wohl, E., Barros, A., Brunsell, N., Chappell, N., Coe, M., Giambelluca, T., Goldsmith, S., Harmon, R., Hendrickx, J., Juvik, J., McDonnell, J., Ogden, F. (2012). The hydrology of the humid tropics. Nature Climate Change 2 (9): 655–662. DOI:10.1038/NCLIMATE1556

Yang, S., Cammeraat, E., Jansen, B., Haan, M., Loon, E., Recharte, J. (2018). Soil organic carbon stocks controlled by lithology and soil depth in a Peruvian alpine grassland of the Andes, CATENA, Volume 171, 2018, Pages 11-21, ISSN 0341-8162, https://doi.org/10.1016/j.catena.2018.06.038.

Yang, S., Jansen, B., Kalbitz, K., Chunga Castro, F.O., van Hall, R.L., Cammeraat, E.L.H., (2019). Lithology controlled soil organic carbon stabilization in an alpine grassland of the Peruvian Andes. Environmental Earth Science in Press.

Zurite Comisión de Regantes de Agua (Water Users Commission). Personal communication. December 2020.

APPENDICES

Appendix A

Orographic precipitation results from rising convections of warm, moisture-laden air upward along topographic gradients, such as mountains, and cooling adiabatically through the process. The result is condensation and subsequent precipitation of water vapors with increasing elevation (Roe, 2005). Traditional spatial interpolation methods rely on geostatistical or deterministic approaches to account for variable effects on precipitation quantities (Ly et al, 2011; Hu et al, 2019, Ryu et al, 2020); however, these methods require networks of weather stations or rain gauges that are strategically positioned to capture variable effects on precipitation distribution, while also dense enough to allow for interpolation at the desired resolution (Ly et al. 2011; Ryu et al. 2020). Such spatially distributed precipitation data sets are critical drivers for hydrological and meteorological analyses and are frequently relied upon as driving parameters for spatial modeling methods that inform land use management decisions (Markstrom et al, 2008; MacKane et al, 2012; Markstrom et al. 2015; Hu et al, 2019).While useful in many applications, the resolution of published, large-extent spatially distributed precipitation data sets often renders them unusable in small catchment-scale applications (Mimeau et al., 2019).

Precipitation distributed within the URW

Given the small scale of the URW (2.12 km^2), existing gridded precipitation products that utilize deterministic or geostatistical interpolation methods (Aybar et al.,

2017; Aybar et al., 2020) did not perform at a resolution that was adequate to account for elevation ranges within the URW (4011 – 4543 m.a.s.l.). To account for orographic effects on precipitation, we plotted a time series of the 15-day moving average difference in measured precipitation between two identical HOBO RG3 tipping bucket rain gages, one installed in the URW and the other in the town of Zurite (Figure 32). Figure 33 shows a time series of the 15-day moving average difference in precipitation measured – displaying a consistent trend of greater precipitation received in the URW than in Zurite in all but a handful of days (shown as the orange, negative values in Figure 33). Figure 34 shows a longitudinal profile from the Casa Zurite rain gage to the URW rain gage and beyond, to the upper boundary of the URW.

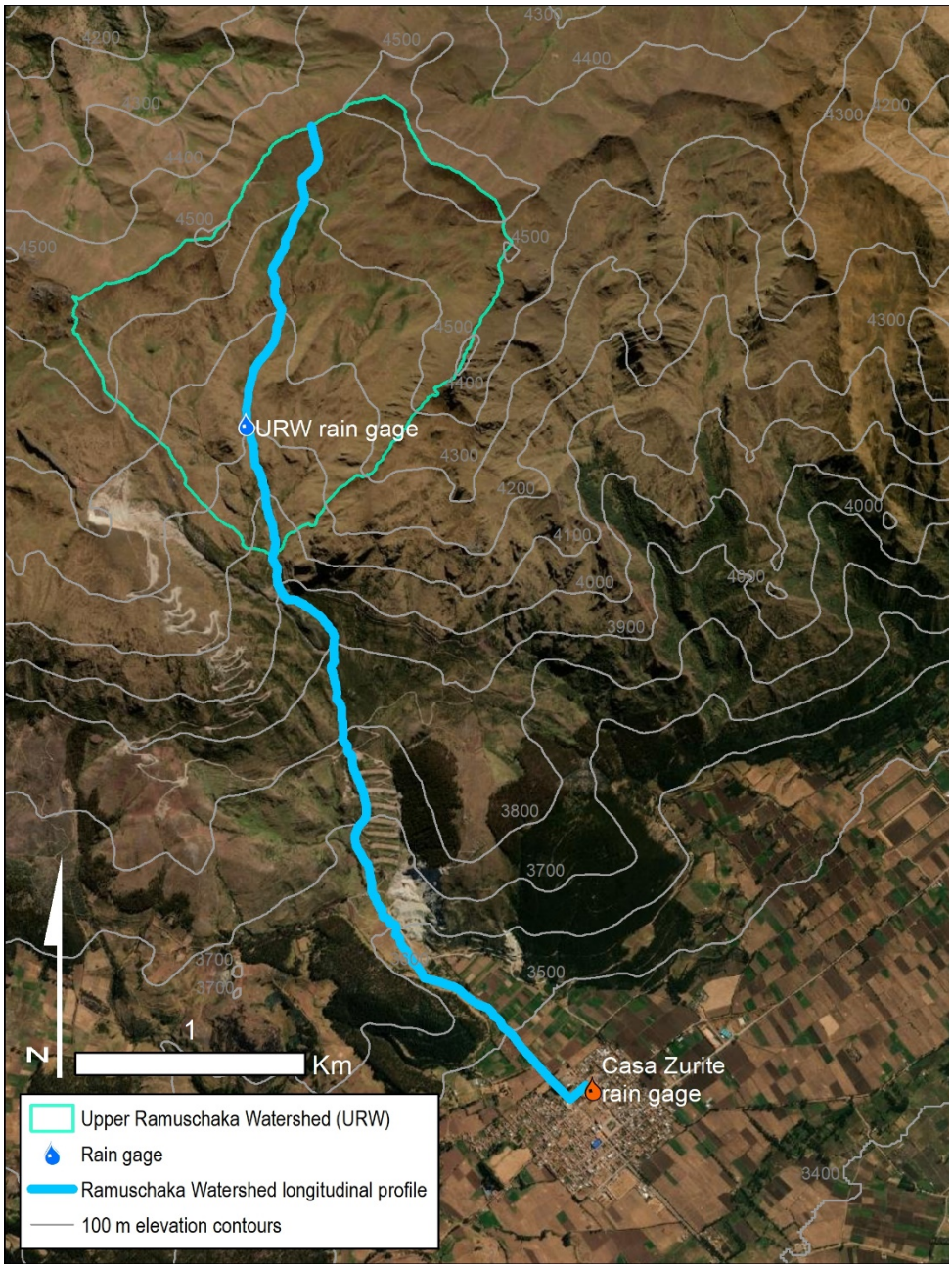

Figure 32. Overview of HOBO Onset RG3 tipping bucket rain gage placements in the URW and in the town of Zurite. There is approximately 800 m of vertical relief between 3.5 km of distance along the longitudinal profile up the Ramuschaka Watershed from the Casa Zurite rain gage.

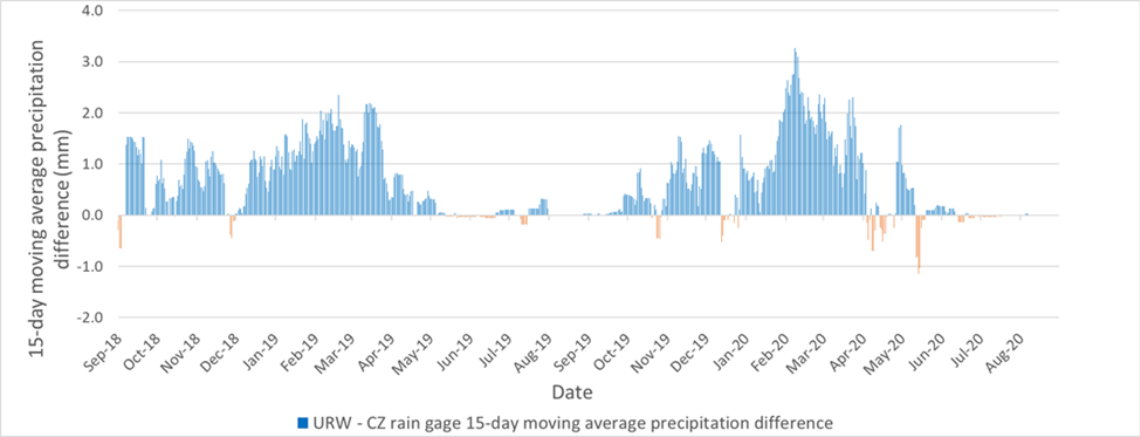

Figure 33. The 15-day moving average difference in precipitation measured between the URW rain gage and Casa Zurite rain gage in water years 2019 and 2020 demonstrates the general trend and seasonality of greater precipitation in the URW uplands (blue bars, positive values) than in Zurite. While present at several times in WY2019 and WY2020, we ignored periods in which the 15-day moving average precipitation was greater in Zurite than in the URW (orange bars, negative values), as we assumed that the primary effect on the difference in precipitation received was attributable to orographic elevation differences between the sites.

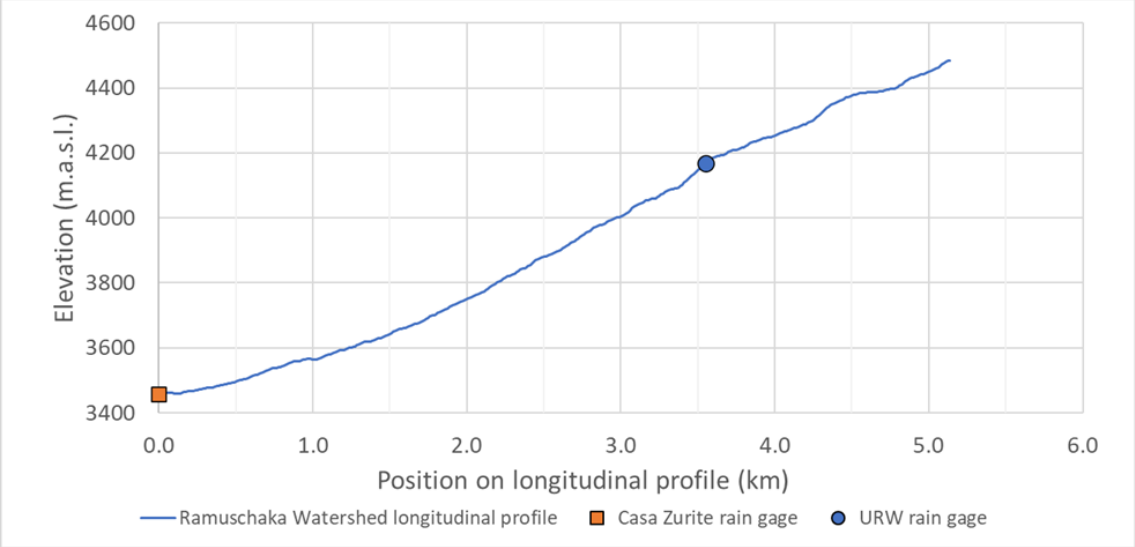

Figure 34. Longitudinal profile from Zurite to the upper bounds of the Ramuschaka Watershed with the marked elevations and positions of the two rain gages along the longitudinal profile. The elevation profile follows the Ramuschaka stream channel up to the URW northern boundary.

To account for orographic effects on precipitation across the elevation range of the URW, we extrapolated the 15-day precipitation difference (Figure 32) as a per-meter, per day precipitation adjustment for four elevations of the URW – the maximum and minimum elevations of the URW (4,543 and 4,011, respectively), and two arbitrary intermediate elevations. We proceeded to sum the total extrapolated precipitation for each of the four elevation points for WY2019 and WY2020 (Figure 34) and plotted them with observed cumulative water year precipitation values for the two rain gages (Figure 34). We proceeded to fit a second-degree polynomial function in Excel to the observed and predicted WY2019 and WY2020 elevation-adjusted precipitation values. We used the second-degree polynomial function to produce a URW gridded precipitation dataset as a

function of elevation for both water years with raster calculator and the 1-m DEM product we created from drone survey photogrammetry in *Agisoft Metashape Professional* (Figure 9).

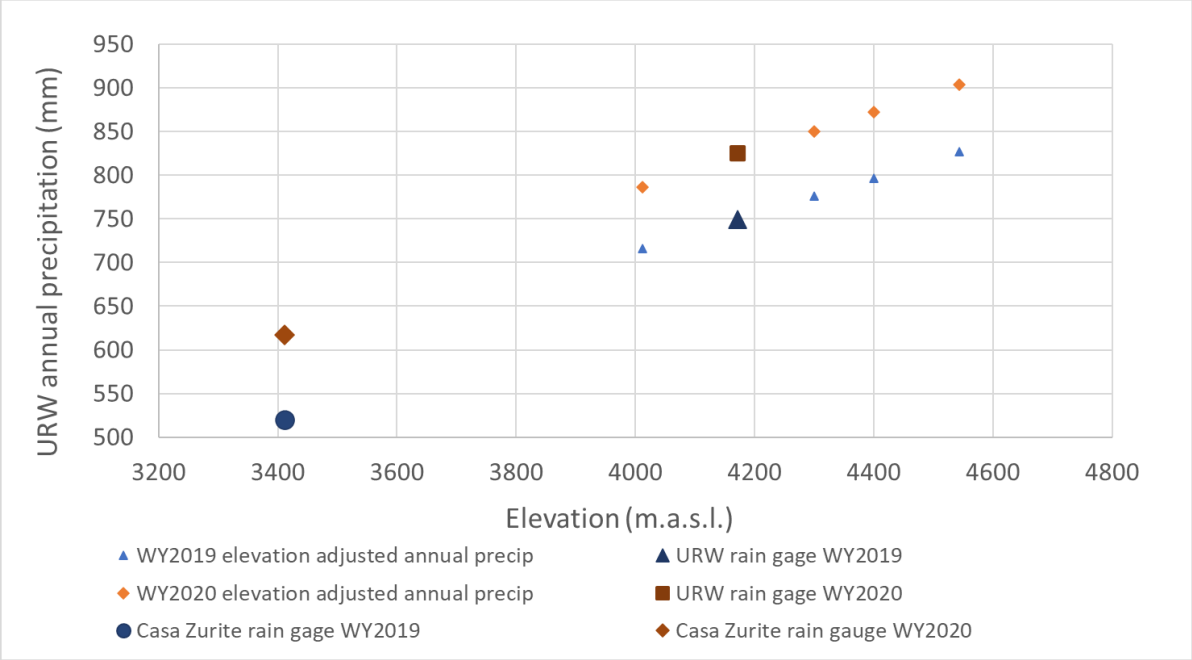

Figure 35. We developed a numerical correction for orographic effects on precipitation in the URW using a 15-day mean difference in precipitation received at the URW rain gage and the CZ rain gage. This plot shows the resulting elevation-adjusted annual precipitation values and measured precipitation quantities at the two rain gages for water years 2019 and 2020.

Error estimates for URW distributed annual precipitation

To estimate error of elevation-adjusted annual precipitation throughout the URW, we cross-validated the model by estimating precipitation at the URW rain gage from the

Casa Zurite rain gage and applied the resulting error as a proportion of the maximum extrapolated precipitation at the highest point within the URW (Table 12).

Table 12. Estimates of elevation-adjusted annual precipitation after accounting for orographic effects with a 15-day average difference model between two rain gages at different elevations.

Location	URW high point	URW rain gauge	URW low point	Casa Zurite (CZ) rain gauge	Cross validation CZ rain gauge applied to URW rain gauge elevation	Cross validation CZ rain gauge applied to URW rain gauge elevation	Maximum error in URW distributed precipitation (mm)
Elevation (m.a.s.l.)	4543	4171	4012	3411	4171	3411	Not applicable
WY2019 elevation adjusted annual precipitation (mm)	827	749.0	716	519.8	675	590	7.7

Location	URW high point	URW rain gauge	URW low point	Casa Zurite (CZ) rain gauge	Cross validation CZ rain gauge applied to URW rain gauge elevation	Cross validation CZ rain gauge applied to URW rain gauge elevation	Maximum error in URW distributed precipitation (mm)
WY2020 elevation adjusted annual precipitation (mm)	904	825.2	786	617.2	781	653	4.2

Results of URW distributed precipitation

Distributed elevation results are shown as URW maps with contours that represent elevation-adjusted annual precipitation contours for WY2019 (Figure 36) and WY2020 (Figure 37).

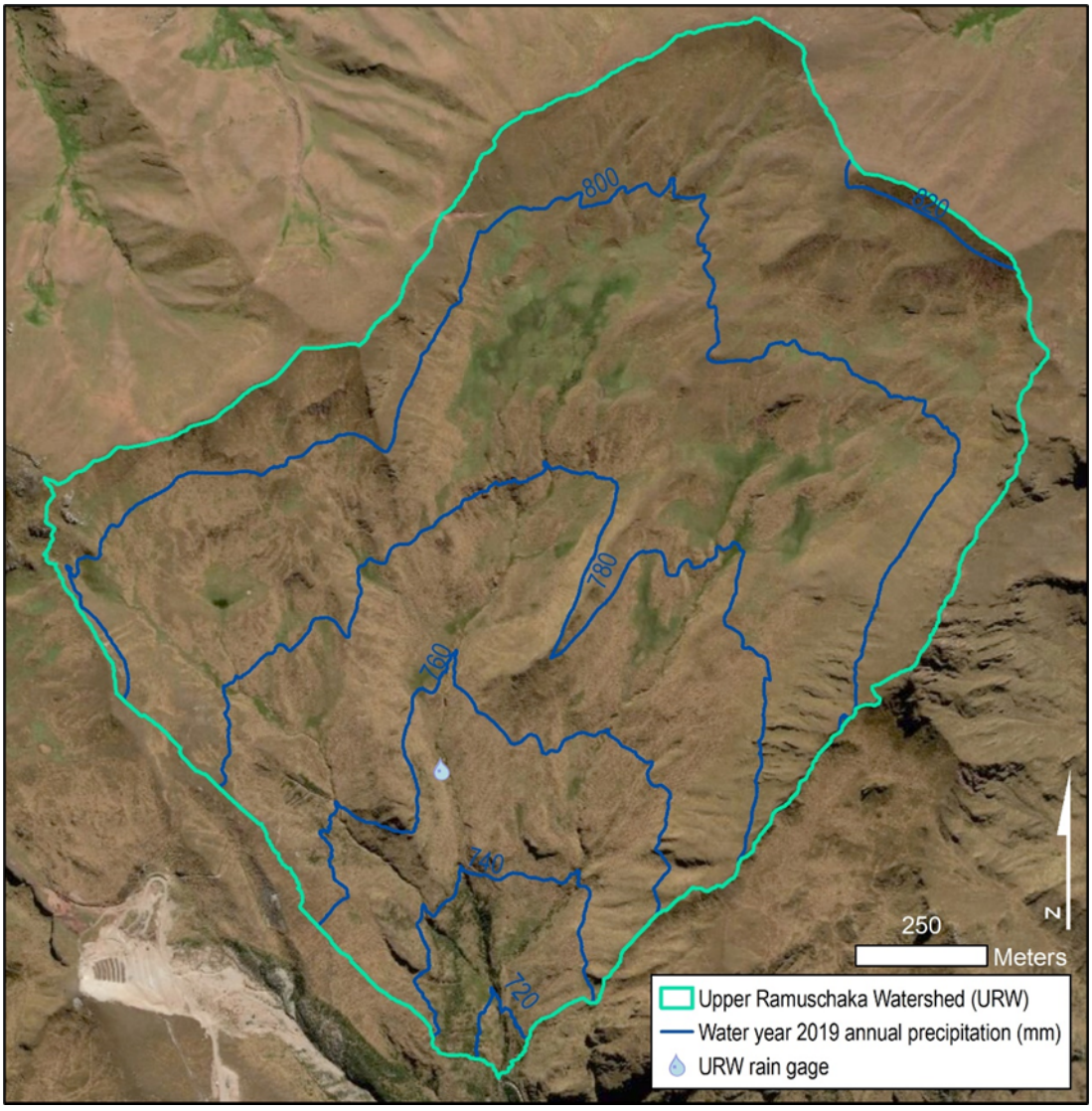

Figure 36. Distributed annual precipitation contours (mm) for water year 2019 are shown throughout the watershed. Total measured precipitation at the URW rain gage over water year 2019 was 749 mm.

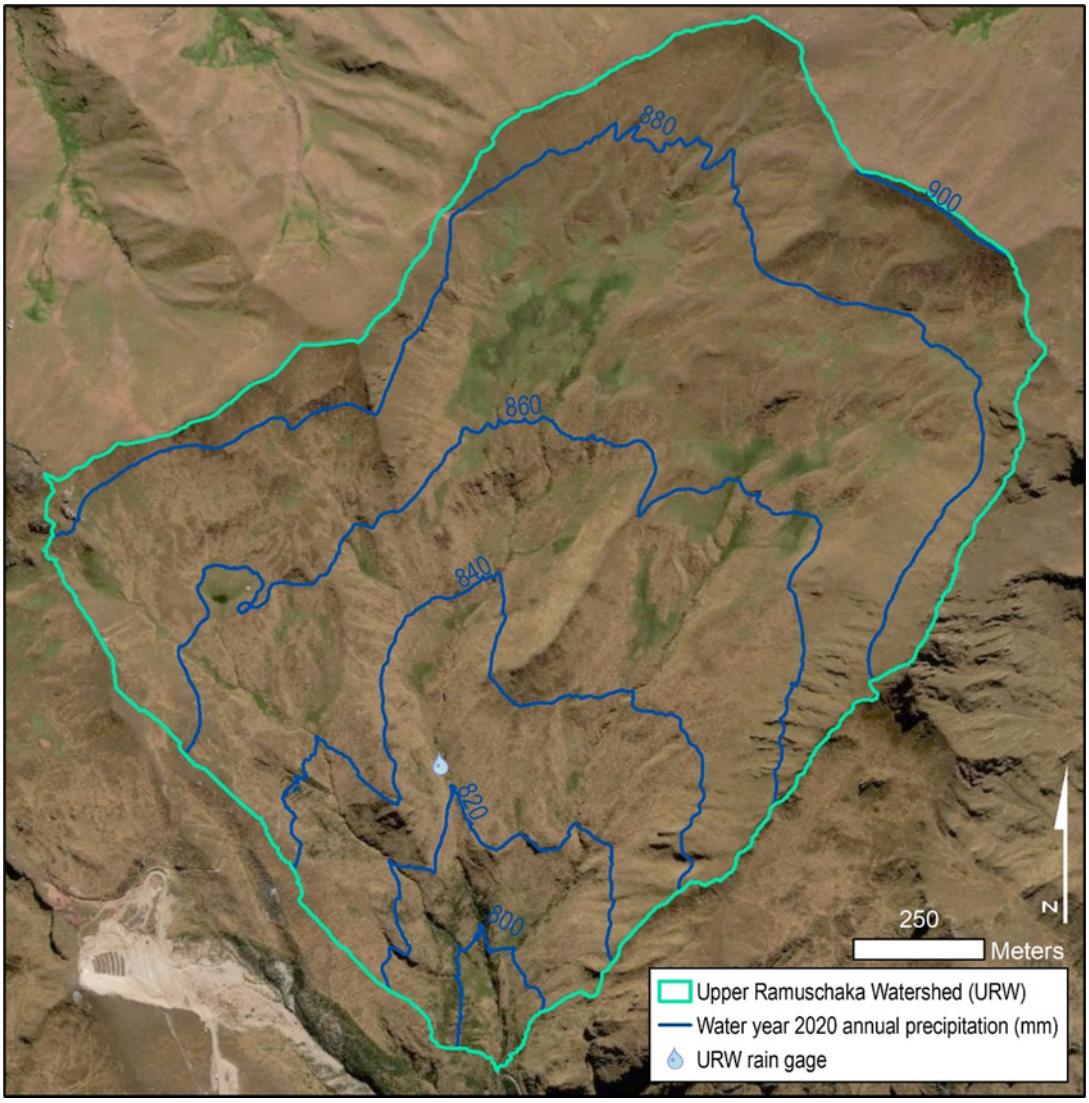

Figure 37. Distributed annual precipitation contours (mm) for water year 2020. Total measured precipitation at the URW rain gage over water year 2020 was 825 mm.

Appendix B

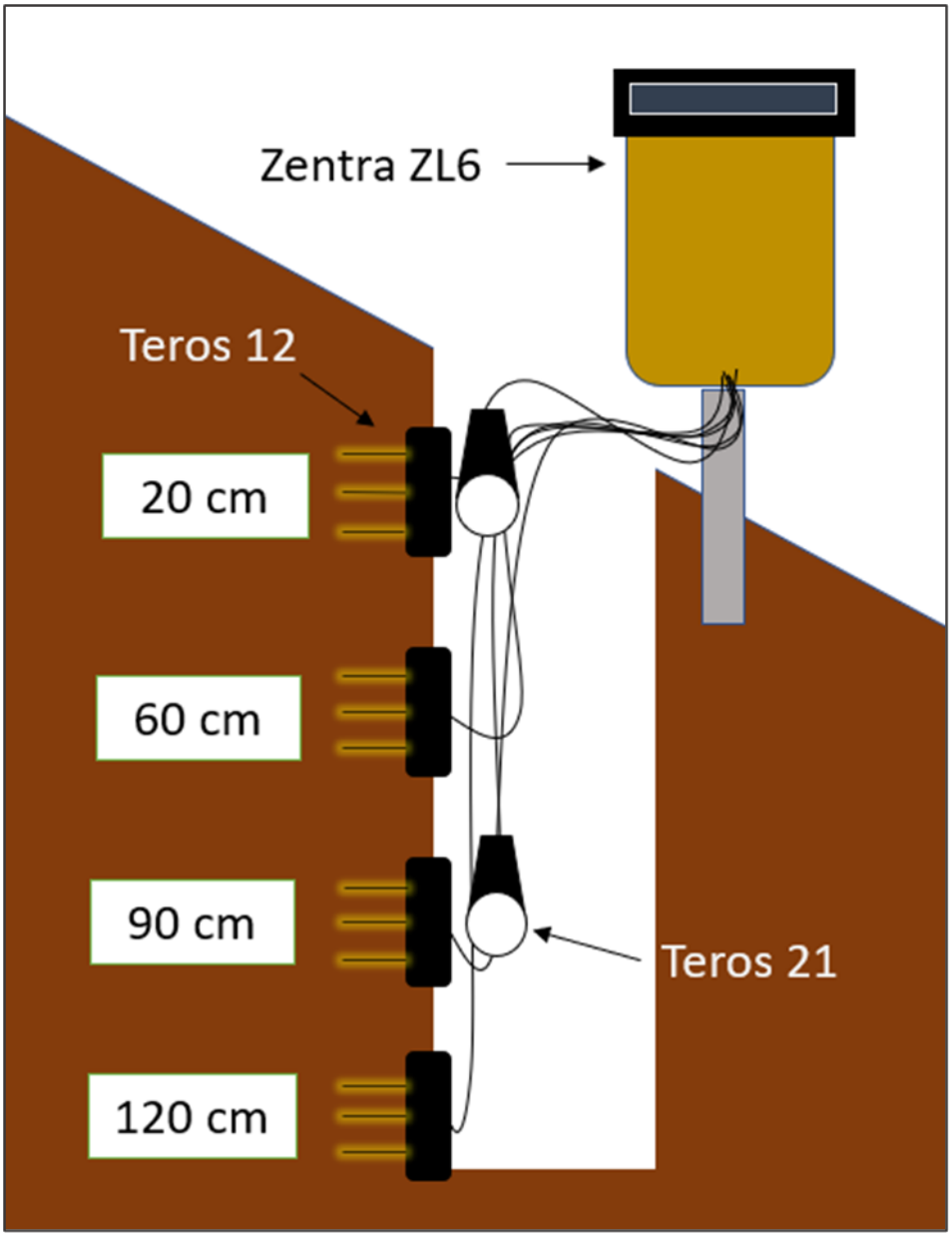

Figure 38. Schematic of installed Meter Environmental Zentra ZL6 data logger, four Teros-12 moisture sensors, and two Teros-21 matric potential sensors. The subsurface moisture sensor array was installed in a vertical profile of a hillslope near the URW rain gage, backfilled and gently compacted to minimize subsurface disturbance. Data values were recorded at 15-minute intervals from January 2019 until September 2020.

Table 13. Material descriptions of subsurface depths at which subsurface moisture sensors were installed.

Sensor Depth	Horizon Classification	Material Description
20 cm	Soil – A horizon	Dark brown, organic rich clayey soil. Deep A horizon. Abundant coarse and fine perennial grass roots. Very moist to wet.
60 cm	Soil – B/A horizon	Mixing boundary between A and B horizons. Dark brown, clayey soil mixed with red sandstone and mudstone clasts and red clays. Abundant perennial grass fine roots with some coarse roots. Moist to wet.
90 cm	Soil - B/C horizon	Red weathered sandstone and mudstone clasts with red clay intermixed. Few roots present, mostly fine. Moist to wet.
120 cm	Saprolite	Red, medium-grained sandy with abundant weathered sandstone and mudstone bedrock clasts. Some brown clay pockets. Very wet.

Field capacity estimate histograms

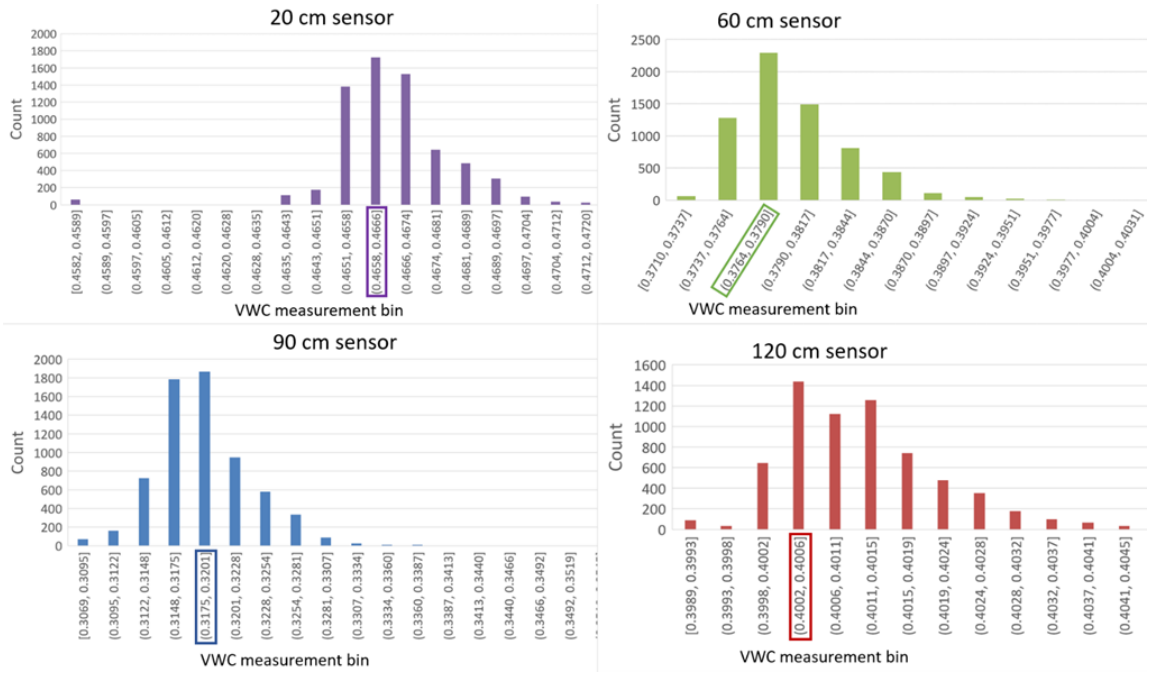

Figure 39. Histograms of volumetric water content (VWC) values plotted from the wettest time window measured (January 31 – April 8) in both water year 2020 to estimate field capacity for each subsurface layer. We binned each data series into 20 bins and used the mean value of the modal data bin as a field capacity estimate for each monitoring depth (represented as horizontal dashed lines in Figure 16.

Appendix C

Central stream gage

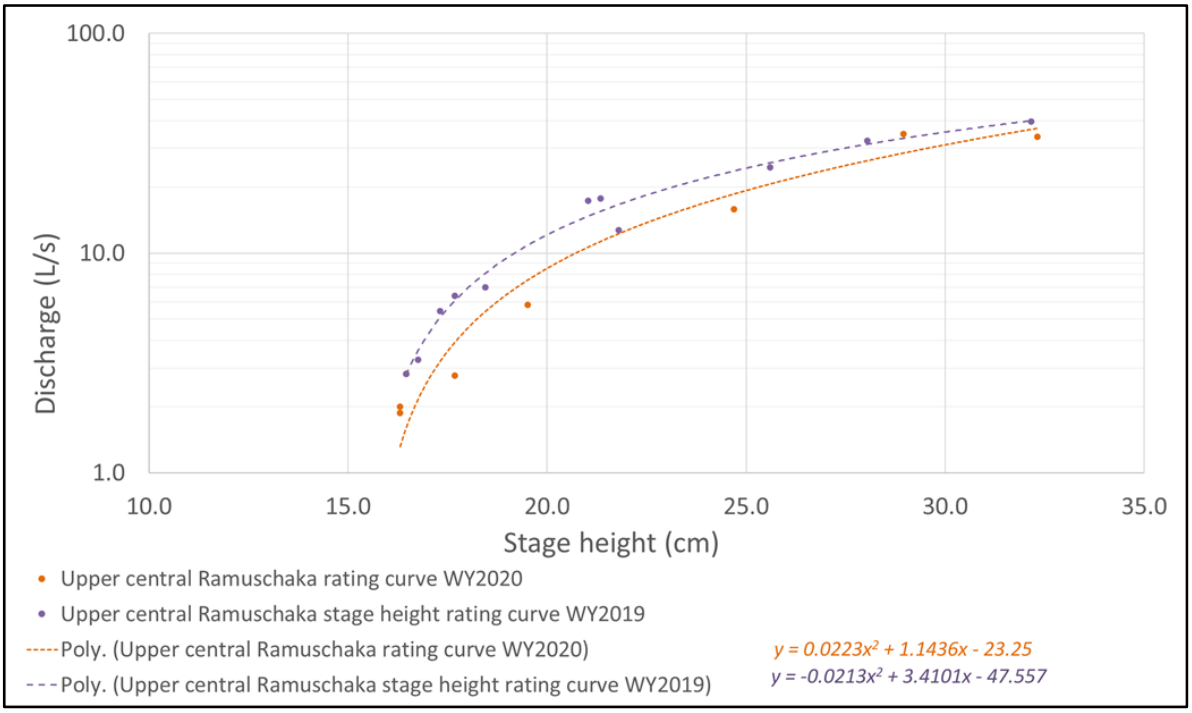

Figure 40. Stage height rating curves from discharge measurement dates for the URW Central stream gage for water years 2019 and 2020.

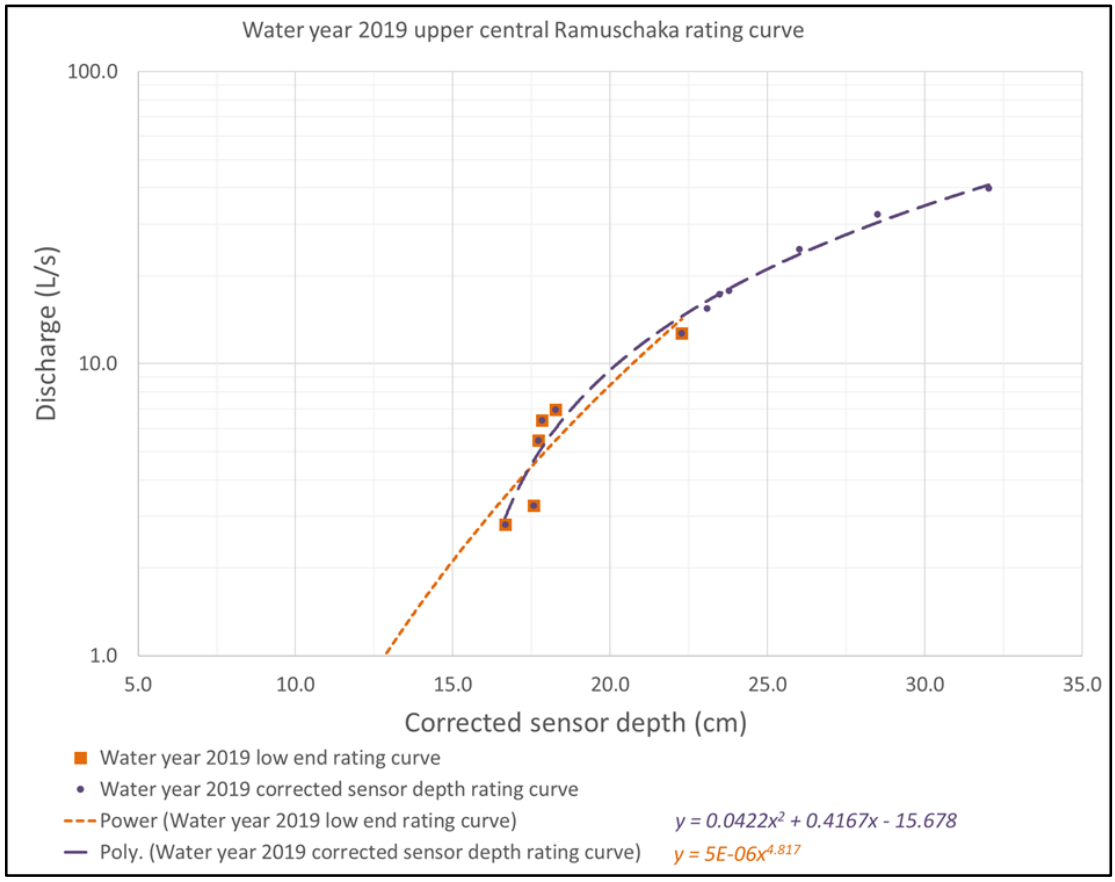

Figure 41. Rating curves for measured sensor depths at the Central stream gage for water year 2019. Discharge was estimated using the low-end rating curve below the lowest intersection of the two rating curves.

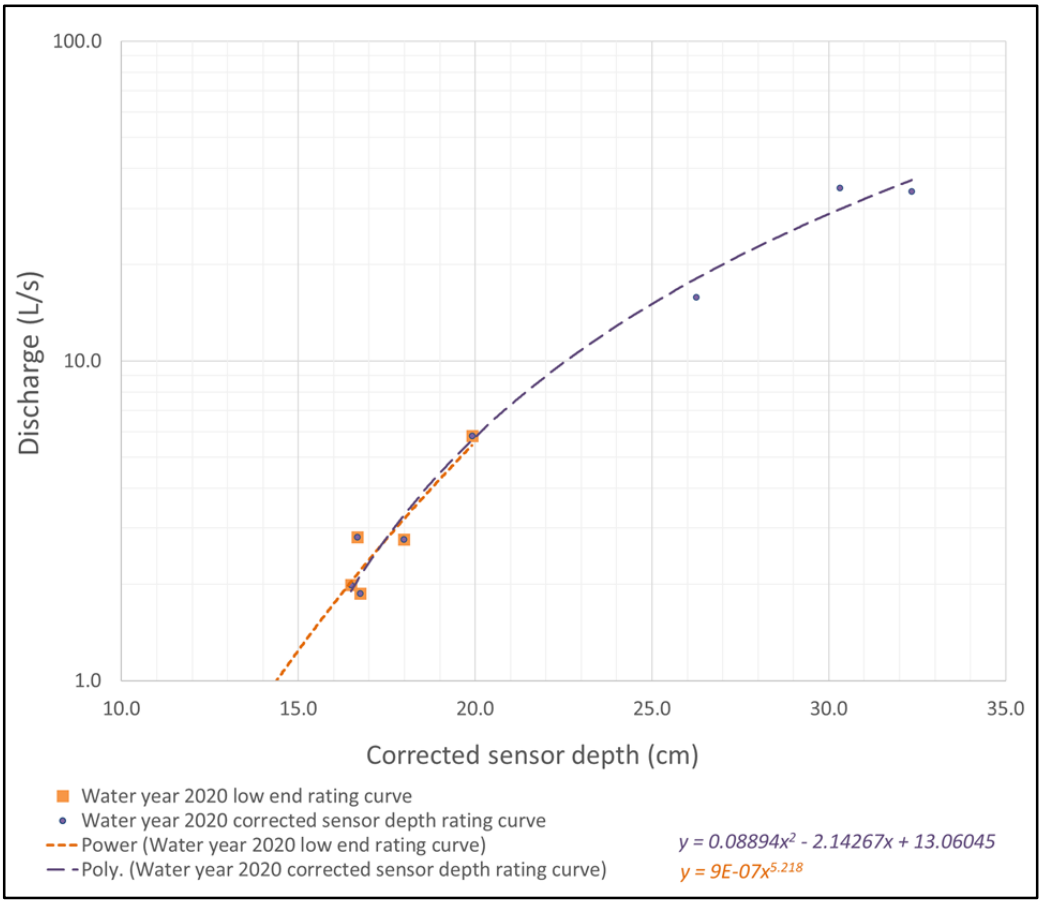

Figure 42. Rating curves for measured sensor depths at the Central stream gage for water year 2020. Discharge was estimated using the low-end rating curve below the lowest intersection of the two rating curves.

Above Diversion stream gage

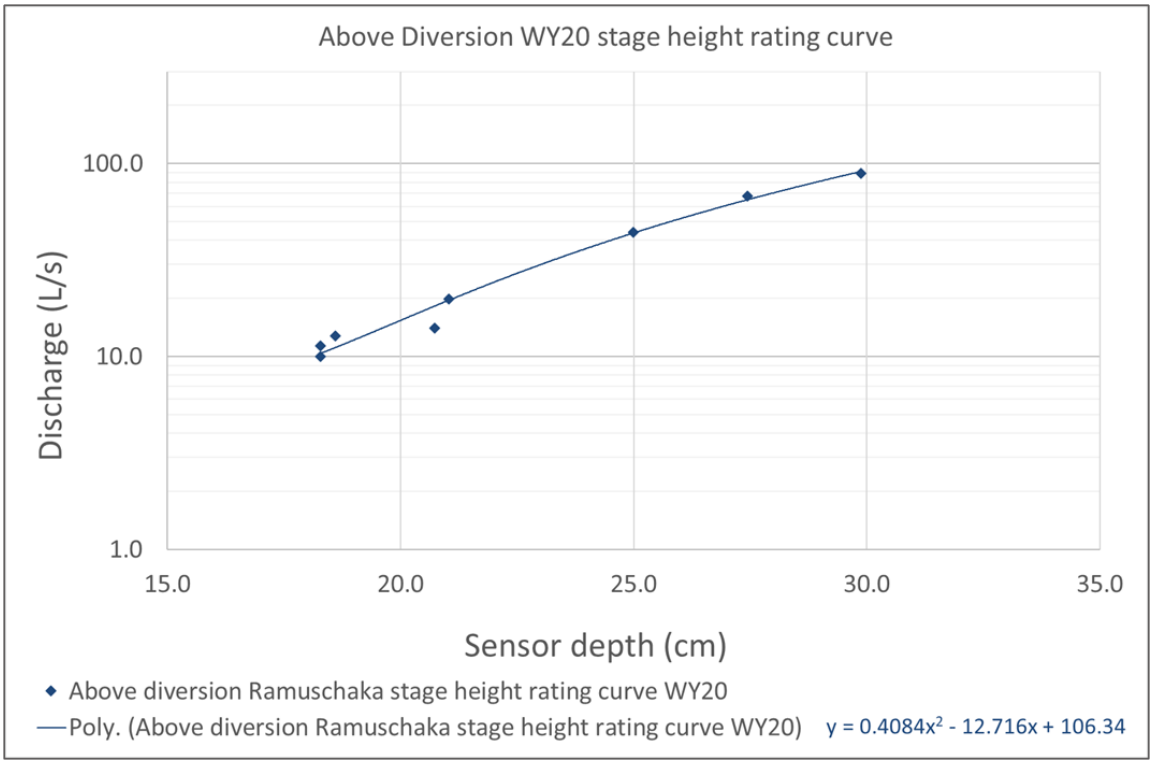

Figure 43. Stage height rating curves from discharge measurement dates for the URW Above Diversion stream gage for water year 2020.

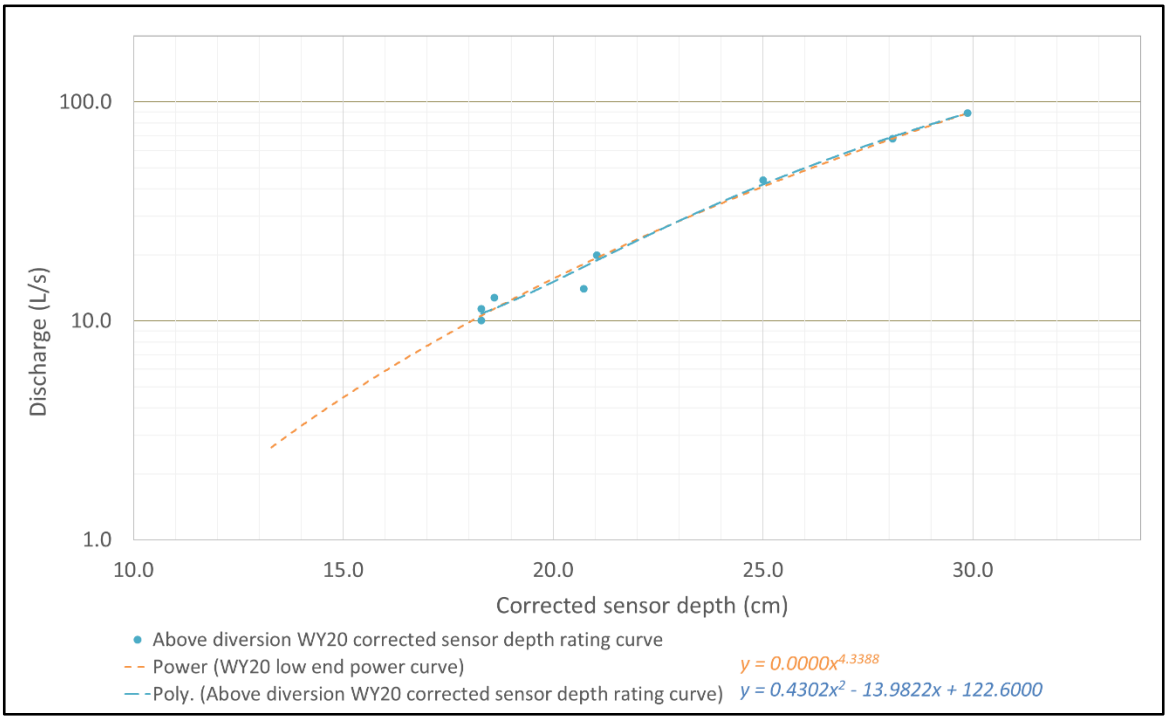

Figure 44. Rating curves for measured sensor depths for the URW Above Diversion stream gage for water year 2020. Discharge was estimated using the low-end rating curve below the intersection of the two rating curves.

Rating curve residuals

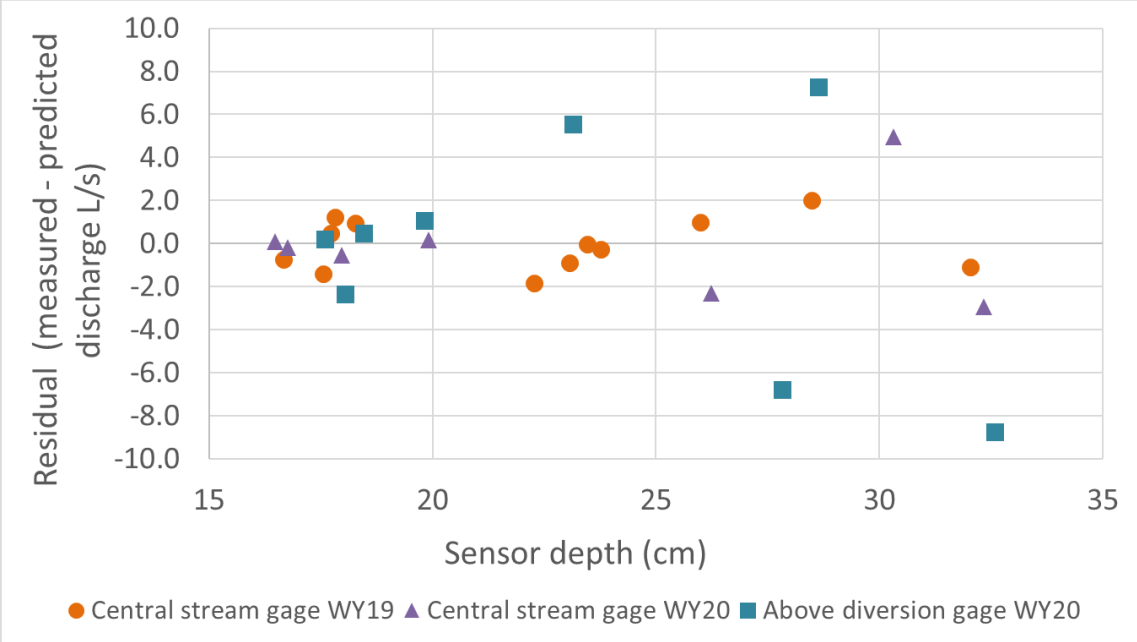

Figure 45. Residual error in rating curve predicted discharges relative to measured discharges. Residual error was small with lower flows and increased proportionally with the flow magnitude. Residual error appears to be randomly distributed.